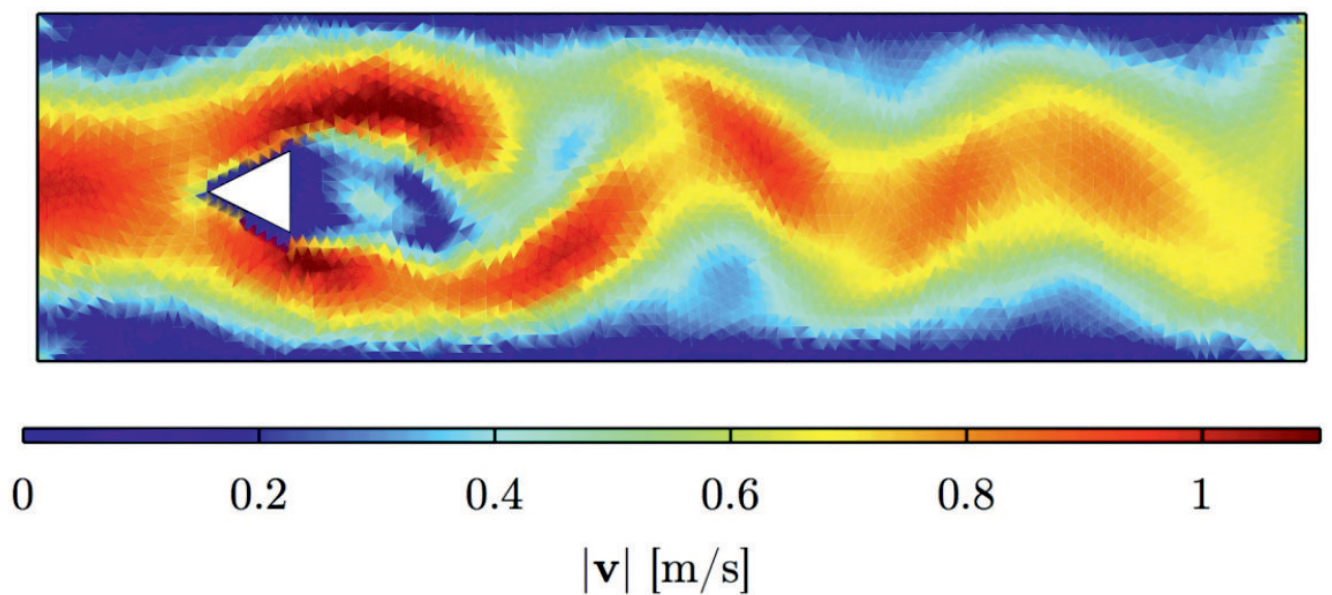


Fluid compressibility in a solid-fluid mixture flow

Timo T. Reisner



**Fluid compressibility in a solid-fluid mixture flow:
Experiments, modeling and numerical application to batch
sedimentation**

Dissertation
zur
Erlangung des akademischen Grades eines
Doktors der Ingenieurwissenschaften
der
Fakultät für Bau- und Umweltingenieurwissenschaften
der Ruhr-Universität Bochum

von

TIMO T. REISNER

aus Dortmund

Bochum 2015

Einreichung der Dissertation: (thesis submission)	23. Juni 2015
Tag der mündlichen Prüfung: (thesis defense)	18. September 2015
Erster Referent (first referee):	Prof. Dr. Holger Steeb
Zweiter Referent (second referee):	Prof. Dr. Ioana Luca
Dritter Referent (third referee):	Prof. Dr. Jörg Renner
Vorsitzender (committee chair):	Prof. Dr. Rüdiger Höffer

Preface

The present thesis is the outcome of my research as a Ph.D. student at the Chair of Continuum Mechanics, Ruhr-University Bochum, from 2011 to 2015. Originally a geoscientist, having the chance to get to know a different way of approaching problems in an engineering workgroup has immensely broadened my view. During this study, I have greatly profited from other people's support, too many to name them all. I would like to express my gratitude to:

Prof. Dr. Holger Steeb, for providing the opportunity to carry out a Ph.D. study at his chair, for offering great freedom to learn, and for his incredible and unshakable optimism.

Prof. Dr. Ioana Luca, for the inspiring joint work, for sharing her knowledge and experience in mathematics, and for her always patient explanations that have helped so much.

Prof. Dr. Jörg Renner, who first taught me the basics of Physics and Geophysics and later supervised my B.Sc. and M.Sc. theses, and became a true mentor for me over the past decade.

All colleagues in the chair, for the wonderful working atmosphere, and all the helpful discussions. The students Kristina Klein and Lukas Poggenpohl, who have helped in the lab experiments and in their evaluation.

My friends and family for providing either mental support or mental distraction from my work, depending on which was more necessary in any situation.

My wife Kati for her patience, support, love and understanding during both the good and difficult phases of being a young researcher;
And to my children, Aurelia and Joshua, for showing me what truly counts in life.

Bochum, June 2015

Timo Reisner

Abstract

This thesis concerns the influence of the fluid compressibility on the flow behavior of granular-fluid mixtures. Experiments on the outflow of a fluid-saturated granular medium from a laboratory-scale test rig are presented. The fluid phase consists of tap water at room temperature, while for the solid phase we have used spherical glass beads with diameters of 0.5, 2 and 4 mm, and mixtures thereof. The solid particle flow is captured on video and measured by Particle Image Velocimetry (PIV), and the pore fluid pressure is measured by absolute pressure sensors and highly sensitive dynamic pressure sensors. The results reveal strong interaction and feedback effects between the solid's flow behavior and the pressure of the pore fluid. The pore fluid pressure appears to have an outstanding influence on the overall flow process. The fluid pressure is in turn influenced by the porosity evolution of the solid phase. The dependence of the pressure on porosity can be explained by taking into account the fluid compressibility.

Based on the above observations, mass and momentum balances for a compressible fluid and an incompressible solid phase are employed in the development of a continuum mixture model. Due to the complexity of the experimentally observed flow pattern, the system of equations is closed with constitutive equations for the more simple case of batch sedimentation. The underlying balance equations are kept in their general form to allow for future extensions of the model to more complex flows. Batch sedimentation and the experimentally observed flow are linked by the fact that a relative motion between the phases and the full range of solid volume fractions are observed in both processes. However, batch sedimentation involves smaller Reynolds numbers and simpler boundary conditions. Due to the compressibility of the fluid phase, both transport phenomena and the propagation of acoustic waves are captured by the model.

The mixture model for batch sedimentation is numerically implemented into a discontinuous Galerkin framework. Acoustic waves reaching the boundaries of the computational domain are treated by special open boundary conditions that allow their free outflow. A number of standard Computational Fluid Dynamics benchmarks is used to verify the performance and accuracy of the numerical scheme. Then, numerical calculations of batch sedimentation are presented. The results for steady-state sedimentation are found to be in very good agreement with an analytical solution. Moreover, in the very beginning of the simulations, dynamic effects are observed that are due to the compressibility of the fluid phase and that have not yet been reported in the literature.

Zusammenfassung

Diese Dissertation beschäftigt sich mit dem Einfluss der Fluidkompressibilität auf das Fließverhalten granular-fluider Mischungen. Zunächst werden experimentelle Ergebnisse zum Ausfließen eines fluidgesättigten granularen Mediums aus einem kleinskaligen Behälter gezeigt. Die Fluidphase besteht aus Leitungswasser bei Raumtemperatur, während für die granulare Phase runde Glaskugeln mit Durchmessern von 0,5, 2 und 4 mm, sowie Mischungen derselben verwendet werden. Das Fließverhalten der Glaskugeln wird per Video und mittels Particle Image Velocimetry (PIV) aufgezeichnet. Der Porenfluiddruck wird mittels Absolutdrucksensoren sowie hochempfindlichen dynamischen Drucksensoren gemessen. Die Resultate zeigen starke Interaktions- und Kopplungseffekte zwischen dem Fließverhalten des fluidisierten granularen Festkörpers und dem Porenfluiddruck. Der Porenfluiddruck scheint einen herausragenden Einfluss auf den gesamten Fließprozess zu haben. Der Fluidruck wird wiederum von der Porositätsentwicklung der Festkörperphase beeinflusst. Die Abhängigkeit des Druckes von der Porosität lässt sich erklären, wenn das Porenfluid als kompressibel angenommen wird.

Basierend auf den o. g. Beobachtungen werden Massen- und Impulsbilanzen für ein kompressibles Fluid und eine inkompressible Festkörperphase verwendet, um ein Kontinuums-Mischungsmodell zu entwickeln. Aufgrund der Komplexität des experimentell beobachteten Fließprozesses werden jedoch zunächst Konstitutivgesetze für das einfachere Beispiel eines Sedimentationsprozesses eingesetzt. Die zugrundeliegenden Erhaltungsgleichungen bleiben aber in ihrer allgemeinen Form erhalten, um eine spätere Erweiterung des Modells auf komplexere Fließprozesse zu ermöglichen. Die Ähnlichkeit zwischen dem Sedimentationsprozess und dem experimentell beobachteten Fließprozesses ist durch die in beiden Prozessen auftretende Relativbewegung der beiden Phasen sowie die identische Bandbreite auftretender Volumenanteile des Festkörpers gegeben. Sedimentation ist jedoch mit kleineren Reynoldszahlen und einfacheren Randbedingungen verbunden. Aufgrund der Kompressibilität der Fluidphase werden sowohl Massentransportprozesse als auch die Ausbreitung akustischer Wellen im Modell abgebildet.

Das Mischungsmodell für Sedimentation wird numerisch mittels eines diskontinuierlichen Galerkin-Verfahrens implementiert. Akustischen Wellen wird der Austritt über die Ränder des Rechengebiets mittels spezieller offener Randbedingungen ermöglicht. Die Funktion und Exaktheit der numerischen Methode wird mittels einiger Standard-Benchmarks der numerischen Fluidodynamik verifiziert. Schließlich werden Simulationsergebnisse eines Sedimentationsprozesses gezeigt. Die Resultate für stationäre Sedimentation sind in sehr guter Übereinstimmung mit einer analytischen Lösung. Des Weiteren werden zu Beginn der Simulationen dynamische Effekte beobachtet, die der Kompressibilität der Fluidphase zuzuschreiben sind und über die in der Literatur bisher nicht berichtet wurde.

Contents

1	Introduction	1
1.1	Mechanical models for solid-fluid mixture flows	1
1.2	Motivation and outline	4
1.3	Numerical implementation	5
2	Experiment	7
2.1	Introduction and motivation	7
2.2	Experimental setup	8
2.3	Results	11
2.4	Discussion	18
2.5	Conclusions	23
3	Two-phase hybrid continuum mixture model	25
3.1	Introduction and motivation	25
3.2	Framework	26
3.3	Kinematical assumptions	27
3.4	Balance equations	30
3.5	Constitutive relations for batch sedimentation	33
3.6	Summary and discussion of the hybrid model	39
4	Numerical implementation - dG method	41
4.1	Introduction to the discontinuous Galerkin method	42
4.2	2-D problems	58
4.3	Open boundary conditions	66
4.4	Numerical implementation of the hybrid model	74
4.5	Time integration	76
5	Simulations of batch sedimentation	83
5.1	Initial boundary value problem	83
5.2	Results and discussion	85
5.3	Conclusions	96
	Conclusions and Outlook	99
	Bibliography	101

Chapter 1

Introduction

1.1 Mechanical models for solid-fluid mixture flows

The subject of this thesis is the flow behavior of fluidized aggregates of solid grains and a continuous fluid filling the void space between the grains. The outflow of a granular-fluid mixture from a laboratory test rig and batch sedimentation serve as examples of such flows. In the field of *dry* fluidized granular materials, numerous problems have been investigated, cf. e.g. [34, 69]. However, if a fluid is added into the pore space, the situation is surprisingly more complex. Brennen [11] notes: *"All of the above analysis [concerning dry granular flows] assumed that the effect of the interstitial fluid was negligible. When the fluid dynamics of the interstitial fluid have a significant effect on the granular flow, analysis of the rheology becomes even more complex and our understanding is quite incomplete"*. Although this statement is already a bit dated, it's message is as relevant as ever. Next we give an overview of the scientific fields where fully saturated granular flows are investigated, and a classification of mathematical modeling methodologies used in the respective contexts.

Depending on the problem and the scale of interest, two principally different approaches to describe mixtures of a continuous fluid and dispersed gaseous, fluid or solid particles are found in the literature: in *microscopic* models, an equation of motion is solved for *each particle*. *Macroscopic*, or continuum models, on the other hand, investigate the *averaged* motion of the constituents or phases of the mixture within a Representative Elementary Volume (REV), cf. [23, 75].

Binary, i.e., two-phase mixture models based on a microscopic formulation are proposed e.g. by Yazdchi et al. [87]. A mesh-free Discrete Element Method (DEM) is used to numerically calculate the motion of single solid particles, while the flow of the continuous fluid is usually solved using "classical" Stokes- or Navier-Stokes solvers based on a Finite-Volume, Finite-Difference or Finite-Element schemes. Newer contributions (e.g. [55, 57]) propose to use mesh-free methods, as Lattice-Boltzmann (LB) or Smoothed Particle Hydrodynamics (SPH), also for the description of the continuous phase. The coupling between solid and liquid phase can be achieved using a staggered scheme, where the motion of one of the phases within one time step and the corresponding interaction forces are calculated first, and the results enter the computation of the motion of the other phase. Microscopic models are especially suitable for small-scale problems involving a restricted number of particles; due to the computational cost, they are not suitable for high particle densities.

On the other end of the model classification are macroscopic models on the continuum scale. Such models describe the microscopic, multi-phase composition of the mixture on a macroscopic scale by incorporating the volume fraction of each phase; and by attributing a set of balance equations to each continuum *phase* instead of each microscopic *particle*. This approach is prevalent in numerous fields dealing with high particle concentrations, e.g. fluidized beds [3, 33, 44], avalanches [39, 43], debris flows [39, 80], sediment transport [13, 14, 30], slurry transport in pipelines [62], and soil liquefaction [25].

A possible subdivision of the macroscopic continuum models could be according to the volume fraction of the dispersed phase. Many commercial and open-source codes in Computational Fluid Dynamics (CFD) appear to be structured along a similar classification.

- Class A
 - Mass balance equation for the mixture as a whole
 - Momentum balance equation for the mixture as a whole
 - This class of models is usually implemented if the physical problem involves a low volume fraction of the dispersed phase. The resulting equations are very similar to the Navier-Stokes equations, where the viscosity of the mixture as a whole is determined as a function of the volume fraction of the dispersed phase, cf. [23, 75]. The information about the velocities of the single phases is not naturally resolved by such models and only recovered, if desired, by postulating closure relations.
- Class B
 - Mass balance equation for each constituent
 - Momentum balance equation for the mixture as a whole
 - Models belonging to this class can be employed when the volume fraction of the dispersed phase is still low, but the distribution of the volume fractions of fluid and dispersed phase is of interest. In case of density preserving (i.e., incompressible) constituents, the volume fractions can be directly obtained from the mass balance, while in case of non-density preserving (i.e., compressible) constituents, evolution equations for the volume fractions must be postulated. The constituent velocities are still calculated constitutively in this case.
- Class C
 - Mass balance equation for each constituent
 - Momentum balance equation for each constituent
 - When the flow of the dispersed phase is not only influenced by the flow of the continuous phase (*one-way coupling*), but also vice versa, the flow of the continuous phase is significantly influenced by the dispersed phase flow (*two-way coupling*), the use of a model of Class B is not possible because the phase velocities cannot be recovered employing a constitutive law. Two-way coupling usually occurs at high phase fractions of the dispersed phase.

Other classifications than the one given above are of course possible, cf. e.g. [38, Sec. 7.1]. Clearly, the numerical cost, and also the complexity increase from Class A to Class C due to the increasing number of equations to be solved. According to the above classification, the model developed in Chapter 3 belongs to Class C. In the following, some application fields for the above models are presented.

Sediment transport models describe two-phase flow processes of fluid-granular mixtures at a large range of volume fractions of the dispersed particles. Most contributions make use of the so-called Navier-Stokes-Fourier-Fick equations (Class A), consisting of the mass and momentum balance equations of the mixture and an advection-diffusion equation for the description of the temporal evolution of the sediment surface. Numerical implementations often use staggered approaches for the coupling of the two processes: First, the flow equations are solved. The results deliver boundary conditions for the advection-diffusion process; and in turn the results from that process enter the calculation of the flow field [50, 61, 65]. The solution variable is the barycentric velocity of the mixture, so that the information on the phase velocities remains unknown. The staggered approach allows to restrict the computational domain to the area above the sediment bed, where the sediment concentration is sufficiently low to enable the use of a model of Class A. However, when the sediment is redistributed, the computational domain must be re-meshed according to the new shape of the bottom boundary. Moreover, the flow within the sediment bed is not captured in these models. Suitable methods as e.g. Volume-of-Fluid (VOF) and Level-Set methods are used for the resolution of the sediment surface. The idea of the VOF method is to monitor the gradient of sediment concentration within the computational domain; the interface is located near the isoline of the gradient's maximum. The Level-Set method employs a partial differential equation (a so-called Level-Set function) to locate the position of the interface at each timestep. While the VOF method is easy to implement and numerically cheap, the interface tends to be "smeared out". The Level-Set method, on the other hand, is more precise, but involves the numerical solution of an additional partial differential equation.

Binary geophysical mass flows (e.g., landslides and debris flows) are usually described in the framework of Mixture Theory, using mass and momentum balance equations for both the solid constituent and the mixture (Class B), or the solid and fluid constituents (Class C). However, most numerical implementations exploit the assumption that the longitudinal dimensions of the flow are much greater than the height, and transfer the equations to so-called shallow water equations, thereby reducing the dimensionality of the problem by one [68, 81].

Another application of Mixture Theory models is the field of Fluidized Beds, where the mass and momentum balance equations of both continuous and dispersed phases are implemented (Class C) due to the high phase fractions of the dispersed phase [3, 33, 44]. The majority of contributions is however devoted to gas-solid mixtures; liquid-solid mixtures are less prominent, cf. [88]. Need for research is seen in relation to the viscosity of the particle phase and the behavior close to densest packing [88]. Note that in Fluidized Beds the fluid is pumped through the porous medium from below; hence the fluid pressure is a control variable. Consequently, the type of flow is different from geophysical mass flows because in case of Fluidized Beds the particles are maintained in a fluidized state by an externally applied pressure; whereas geophysical mass flows might be triggered by an instantaneous increase in pore pressure, but once in motion, are self-sustaining.

Rusche [73] proposed a binary mixture model for the case of a high volume fraction of the dispersed phase (Class C) that is independent of the aggregate state of the phases. His work forms the basis of the multi-phase branch of the Open-source software OpenFOAM. Numerical examples are related to fluid-gas and fluid-fluid mixtures. OpenFOAM employs the Finite Volume Method to solve the partial differential equations, cf. Section 1.3.

1.2 Motivation and outline

The motivation for this study is given by the collapse of the Historical Archive of the City of Cologne into an underground cavity, causing two casualties in March 2009. It is believed that the cavity was created by the failure of a diaphragm wall and subsequent efflux of the water-saturated soil into a nearby excavation pit. Although many research fields are concerned with solid-fluid mixtures in general (cf. Section 1.1), the outflow of a solid-fluid mixture through an orifice from a confined reservoir seems not to be well understood. Hence experiments on the outflow of a fully water-saturated assembly of spherical glass beads from a container were conducted and are presented in Chapter 2. The container is 50 cm high and has a basal surface of 10 x 20 cm. The flow process is impulsively started by opening a hatch at the bottom of one of the side walls. The experimental setup is a small version of a large-scale experimental facility at the Institute and Laboratory of Geotechnics of the Technical University of Darmstadt, cf. [46], for the investigation of the flow behavior of water-saturated gravelly soils. The experiment at the University of Darmstadt focuses on a realistic flow process at a large scale using natural soils. However, due to the sheer scale of the experimental setup, the effort in terms of material and workforce to conduct one single experiment is relatively high. In contrast, the small-scale experiment focuses on the understanding of the physical processes during the fluid-solid mixture flow. The smaller scale allows to conduct more experiments at low cost; while at the same time, it is possible to use more exact measurement equipment under laboratory conditions. Moreover, due to the low material need, it is possible to systematically vary the grain sizes and to use mixtures thereof. The use of spherical glass beads allows for a simple estimation of the permeability. Yet, the geometry of both experiments was chosen to coincide to allow for a later comparison of the results. The results may also be relevant in the field of landslides and debris flows, because the failure mechanism leading to these mass flows is often similar to that observed in the experiments, where the generation of a local weakness of the porous medium leads to the subsequent failure of the complete porous skeleton.

The observations made during the experiments clearly show that the observed phenomena cannot be explained without accounting for the compressibility of the pore fluid. The compressibility of water is so low that it is usually assumed incompressible in models of solid-liquid mixtures. However, a low compressibility leads to a strong reaction in terms of pressure to small changes in fluid volume. In case of the experiments shown here, the volume that is available for the fluid is determined by the pore space. The fluidization of a porous skeleton, in turn, is associated with an increase in pore space.

These observations motivate the development of a new mixture model for the flow of fluid-granular mixtures, assuming incompressible grains and a *weakly* compressible, barotropic pore fluid in Chapter 3. In the following, the term *hybrid model* will be used to indicate the use of a compressible and an incompressible constituent. Tradi-

tionally, the reason to assume weak compressibility is a numerical one: it is assumed in numerical frameworks where it is desirable to avoid implicit integration schemes, e.g. Smoothed Particle Hydrodynamics (SPH, [63, 76]), to approximate the behavior of fluids that would be assumed incompressible in other numerical frameworks. Implicit integration is necessary when the pressure appears as a free variable. In SPH in particular, the implementation of incompressible models is also possible, and weak compressibility is solely assumed for reasons of numerical efficiency. Here, the idea behind weak compressibility is twofold: on the one hand, as in SPH, the assumption of a weakly compressible pore fluid allows for the use of relatively simple, explicit time integration schemes. On the other hand, however, effects that occur due to the compressibility of the pore fluid, e.g. the phenomena presented in Chapter 2, and also the propagation of acoustic waves are described by the model.

Due to the complexity of the mixture flow presented in Chapter 2, the balance equations of the hybrid model are supplied with constitutive relations for the application of batch sedimentation of spherical particles in water. The balance equations are, however, kept in their general form to allow for a simple extension of the model to other types of flow. As yet, apparently only three contributions [15, 53, 54] have dealt with the implementation of such a general model for the description of batch sedimentation, and none of them employs a compressible fluid phase.

Chapter 4 outlines the numerical implementation of the model into a discontinuous Galerkin (dG) framework. The method is first introduced in 1-D and examples are given, then the 2-D case is presented. Numerical benchmarks for the structurally similar weakly compressible Navier-Stokes equations are shown. Due to the compressible nature of the fluid, acoustic waves may emerge within the computational domain, requiring a special treatment of in- and outflow boundaries. The approach used here is described and verified by a numerical example. Finally, the implementation of the mixture model equations is described.

Chapter 5 deals with the actual simulations of batch sedimentation. It is shown that for stationary sedimentation, the results converge to an analytically derived solution. However, at the beginning of the numerical experiments, visible and significant effects due to fluid compressibility are found. To obtain a better understanding of the coupled system of equations and the process of sedimentation itself, the single terms of the momentum balance are separated into their contributions to the overall force balance within the different areas of the sedimentation vessel. Finally, a parameter study reveals the influence of several constants appearing in the constitutive laws on the sedimentation process.

1.3 Numerical implementation

The mathematical model presented in Chapter 3 consists of a system of strongly coupled conservation laws (Class C, cf. Section 1.1). Traditionally, two methods have emerged to solve such problems, namely the Finite-Difference Method (FDM) and the Finite Volume Method (FVM). While the FDM is robust and relatively simple to implement, it requires the use of structured grids and fails on complex geometries. The FVM does not suffer from this shortcoming and has nowadays become the standard in many commercial and non-commercial CFD solvers. It is based on a local approximation of the solution within a computational grid cell, while the global solution is recovered by means of a numerical flux between adjacent elements. The choice of the flux allows for the consideration of specific requirements of the equations to be solved;

e.g. in problems involving a preferred propagation direction, like convection dominated problems, so-called upwind fluxes are used to increase the stability. Due to the locality of the scheme, it is easily parallelizable for computation on multi-processor computers. However, the FVM has strong limitations in the possible order of approximation, and as a consequence, it is not hp-adaptive. The term hp-adaptivity relates to a flexible, local refinement of the computational mesh in terms of grid cell size (h-adaptivity) and approximation order (p-adaptivity). Another method, traditionally used in fields dealing with elliptic problems, is the Finite Element Method (FEM). In FEM, a high-order approximation and hp-adaptivity are relatively easy to achieve. Here, the approximation of the solution is not defined locally, but rather on a global level comprising the full computational domain. This globality, in turn, leads to potential stability issues for problems where information flows in a preferred direction.

The issues with each of the methods outlined above have led to the development of the discontinuous Galerkin (dG) method, which combines many advantages from FVM and FEM. Within each single element, the approximation corresponds to that of FEM, while the coupling between the single elements to a contiguous domain is achieved via a numerical flux over the element boundaries, as in FVM. This combined approach makes the method robust for convection dominated problems, easily parallelizable as FVM; and at the same time the method is of high approximation order and hp-adaptive as FEM.

The coupled model equations to be implemented are similar to the compressible Navier-Stokes equations, hence contain hyperbolic and parabolic parts. Suitable dG methods for this type of equations were first proposed by Bassi & Rebay [5] and Cockburn & Shu [16]. They are nowadays known by the name *Local Discontinuous Galerkin* (LDG). Here, operators of second order are first transferred into systems of first-order equations, which are then implemented using the standard dG approach. More advanced methods that emerged from LDG are the Compact Discontinuous Galerkin (CDG) method [66] and the CDG2 method [10], which only contain next neighbors in the flux term and hence are more compact and more suitable for parallel implementation. Alternatives for the treatment of elliptic terms include the Internal Penalty (IP) and Bassy-Rebay 2 (BR2) methods, cf. [10]. The codes developed for this thesis rely on the nodal dG method as outlined by Hesthaven & Warburton [35] and partly on the Open-source dG software Pydgon by Klöckner et al. [47].

Chapter 2

Experiment

2.1 Introduction and motivation

The influence of the pore fluid pressure on the behavior of a granular solid skeleton is well known from research on e.g. fluidized beds or soil liquefaction: Increased pore pressures lead to a decrease in contact stresses between the grains, potentially to an extent where the contact stresses go to zero, and the solid skeleton loses its ability to sustain shear stresses - the solid skeleton liquefies. This causality is described by the principle of effective stress, first proposed by Terzaghi [82] and extended by Biot [9]. According to this principle, the total stress \mathbf{T} in a solid-fluid mixture is related to the effective stress \mathbf{T}_E^s of the solid skeleton and the pore pressure p by

$$\mathbf{T} = \mathbf{T}_E^s - \alpha p^f \mathbf{I}, \quad (2.1)$$

where \mathbf{I} is the unit tensor. The coefficient α is called Biot's coefficient, and is given by

$$\alpha = 1 - \frac{K^m}{K^s}, \quad (2.2)$$

where K^m and K^s are the effective bulk modulus of the granular solid skeleton and the bulk modulus of the solid material, respectively (cf. [84]). Note that the bulk moduli of the solid material alone and the solid skeleton, which consists of an assembly of solid particles, may be massively different. While the material bulk modulus is a material property, the skeleton bulk modulus depends mainly on the contact forces between the grains.

Depending on the degree of consolidation, a granular solid skeleton will usually react to deformation by rearrangement of the grains rather than by a deformation of the solid grains themselves. When a granular solid skeleton is unconsolidated (e.g. beach sand or the glass beads used in the experiment described below), $K^s \gg K^m$, so that $\alpha \rightarrow 1$, and the effective stress principle reduces to

$$\mathbf{T} = \mathbf{T}_E^s - p^f \mathbf{I}. \quad (2.3)$$

Theories on fluidized beds and soil liquefaction assume an increase in pore pressure that *leads to* the failure of the porous skeleton. In soil liquefaction the pore pressure increase is a feedback effect that is created by compaction of a loose, unconsolidated material, e.g. due to earthquakes. However, for the actual liquefaction a high enough

pore pressure is a prerequisite. In this sense, variations in the pore pressure can be seen as a precondition for the onset of flow of the porous skeleton. In fluidized beds, a fluid is pumped through the unconsolidated porous medium from below, so that the pore pressure again acts as a precondition for fluidization. The pore pressure is a control variable. The idea of the experiments presented in this chapter is to study the feedback effects between fluid pressure and bulk flow behavior when the pore pressure is not a control variable, but when, instead, the failure of the unconsolidated, fluid-saturated porous skeleton is induced by a local weakness. One specific example is the collapse of the historical archive of the city of Cologne, Germany in 2009. The collapse was apparently caused by the failure of a diaphragm wall in a subway excavation pit near the building (i.e., a local weakening of the porous skeleton), which caused an underground landslide and led to the development of a cavity underneath the building. The building then collapsed into the cavity. On a more abstract level, it is not difficult to imagine that other types of catastrophic landslides and debris flows may not be caused by the ensemble failure of a large body of soil due to heavy rainfall increasing pore pressures, but by a rather local imperfection that propagates (whatever the onset mechanism may be) through the porous skeleton as a porosity wave, leading to sequential failure of certain areas of soil, and thereby creating the often surprisingly large extent of debris flows.

To get an insight into the aforementioned problems, experiments were carried out, with a focus on the onset of flow of the fluid-granular mixture. The experimental procedure involved mono- or bi-disperse mixtures of glass beads of different sizes that were poured into a container and then saturated with water. At the beginning of an experiment, a hatch was opened at the bottom of the container to allow the fluid-saturated granular mixture to flow out. During the experiments, grain velocities were monitored by Particle Image Velocimetry, further described in Section 2.3. The pore pressure was measured by absolute pressure sensors over the full duration of an experiment, and by high-precision dynamic pressure sensors at the onset of flow.

2.2 Experimental setup

The experimental apparatus consists of a $x = 200$ mm wide, $y = 100$ mm deep and $z = 500$ mm high (internal dimensions) rectangular cuboid, with a 40 mm high hatch at the bottom, normal to the x -direction. The full experimental setup is depicted schematically in Figures 2.1 and 2.3. The test rig is a 1 : 20 downscaled version of a similar apparatus used at the Institute and Laboratory of Geotechnics at the Technical University of Darmstadt for flow experiments with gravel-water mixtures (cf. [46]).

The rig was equipped with pressure transducers at different heights in the wall opposing the hatch (Figure 2.3). The pressure sensors measure only the pore fluid pressure. It was constructionally assured that a mechanical contact between the sensors' measuring membrane and glass beads is not possible, that is, there is only water in contact with the membrane. Consequently, the pressures p^f measured here correspond to the true fluid pressure in the presence of only one phase, p^{fR} . We used two types of pressure sensors: (i) Kistler piezoresistive absolute pressure sensors, type 4005BA5A2, in conjunction with 4618A2 amplifiers, giving an analog signal output of 0 – 10 V corresponding to 0 – 500 kPa absolute pressure; and (ii) PCB high resolution, dynamic ICP[®] pressure sensors, type 112A22, giving ± 5 V output, corresponding to ± 345 kPa

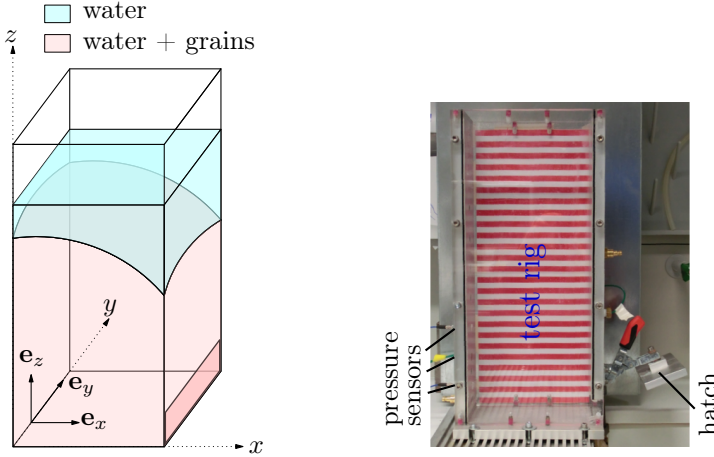


Figure 2.1: Schematic view and photograph of the test rig used for flow experiments

relative to the stationary ambient pressure. The two types of pressure sensors are substantially different: When a step function pressure signal is applied (cf. Figure 2.2), the absolute pressure sensors' output corresponds exactly to the input signal, e.g. when the pressure is increased from 0 kPa to 50 kPa, the output signal changes from 0 V to 1 V accordingly. In contrast, the working principle of a dynamic pressure sensor is rather like that of a microphone: While the output emerging from a step function pressure input signal also reflects the onset time and amplitude of the step function, the output will exponentially decay back to zero if the pressure is constantly kept at the new level. The decay time depends on a couple of factors, the most important one being the discharge time constant (DTC). The DTC determines the time in which a step function input signal decays from 100 % to 37 % of its original value. As a rule of thumb, in the first 10 % of DTC, time and signal decay have a linear one-to-one relationship, i.e. if the sensors have a DTC of 1 s - which is the DTC of the sensors used in this experiment - then within the first 0.1 s of the experiment, 10 % of the signal decay. A good introduction into dynamic pressure measurement can be found on the PCB webpage [2].

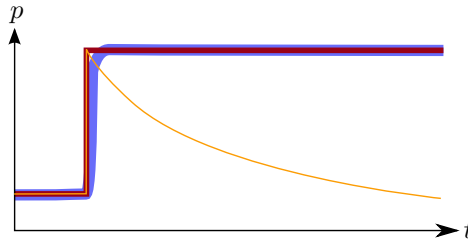


Figure 2.2: Illustration of the reaction of absolute and dynamic pressure sensors to a step function pressure input. The pressure is depicted in red. The absolute pressure sensor output signal, depicted in blue, follows with a slight delay and contains relatively much noise. The signal stays on the new, higher level. The dynamic pressure sensor output signal, depicted in yellow, follows the input pressure almost instantaneously and contains very little noise. The signal decays back to zero.

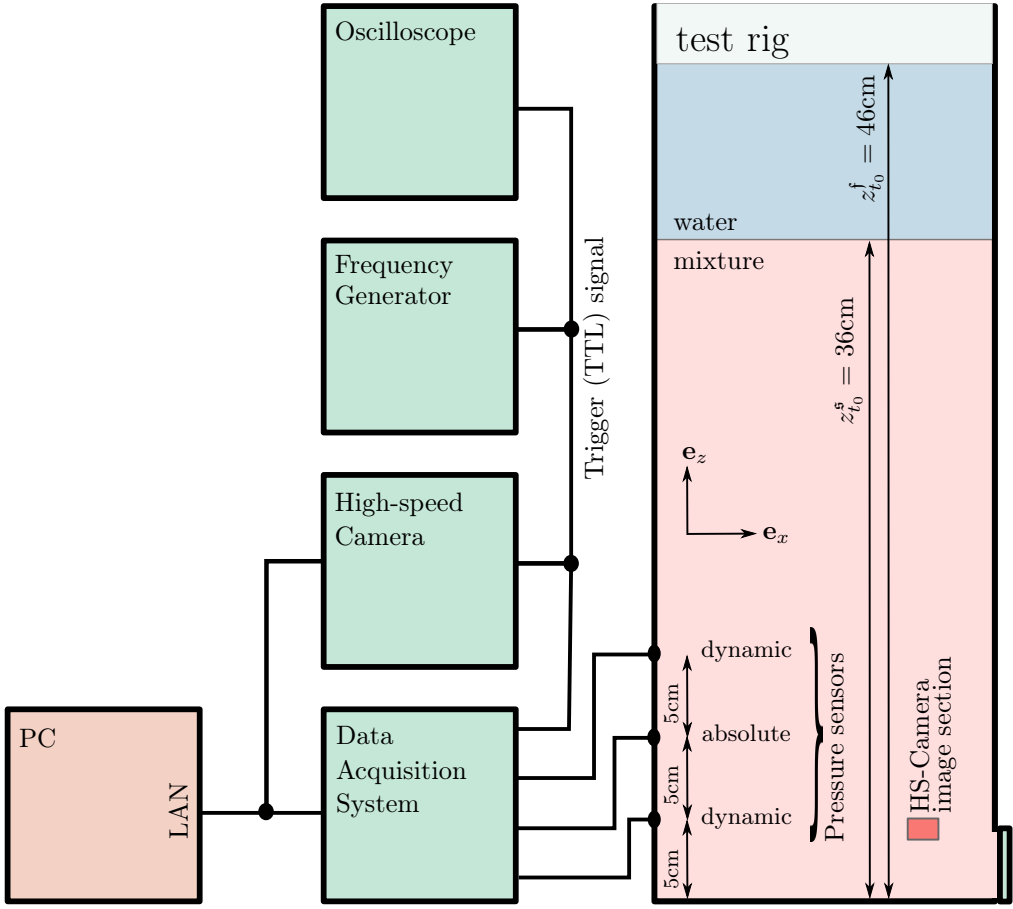


Figure 2.3: Overview of the experimental setup. The initial filling level of glass beads is denoted by $z_{t_0}^s$, and the filling level of water is $z_{t_0}^f$.

While dynamic pressure sensors can only measure absolute pressures on relatively short timescales, and short-lived oscillations on longer timescales, their advantage lies in their temporal and amplitude precision. In practice, we measured a signal noise of ≈ 400 Pa with the static Kistler sensors, while for the dynamic sensors the noise was ≈ 15 Pa. The resonant frequencies are 100 kHz and 250 kHz for the Kistler and PCB sensors, respectively. The use of both types of sensors allowed for the investigation of high-resolution pressure signals on a short timescale of 0.1 s at the beginning of the experiments, and over the timescale of a complete experiment at a lower resolution. The pressure sensor data were recorded at a sampling rate of 96 kHz using an HBM QuantumX MX410B data acquisition system and processed using the HBM acquisition software catman AP.

A high-speed camera Phantom v4.3 was used to capture grain movement in detail at 1000 frames per second for a maximum of 4.5 s. The image data were processed using the Phantom Camera Control application PCC. The resolution of 800x600 pixels corresponds to an image section of $\approx 17.5 \times 13$ mm. For the largest grains, the camera was positioned slightly further away from the test rig, yielding an image section of $\approx 26 \times 19.5$ mm. We used a frequency generator to create a trigger signal to start the high speed camera. To synchronize data from the camera and the pressure sensors, the

trigger signal was also recorded by the data acquisition system. The hatch was opened manually when the trigger signal turned to "on", as indicated by an oscilloscope (cf. Figure 2.3). A conventional digital compact camera Casio Exilim EX-ZR200 captured the total view of the test rig at 240 frames per second and a resolution of 430x320 pixels during each experiment.

no. experiment	L0.1 L0.2	L1.1 L1.2	L2.1 L2.2	L3.1 L3.2	L4.1 L4.2	L5.1 L5.2
grain size [mm]	no grains	0.5	2	4	0.5 (50%) 2 (50%)	0.5 (50%) 4 (50%)

Table 2.1: Grain sizes used in experiments

The series of experiments described here includes twelve experiments, cf. Table 2.1. Each experiment was repeated once to check data consistency. Two experiments (L0) were conducted using only water, without glass beads. Experiments L1 to L3 involved the use of monodisperse (uniform grain size) grain-water mixtures; with the grain diameter increasing from experiment L1 to L3. Four experiments (L4 and L5) were conducted using bidisperse mixtures (two distinct grain sizes).

The experiments were set up as follows: First, the test rig was filled with tap water to about one third. Then, a scoop of glass beads was carefully submerged to avoid excessive air entrainment, and then allowed to sink to the bottom of the test rig. In case of bidisperse mixtures, the grain sizes segregated due to their different sedimentation velocities, and the grains settled in layers. To ensure a homogeneous distribution of grains at the beginning of an experiment, the mixture was stirred each time after adding a 5 cm layer of grains. This procedure worked surprisingly well and resulted porous mixture that looked satisfactorily homogeneous and isotropic.

2.3 Results

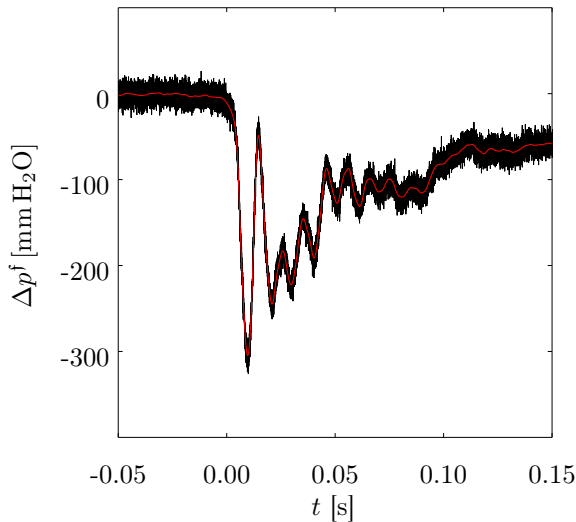


Figure 2.4: Unfiltered (black) and filtered (red) absolute pressure signal

Due to the high amount of noise in the absolute pressure signal, the data were filtered using a 300 Hz low pass filter for better readability. No hardware filter was used to avoid loss of any potentially important information. The open-source Python framework ObsPy [8], originally intended for processing seismological data, was used for filtering. A comparison of the unfiltered and filtered signal for experiment L0.1 shows that the frequency content of interest is still present in the filtered signal, while the noise is reduced (Figure 2.4). All pressures are given in mm H₂O, for easy comparison to the hydrostatic pressure ρgz expected from the water level, z . Note that for each experiment the time $t = 0$ was set manually to the moment when the pressure curves significantly deviated from zero.

The high-speed image data were processed using Particle Image Velocimetry (PIV). Originally, PIV emerged as a non-intrusive technique to measure fluid flow processes. In a nutshell, PIV works as follows: A small number of neutrally buoyant tracer particles is added to the fluid. During the flow process, two or more images of the flow including tracer particles are captured. Each image is subdivided into several so-called interrogation windows. The average displacement vector between two successive images is then approximated for each interrogation window using a cross-correlation technique. During the last two decades, PIV has found more and more application in the field of granular flows, see e.g. [24, 58, 77]. This extension is somewhat natural because a granular flow contains ‘tracer’ particles by definition.

In this study, the open-source program JPIV [1] was used for PIV analysis. The size of the interrogation windows was set such that each interrogation window would contain at least six to ten particles. It turned out that an interrogation window size of 64 pixels for experiments involving 0.5 mm glass beads yielded the best results, and 260 and 300 pixels for 2 mm and 4 mm glass beads, respectively. One displacement field was obtained for each subsequent pair of images from the high-speed camera. The analysis of the data revealed significant outliers in each of the displacement fields. These outliers are presumably due to an effect described by Eckart et al. [24]: The cross correlation technique used for the calculation of the displacement fields relies on the assumption that each pair of subsequent images contains the same information - here, the same grains in the same configuration - only displaced by a certain value that is calculated by the cross-correlation. The type of granular flow investigated here, however, is not entirely two-dimensional, but may contain a component normal to the image section. Thus, grains might leave the image section towards the inside of the test rig and be replaced by other grains between two image frames. Another problem, also noted by Eckart et al. [24], arises because the grain assembly is not only displaced, but also deformed during the flow process, which also cannot be captured by cross-correlation. However, robust and well-tested techniques are implemented in JPIV (see [1] and citations therein) to find such outliers by a normalization procedure. The outliers were then replaced by the median for each displacement field. Further data processing involved the calculation of the average velocity from each displacement field. Moreover, the gradients of the velocity fields were calculated and averaged over the whole field, yielding information about average shear rates and divergence of the granular flow within the image section. Valuable PIV data could only be obtained for the beginning of the experiments; at later times the grain velocity is so high that the high-speed images, although involving short exposure times of 830 μ s, become blurred, and the resulting velocity data are very noisy.

The flow process can be subdivided into five different stages, as described in Section 2.3.1, and the total view videos were used to decide when each of the stages was fully

developed. Results for selected experiments are shown in Table 2.2.

To understand the processes during the outflow of granular-fluid mixtures from the test rig, it is illustrative to first describe in a qualitative manner all macroscopic observations, and to compare these observations with the absolute pressure data. This is done in the following subsection. After that, the focus is turned to the first 0.1 s of the experiments, and the high-speed image data are analyzed together with the high-resolution pressure data from the dynamic pressure sensors.

2.3.1 The phenomenology of an experiment

For simplicity, let us start with the *reference* experiment L0.1 that uses only water instead of a mixture. The flow process can roughly be subdivided into three intrinsic timescales, denoted by Δt_1 , Δt_2 and Δt_5 , see the upper left plot in Figure 2.5. At time $t = 0$, the hatch is opened, and water immediately starts to flow out. The pressure decreases to approximately the atmospheric pressure (-360 mm H₂O, because the pressure sensor is installed 360 mm below the initial water level) during Δt_1 . The pressure then returns to the hydrostatic pressure during Δt_2 . During the last period of the experiment, Δt_5 , the observed flow pattern is relatively stationary, and the pressure coincides with the hydrostatic pressure $\rho g z$ expected from the optically observed water column height z . The mixture experiments involve two additional time periods Δt_3 and Δt_4 that are not seen in the single-phase (water) experiments.

no. experiment	L0.1	L1.1	L3.2	L4.2
hatch opens (Δt_1)	0 s	0 s	0 s	0 s
flow starts ($\Delta t_{2,3}$)	0 s	0.4 s	0 s	0 s
flow fully developed (Δt_4)	0.1 s	2.1 s	0.6 s	1.4 s
grain surface reaches hatch (Δt_5)	no grains	4.3 s	1.0 s	4.1 s

Table 2.2: Different stages of flow as inferred from total view video sequences

Let us now refer to the *mixture* flow experiment L1.1 involving small (0.5 mm) grains. Here and in all other mixture flow experiments, five intrinsic timescales Δt_1 to Δt_5 can be discriminated, see the upper right plot in Figure 2.5. Upon opening of the hatch, the pressure drops within Δt_1 . Note that the pressure drop is stronger in amplitude than for pure water. At the same time, as observed during the experiments, high-speed images show that the grains visibly accelerate for a very short time, but then almost cease to move. In the next period Δt_2 , the pressure recovers slightly. Yet, it remains well below the hydrostatic pressure $\rho g z$, and even decreases further during the next period, Δt_3 . Macroscopically, it can be seen in the videos that clumps of grains fall out of the test rig at the opening, and the high-speed images indicate that the grains near the hatch move very slowly. The beginning of Δt_4 marks a clear transition, visible in the videos, from the very stagnant behavior observed so far, that was characterized by slow water flow and clumps of grains shearing off the bulk granular skeleton near the hatch, to a fully developed, stationary bulk flow of the granular-fluid mixture. Meanwhile, the pressure increases, and reaches the hydrostatic level $\rho g z$ at the end of Δt_4 . The high-frequency noise during this period is due to the high acoustic noise intensity created by the fast outflow of glass beads. Finally, at the beginning of Δt_5 , the uppermost layer of grains reaches the upper edge of the hatch, letting the remaining water flow out freely and unobstructed by grains. Time periods $\Delta t_{3,4}$ have no correspondence in the single-phase experiments. During Δt_5 ,

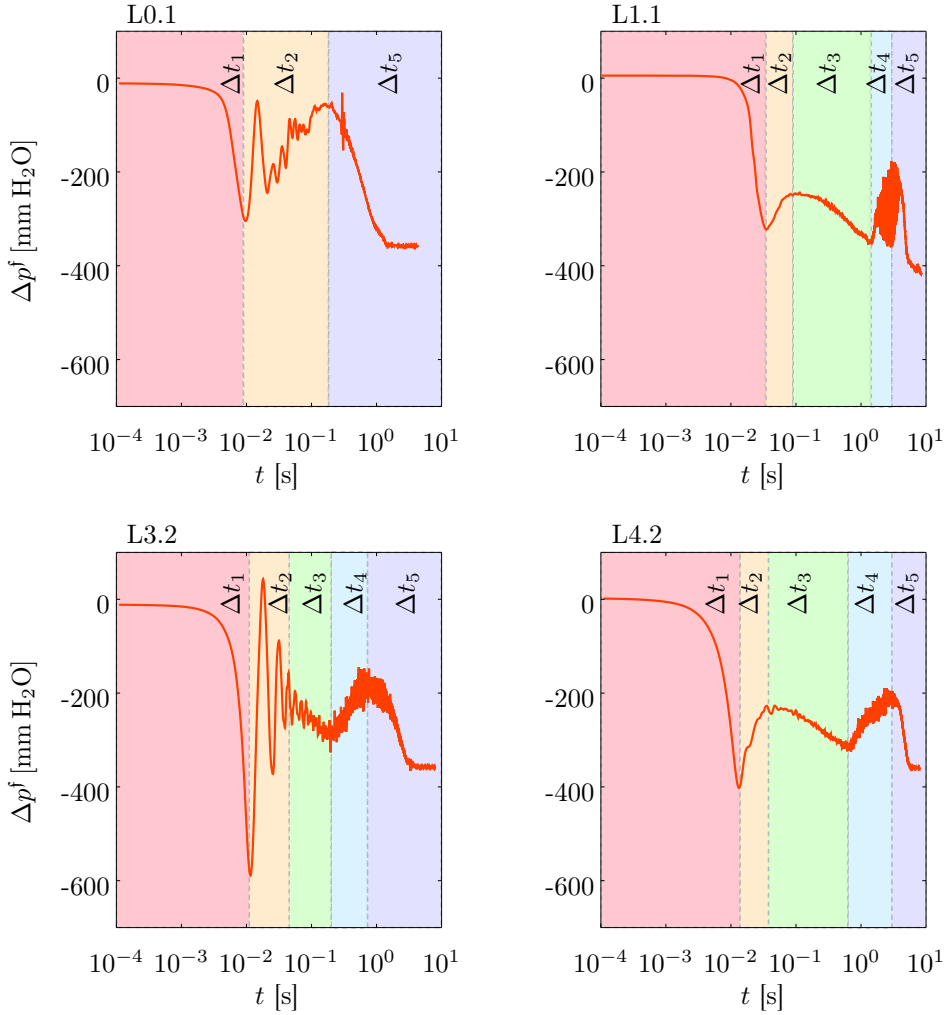


Figure 2.5: Fluid pressures and intrinsic time scales of experiments on a semi-logarithmic scale. Each panel exemplarily depicts one type of experiment: no grains (upper left), small grains (0.5 mm, upper right), larger grains (4 mm, lower left), bidisperse mixture (2 mm and 0.5 mm, lower right).

however, the pressure curves for both the single-phase reference experiments and the mixture experiments are similar and correspond to the hydrostatic water level.

The experiments L4 and L5 involving *bidisperse mixtures* (lower right plot in Figure 2.5 shows experiment L4.2) are very similar to the experiments L1 involving 0.5 mm grains. Note, however, that the absolute pore pressure drops slightly below the atmospheric pressure. The experiments L2 and L3 involving larger (2 and 4 mm) grains show similarities to both the single-phase experiment L0 and the small grain experiments L1, L4 and L5 described above. The lower left plot in Figure 2.5 shows experiment L3.2. At the beginning, the grains immediately start to flow; a deceleration of the grains, as in the small grain experiments, is not macroscopically visible in the high-speed image data. Yet, the flow starts much less vigorously than the outflow of water, and one can discriminate between a developing flow from Δt_1 to Δt_3 and a fully developed flow during Δt_4 (cf. Table 2.2). The boundaries between the different stages of the flow are not very clear during the first three time periods, which is also reflected in the pressure time series. The boundary between Δt_4 and Δt_5 is clearly existent, but much less distinct. Note the amplitude of the initial pressure drop, $-590 \text{ mm H}_2\text{O}$, i.e., $230 \text{ mm H}_2\text{O}$ below atmospheric pressure.

2.3.2 Particle Image Velocimetry and high-resolution pressure data

The dynamic pressure sensors measure pressure differences on short time scales; and absolute pressures can only be inferred from the data shortly after an initial pressure perturbation. Hence we now focus on the first 0.1 s after the beginning of an experiment (corresponding to Δt_1 and Δt_2), as the signal decay on this time scale is less than 10%. Figures 2.6 and 2.7 show dynamic pressure sensor data along with absolute values of y - and z -velocity components obtained from PIV analyses for all twelve experiments. The fluid pressure axes have the same scaling in all twelve plots; however, the velocity axes were grouped into the small grain experiments (0.5 mm, L1), large grain experiments (2 and 4 mm, L2 and L3), and bidisperse mixtures (L4 and L5); and only the velocity axes in each group have equal scaling.

Let us investigate some commonalities of all granular flow experiments. First, note that in all experiments the beginning of the pressure drop coincides with an increase in grain velocity. As the pressure drops further, the grain velocity decreases again. For the larger monodisperse mixtures, this effect is less distinct. In all experiments, the initial pressure drop at the beginning of an experiment is larger than for pure water. At $t = 0$, the test rig is filled with 460 mm of water, so for the lower sensor, installed 50 mm above the bottom of the test rig, atmospheric pressure corresponds to $-410 \text{ mm H}_2\text{O}$. In most experiments, this pressure is even undercut for a short time during the initial pressure drop. The smallest pressure drop occurs in case of the 0.5 mm grains, while the pressure drop is largest for the 4 mm grains, $239 \text{ mm H}_2\text{O}$ below atmospheric pressure in experiment L3.2. In case of the single-phase experiments L0, the data from both pressure sensors almost coincide; while in case of the mixture experiments, the *lower* pressure sensors (depicted by the red lines) show a significantly lower pressure - although the hydrostatic pressure, i.e., the water head is *higher* for this sensor, and both sensors were calibrated to zero at the beginning of an experiment. Data collected in preparatory experiments using two absolute pressure sensors show that this difference is maintained until the beginning of Δt_5 . At this time, when the grain surface reaches the hatch, the two pressure time series switch their positions,

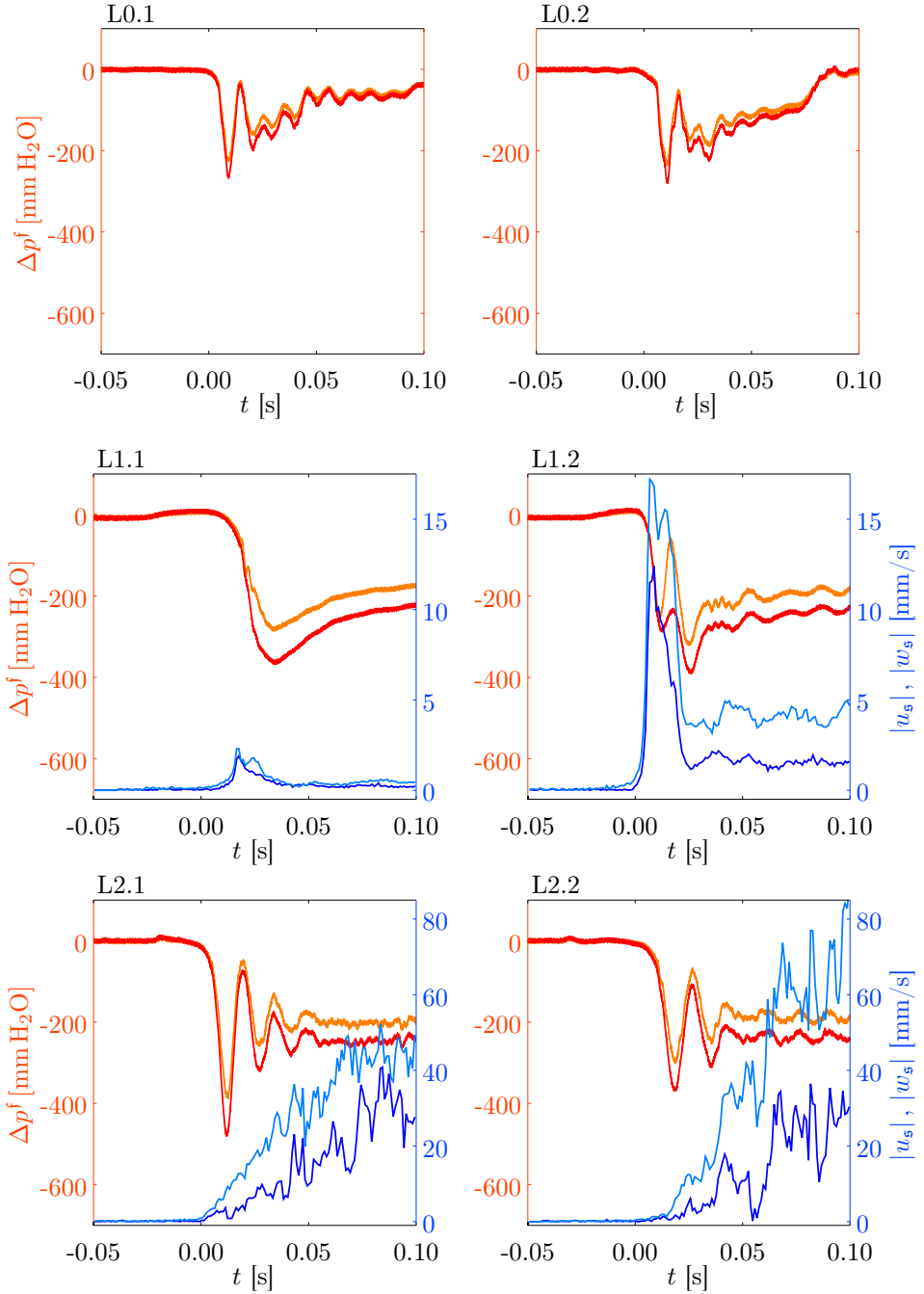


Figure 2.6: Fluid pressures and grain velocities for the experiments L0 (top), L1 (middle), L2 (bottom). Orange / red: upper and lower dynamic pressure sensor; dark / light blue: absolute value of grain x - and z -velocities obtained from PIV measurements

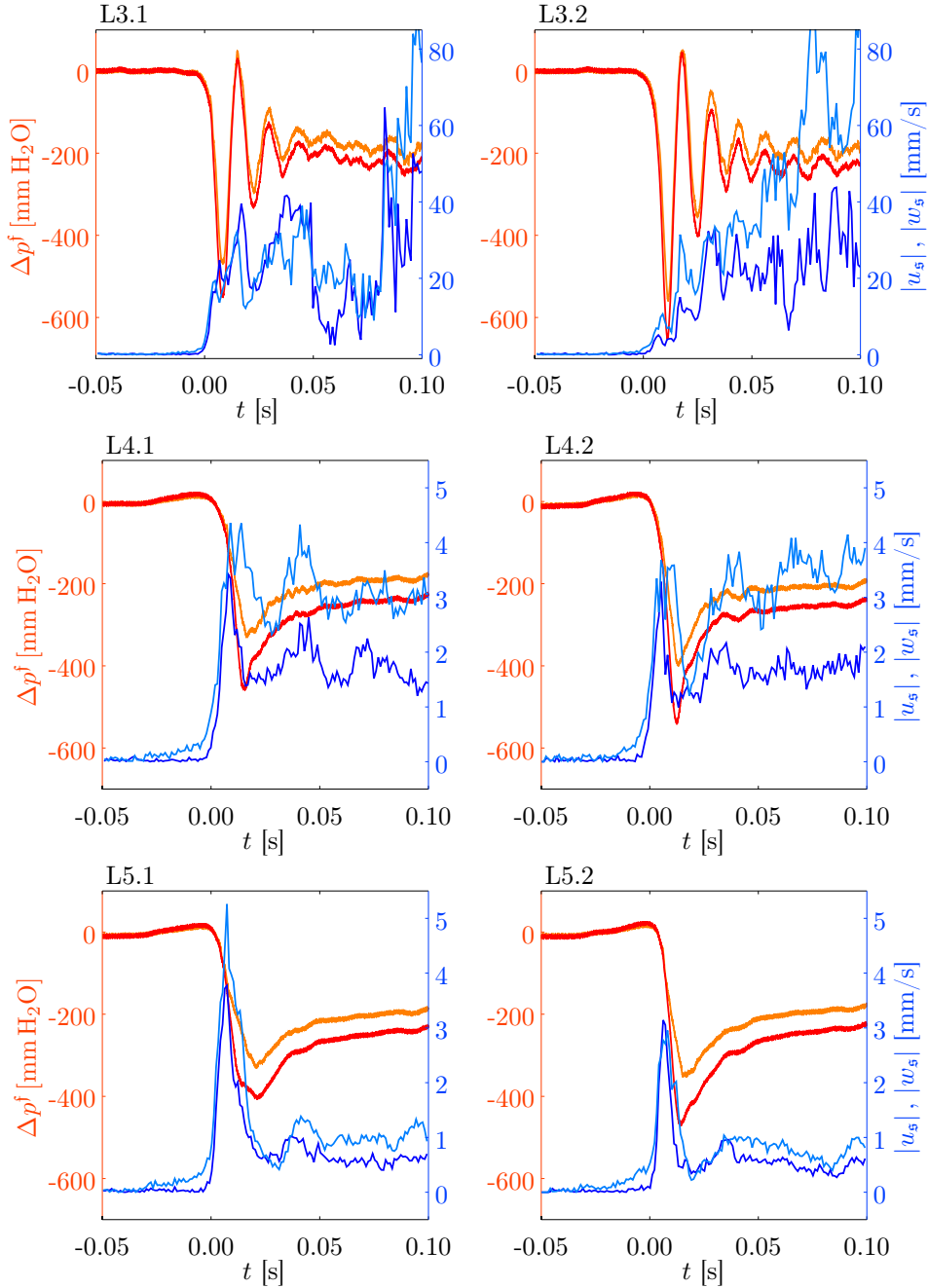


Figure 2.7: Fluid pressures and grain velocities for the experiments L3 (top), L4 (middle), L5 (bottom). Orange / red: upper and lower dynamic pressure sensor; dark / light blue: absolute value of grain x - and z - velocities obtained from PIV measurements

and the lower pressure sensor shows a higher pressure, as could be expected from the hydrostatic water level.

The first four plots in Figures 2.8 and 2.9 depict the elements of the (non-symmetric) velocity gradient tensor with respect to a Cartesian system, as inferred from the high speed image data:

$$\text{grad } \mathbf{v}_s = \begin{pmatrix} \frac{\partial u_s}{\partial x} & \frac{\partial u_s}{\partial z} \\ \frac{\partial w_s}{\partial x} & \frac{\partial w_s}{\partial z} \end{pmatrix}, \quad (2.4)$$

with $\mathbf{v}_s = [u_s \ w_s]^T$, and u_s and w_s the x - and z -components of the velocity vector of the solid grains, respectively. In (2.4), we have assumed planar flow, i.e., for the velocity v_s in y -direction we have $v_s = 0$, and likewise for the derivatives in y -direction $\frac{\partial \bullet}{\partial y} = 0$. All zero components were omitted in the definitions of \mathbf{v}_s and $\text{grad } \mathbf{v}_s$. The partial derivatives in (2.4) were computed in Matlab[®] using the gradient function, which employs a central difference scheme for interior data points, and single-sided differences at the edges of a matrix. The diagonal elements of the velocity gradient tensor contain information on the volumetric deformation of the porous skeleton, while the non-diagonal elements contain information on rotation and shear. The rate of volume deformation is given by the divergence of velocity, that is, the sum of the diagonal elements of the velocity gradient tensor,

$$\text{div } \mathbf{v}_s = \frac{\partial u_s}{\partial x} + \frac{\partial w_s}{\partial z}, \quad (2.5)$$

(lower left plots in Figures 2.8 and 2.9) and the (rotation-free) shear rate is given by the symmetric part of the velocity gradient tensor, that is, the average of the non-diagonal elements,

$$\text{dev } \mathbf{v}_s = \frac{1}{2} \left(\frac{\partial u_s}{\partial z} + \frac{\partial w_s}{\partial x} \right) \quad (2.6)$$

(lower right plots in Figures 2.8 and 2.9).

Experiments L1.1 and L5.2 were arbitrarily chosen to be shown here; the respective plots are qualitatively similar for all experiments. The signal-to-noise ratio is relatively low in these plots. However, at the time of the initial pressure drop, a peak can be recognized in each of the plots. While experiment L1.1 shows compaction in x - and dilation in z - direction, experiment L5.2 shows exactly the opposite. Due to the fact that the derivatives in both directions have opposite signs, almost no signal is observed in the divergence plots. After the initial pressure drop, however, compaction is observed in experiment L1.1 and dilation in experiment L5.2; however the signal is relatively close to the noise. The signals are clear enough to state that the granular skeleton is being sheared within the interrogation window.

2.4 Discussion

The flow has to pass through a reduced cross section at the outlet. Hence the movement of the granular phase cannot be purely translational or rotational; instead, it has to fluidise in order to pass through the outlet. It is a common and reasonable observation that when an assembly of grains fluidises, its porosity increases, i.e., it behaves dilatant. This porosity increase can easily be understood by considering the

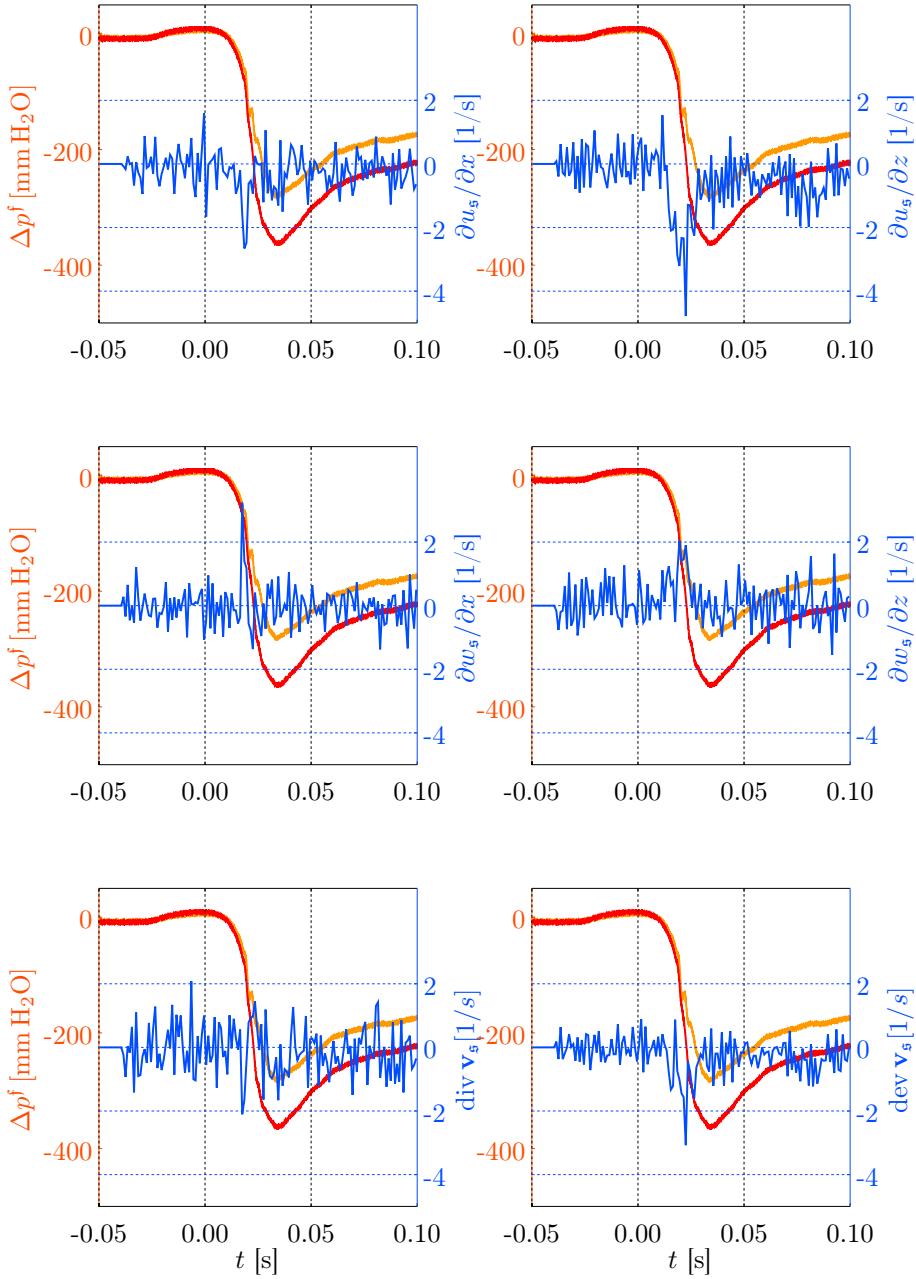


Figure 2.8: Dynamic pressure sensor data (orange and red) with averaged derivatives of the velocity fields (blue) for experiment L1.1

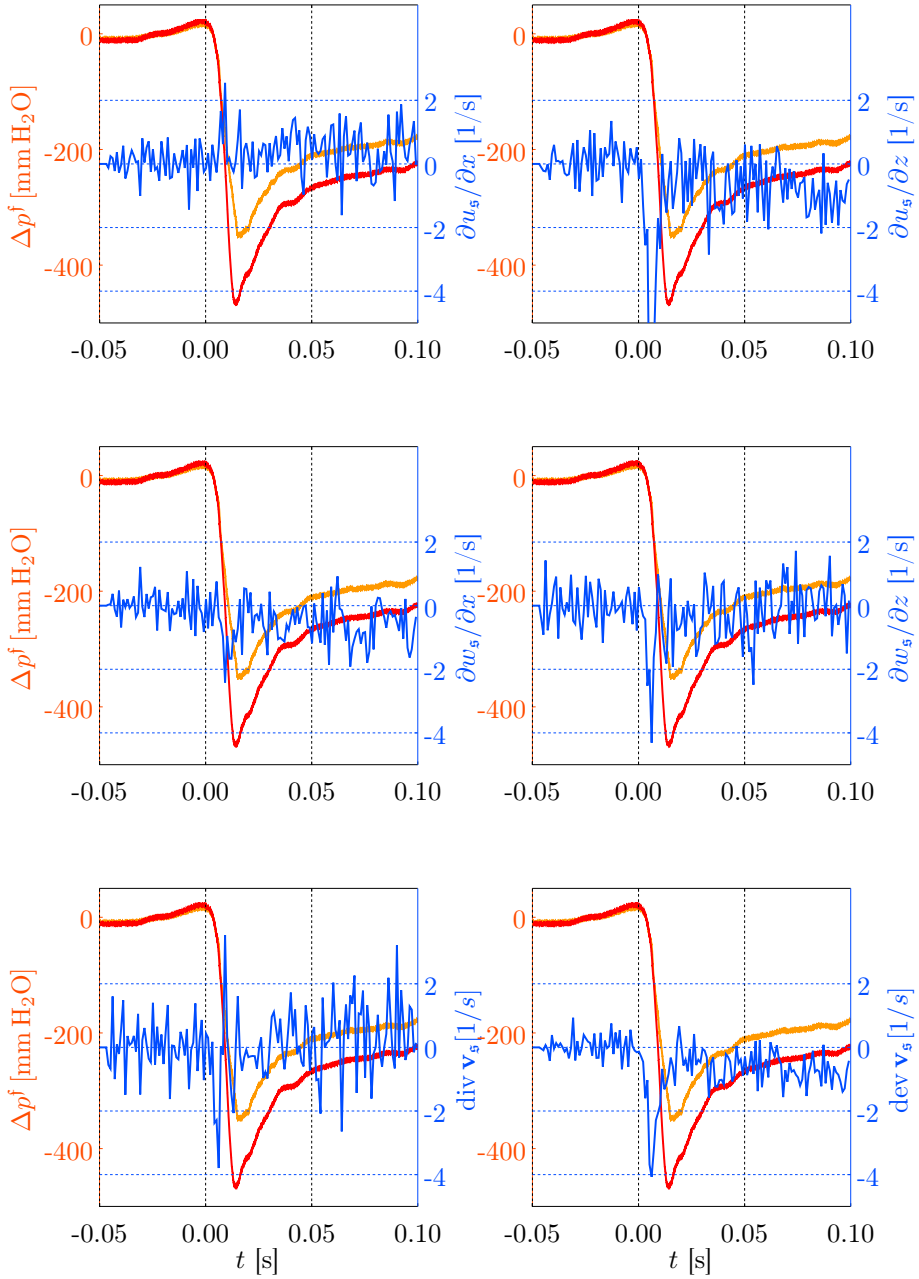


Figure 2.9: Dynamic pressure sensor data (orange and red) with averaged derivatives of the velocity fields (blue) for experiment L5.2

process of granular fluidisation on the grain scale. Consider some neighboring layers of grains (Figure 2.10). At random close packing, the grains of one layer come to rest in the voids between the other layer's grains. In order to pass one another, the layers first have to dislodge from one another, thereby increasing the porosity. Under fully undrained conditions (i.e., no water inflow into, and no water outflow from the pore space), and if the pore fluid is compressible, a porosity increase must lead to a decrease in fluid pressure, because the fluid's volume increases while its mass remains constant. The pressure drop will be stronger for a less compressible fluid, and in the theoretical limit of an incompressible fluid, the pressure would instantaneously drop to zero. Under fully drained conditions (free water inflow into, and water outflow from the pore space), a porosity increase leads to fluid inflow, while the fluid pressure remains constant. In case of the experiments described here, the conditions are fully drained only near the interface between grains and water; away from the interface, drainage is inhibited by the finite permeability of the porous skeleton. Hence we can postulate that a porosity increase within the porous medium may lead to a local, instantaneous, short-lived pressure decrease, if the pore fluid is as little compressible as water.

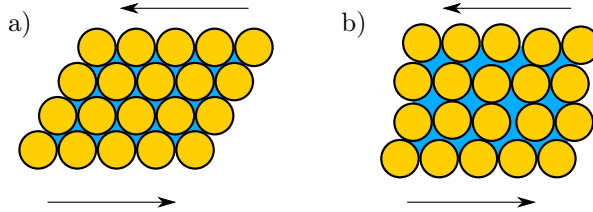


Figure 2.10: Illustration of a fluidizing assembly of grains. Grains are depicted in yellow, pore space in blue. On the left, the grains are closely packed. In order to move as indicated by the arrows, the grain layers first have to dislodge from each other, thereby increasing the porosity.

Adopting the assumption made above that the porous skeleton behaves dilatant when it fluidises, and that dilatancy causes a local, instantaneous decrease in pore pressure, the results outlined in Section 2.3 can be interpreted as follows: The local instantaneous fluid pressure gradient is immense when the hatch opens at the beginning of Δt_1 : The fluid pressure just near the hatch drops to the atmospheric pressure, while the pressure a short distance away is still the initial hydrostatic pressure. The fluid reacts with a strong acceleration towards the hatch, thereby accelerating the grains via viscous drag. An indication of how strong the fluid is locally accelerated is given by the fast and vigorous onset of flow in case of the single-phase experiments. In parallel to the acceleration of both phases, the fluid pressure drops. According to Terzaghi's principle, cf. equation (2.3), the effective stress of the solid skeleton is increased when the pore pressure is decreased; so that the grains are effectively consolidated due to the pressure drop. The consolidation of grains may lead to the subsequent reduction of their velocity, although this effect seems to depend on the actual composition of the solid skeleton, and is less pronounced or even inexistent for larger grain sizes. If the assumption holds that the granular medium behaves dilatant, then dilatancy may explain why the initial fluid pressure drop is stronger in case of the experiments with glass beads than in case of the single-phase experiments: Using the definition of the

bulk modulus,

$$K = -V \frac{dp}{dV}, \quad (2.7)$$

where p represents the fluid pressure, V is the fluid volume, and a value of $K = 2.2 \text{ GPa}$ for water, it can be inferred that under undrained conditions a change in pressure of $100 \text{ mm H}_2\text{O}$, which is in the range of magnitudes observed in the experiments, is obtained by a decrease of only $4.5 \cdot 10^{-3}$ per cent of volume. In other words, in a confined container completely filled with water saturated glass beads, a porosity increase in the fifth decimal place causes a pressure decrease of $100 \text{ mm H}_2\text{O}$. As the fluid pressure is measured locally within the porous medium at some distance from the interface between grains and pure water, a porosity increase due to dilatancy may well serve as an explanation for the stronger pressure drop during Δt_1 compared to the fluid-only experiments. The drainage appears to be insufficient to maintain hydrostatic pressure within the pore space. Water entering into the porous medium from above due to the pressure gradient should lead to an increase in pressure up to the hydrostatic pressure, while porosity production should lead to a decrease in pressure. The hypothesis of insufficient drainage is supported by the observation that the lower of the two sensors experiences the lower pressure, although both sensors were calibrated to zero at the beginning of each experiment. One more indication is given by the fact that experiments L2 and L3, involving larger grain sizes and hence higher permeability, show higher pore pressures during Δt_2 , possibly resulting from better drainage. Note that the change in porosity $\Delta\phi$, where porosity $\phi = dV^f / (dV^s + dV^f)$, and dV^f and dV^s denote the fluid and solid volume, respectively, is not only determined by a non-constant fluid volume, but also a non-constant solid volume.

Unfortunately, the high-speed image data quality remains too uncertain considering resolution and accuracy to directly quantify the amount of porosity increase. Yet, the image section represents only a small portion of the entire test rig, and to estimate more precisely the influence of porosity production on the pore pressure, measurements of the grain velocity gradient over a larger image section are necessary. The small size of the image section may also serve as an explanation for the somewhat surprising result that the porous medium is compacted in x -direction and dilated in z -direction at the beginning of experiment L1.1. It would be plausible to observe exactly the opposite, as in experiment L5.2, because we expect acceleration of the grains in x -direction (towards the outlet), while due to the overburden together with the pressure drop, compaction in z -direction would not be surprising. It is concluded that the data quality must be improved to exactly quantify porosity increase.

At the end of Δt_1 , the fluid pressure has dropped to its minimum. Meanwhile, the grains have slowed down (depending on the grain size), but have not entirely ceased to move. If we again assume that the grains behave dilatant, their movement causes a local increase in fluid volume, and the fluid pressure does not return to the hydrostatic pressure, but remains somewhat lower during Δt_2 . Yet, the pressure increase might assist in further fluidising the grains by reducing the effective stress. During Δt_3 , the pressure decreases yet again, accompanied by an increase in grain velocity. If we further follow the argument of a dilatant porous skeleton influencing the fluid pressure, we may interpret the observation as follows: The porous skeleton increases in velocity due to further fluidisation, i.e. the pore space is further increased, thereby reducing the apparent viscosity of the solid phase and reducing the fluid pressure. This process continues until a steady state flow is reached at the beginning of Δt_4 . The following pore pressure increase could be interpreted as follows: First, the gran-

ular surface moves towards the sensor, so that the porous layer between sensor and pure water diminishes. Second, the production of new pore space does not increase anymore, but is steady, because the outflow is in steady state. Together, these effects may lead to an increase in pressure up to the hydrostatic pressure. Finally, the hydrostatic pressure curve during Δt_5 can be explained with the apparent change in flow mechanism; water can now flow out freely above the grain layer, and hence the pressure is simply hydrostatic.

Let us shortly review the repeatability of the experiments. Clearly, the grain velocity data of the two experiments L1 show a striking difference of almost one order of magnitude in the measured grain velocities, although the experimental setup is identical. However, in the other experiment pairs, the results are reasonably comparable; and even in case of the experiments L1, the observed trends (a velocity peak accompanied by a pressure drop; subsequent pressure recovery and development of a stationary velocity) are the same as in all the other experiments. If experiments L1 are compared to experiments L4 and L5, both also involving 0.5 mm grains, experiment L1.2 could be labeled as an outlier to all other experiments. There are two possible reasons for the observed differences in experiments L1, but also in the other experiments. The main disadvantage of the experimental setup is the manual operation of the hatch. Although it was assured that always the same experimenter opened the hatch using a standardized procedure, a non-automatic operation may lead to erratic results. The second possible source of error is more subtle and concerns the complexity of the experiment. Both pressure and PIV measurements were conducted in-situ at discrete spatial positions. The exact behavior of the porous medium, for example the development of a specific shear band, however, may not be deterministic – in one experiment, the shear band might be visible in the high-speed image data, in another experiment the shear band might pass just next to the image section. Summing up, however, the expressed criticism does not contradict any of the conclusions drawn from the data, because all conclusions rely on qualitative trends rather than quantitative data in the measured time series, and these trends appear to be robust.

2.5 Conclusions

Experiments were conducted using a relatively simple setup to study the flow behavior of water-saturated glass beads close to the dense packing limit. A combination of measurement techniques operating at different spatial and temporal scales was used: in-situ absolute and dynamic, high-resolution pore pressure measurements at different spatial positions, and grain velocity measurements inferred from Particle Image Velocimetry. Together with simple visual observations of the flow behavior of the mixture inferred from slow-motion video recordings, we conclude:

- the flow is dominated by strong feedback effects between pore pressure and the grains' flow behavior. If we attribute an apparent viscosity μ^s to the fluidized solid to describe its resistance to flow, analogous to the dynamic viscosity of a fluid, then this apparent viscosity is largely determined by the increase or decrease in extra stresses due to pore pressure decrease or increase, respectively; i.e. $\mu^s = \mu^s(p^f)$;
- dilatancy (porosity increase) of the fluidizing porous skeleton occurs to be the most important parameter for the determination of the pore pressure;

- although the test rig is open to atmospheric pressure at the top, the conditions within the fluidizing porous medium are not fully drained, that is, a porosity increase is not instantaneously compensated by fluid inflow into the pore space. Instead, the pressure of the compressible pore fluid drops as a reaction to a porosity increase;
- the fluidisation of fluid-saturated, unconsolidated porous media is in principle a self-inhibiting process when resulting from a local weakness in the porous skeleton, because fluidisation of the porous medium leads to a local instantaneous decrease in pore pressure, which in turn increases the effective stresses, potentially stabilizing the porous skeleton. The degree of self-inhibition seems to depend largely on the actual configuration of the porous medium. While self-inhibition is almost negligible in case of the larger grains, its effect seems to increase anti-proportionally to the permeability of the porous skeleton.
- Clues have been given over the whole range of intrinsic time scales regarding the observed flow pattern to be caused by an *interaction of a dilatant, fluidising granular medium with a compressible pore fluid*. The findings emphasize the importance of the coupling between the behavior of grains and fluid. They also show that conventional mathematical/numerical models assuming an incompressible pore fluid are clearly not sufficient to explain the observed behavior, and motivate the development of new models involving a compressible fluid phase.

Regarding future work, it is desirable to increase the accuracy of the PIV measurements in order to quantify the porosity production rate during the experiment. Knowledge of the porosity production rate would allow to calculate exactly the pressure drop associated with porosity increase, and the necessary amount of water inflow from the top to reach the actual measured pressure. A larger image section for the PIV measurements would allow to investigate how fluidization is distributed inside the test rig over time. Moreover, it would be interesting if a porosity wave propagates through the porous skeleton at the onset of flow.

In the series of experiments shown here, the porosity and permeability of the porous medium were varied systematically by using glass beads of different sizes and mixtures thereof; however, clear correlations with the observed flow patterns could not be deduced. An improvement of the hatch opening mechanism might be helpful in establishing such relations.

Preliminary experiments, not shown here, using a slightly different setup without PIV involved the variation of the filling height of glass spheres, thereby varying the ratio between pore pressure and extra stresses. In some cases, increasing the filling levels led to complete stagnation of the granular medium, while decreasing the filling levels led to increased flow rates. A systematic analysis of the data is left for further work.

Chapter 3

Two-phase hybrid continuum mixture model for batch sedimentation

3.1 Introduction and motivation

The behavior of the solid-fluid mixture flow presented in Chapter 2 was interpreted by assuming that the compressibility of the pore fluid is of major importance. Based on this insight, a *hybrid* modeling framework involving an incompressible solid phase and a *weakly* compressible fluid phase is developed. Sections 3.2 and 3.3 introduce the framework and tools necessary for the derivation of a continuum mixture model; the general balance equations are then derived from first principles in Section 3.4, and constitutive laws are added in Section 3.5. The flow described in Chapter 2 is relatively complex, so that as a first step, we resort here to the more simple case of batch sedimentation. However, the balance equations are general enough to allow for extension to the flow presented in Chapter 2 by adding additional appropriate constitutive laws and adjusting the boundary conditions.

Most existing mathematical descriptions of sedimentation are based on the one-dimensional kinematic theory of Kynch [51], which employs a continuity equation for the concentration of sediment particles. The equation is solved using the method of characteristics to give the position of the settling front (interface between clear water and sediment-water mixture at initial concentration) and the bed front (interface between sediment bed and sediment-water mixture). As the term "kinematic" suggests, the model ignores the detailed description of forces on the particles, and assumes that the local solid velocity is a function of the local solid concentration only. A great number of extensions and tailored variants has evolved from this model to account for e.g. sedimentation-consolidation or continuous sedimentation, see [14, 72] for an overview.

Sediment transport naturally involves the sedimentation of particles, beneath erosion and the actual transport process. Studies in this field are abundant, see e.g. [4, 19, 20, 65]. However, the study of batch sedimentation seems largely to be based on Kynch's theory. In fact, there seem to be only three publications to date [15, 53, 54]

that use an implementation of a full continuum mixture model (mass and momentum balances for each phase) for the modeling of sedimentation processes.

All of the above models assume that both phases, solid particles and fluid, are *material incompressible*, that is, the fluid alone or a single solid particle are assumed incompressible, while the solid or fluid *phases* in the mixture might still be compressible due to changes in the volume fraction of the constituents. While the compressibility of water is indeed small, and might be neglected for most types of mixture flows, the importance of effects due to fluid compressibility was shown in Chapter 2, and necessitates the development of new models accounting for the material compressibility of water. Moreover, acoustic and transient effects are not captured by incompressible models. The hybrid model developed here allows the description of both mass transport *and* acoustic effects within the same framework.

3.2 Framework

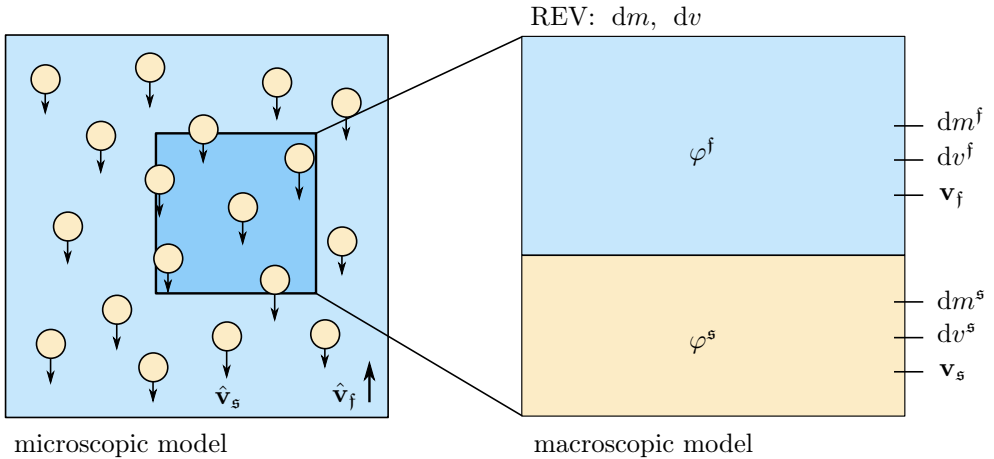


Figure 3.1: Microscopic model (left) and macroscopic model (right), adapted to the present model after [78]. On the microscopic scale, each solid grain and the surrounding fluid have a discrete location and a unique velocity $\hat{\mathbf{v}}_s$ and $\hat{\mathbf{v}}_f$. On the macroscopic scale, these microscopic heterogeneities are not visible, and the phases are instead characterized by their volume fractions and their *average* velocities \mathbf{v}_s and \mathbf{v}_f .

The present model is developed within the framework of Truesdell's [83] Mixture Theory (see [21, 44]). The theory assumes that matter is spread evenly (continuously) throughout the body and fills out the body completely. From an observer's macroscopic perspective outside the body (cf. the macroscopic model in Figure 3.1, right), the microscopic heterogeneities (i.e. the discrete particles, cf. the macroscopic model in Figure 3.1, left) are not visible. In other words, the whole domain, containing the sediment particles and water, is modeled on a macroscopic scale, i. e. as a continuum, with each Representative Elementary Volume (REV) described by the physical properties of a *mixture* $\varphi = \varphi^s + \varphi^f$ where the superscripts s, f are used for the solid and fluid phase, respectively (cf. Figure 3.1).

The behavior of this mixture, according to Truesdell's metaphysical principles, is a superposition of the behavior of its *constituents* α , $\alpha \in \{s, f\}$. Hence the physical properties of a REV depend on the volume fractions of the constituents inside this

REV. All volume elements within the domain contain the same constituents, but in varying volumetric fractions. Consequently, on the macroscopic scale, we are unable to resolve the behavior of single grains. We do, however, know the percentage composition of each constituent within a REV, and how the constituents behave on average. In this framework, the sediment front and bed front are not sharp, discrete boundaries, but are represented by the location of the maximum porosity gradients within the domain. This approach of resolving phase boundaries has been used since the early days of Computational Fluid Mechanics to resolve fluid surfaces in free surface flows, and has been termed Volume of Fluid method (VOF), the classic work being [36].

The density, often called the *effective* or *true density* [78] of a material is defined as

$$\rho^{\alpha R} := \frac{dm^\alpha}{dv^\alpha}, \quad (3.1)$$

where dm^α is a mass element and dv^α is the volume occupied by this element. The *partial density* of a constituent is the mass of that constituent per volume of the mixture,

$$\rho^\alpha := \frac{dm^\alpha}{dv}. \quad (3.2)$$

The volume fraction of a constituent is introduced as

$$n^\alpha := \frac{dv^\alpha}{dv}. \quad (3.3)$$

We assume that there are no voids in the mixture, that is, $\sum_\alpha dv^\alpha = dv$, so that the sum of the volume fractions must equal unity,

$$\sum_\alpha n^\alpha = 1. \quad (3.4)$$

The benefit of this concept is that when one of the volume fractions is known, the second one is known automatically in case of biphasic mixtures. On the other hand, it implies the loss of one free variable, usually leading to complications in calculating the pressure.

3.3 Kinematical assumptions

Kinematics investigates the motion of material points within a continuum without considering the applied forces. This section introduces the most important kinematical concepts associated with the framework of Mixture Theory. The idea of mixture theory is that any *spatial* point is simultaneously occupied by *material* points of all mixture constituents at once. Each *material* point \mathcal{P}^α starting at some reference position at time t_0 follows its very own motion function (cf. Figure 3.2). By identifying each material point with its position in the reference (starting) configuration, we obtain its position \mathbf{x} at time $t > t_0$ as a function χ_α of the reference position \mathbf{X}_α and time t :

$$\mathbf{x} = \chi_\alpha(\mathbf{X}_\alpha, t). \quad (3.5)$$

At time t_0 , by definition, the material point occupies the position \mathbf{X}_α ,

$$\mathbf{X}_\alpha = \chi_\alpha(\mathbf{X}_\alpha, t_0). \quad (3.6)$$

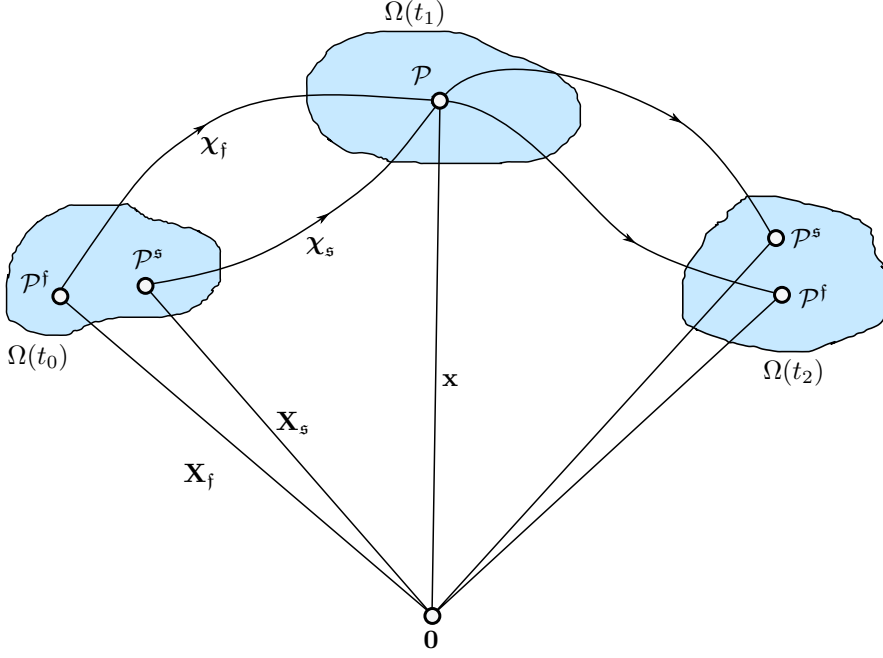


Figure 3.2: Illustration of Kinematics of superimposed continua, modified after [78]. Material points \mathcal{P}^f , \mathcal{P}^s , identified by their positions \mathbf{X}_f , \mathbf{X}_s in the reference configuration (left), are mapped by their motion functions χ_f , χ_s into current configurations, where they may occupy the same (middle) or different (right) spatial points.

As any two material points \mathcal{P}^f and \mathcal{P}^s follow their own motion functions χ_f and χ_s , they may start in different spatial positions \mathbf{X}_f and \mathbf{X}_s at time t_0 , then occupy the same spatial point \mathbf{x} at a later time t_1 and again occupy two different spatial points at time t_2 (Figure 3.2).

Velocity and acceleration of the motion (3.5) are given as the differentiation with respect to time

$$\begin{aligned} \mathbf{v}_\alpha(\mathbf{X}_\alpha, t) &= \frac{d}{dt} (\chi_\alpha(\mathbf{X}_\alpha, t)), \\ \mathbf{a}_\alpha(\mathbf{X}_\alpha, t) &= \frac{d^2}{dt^2} (\chi_\alpha(\mathbf{X}_\alpha, t)). \end{aligned} \quad (3.7)$$

It is clear that velocity and acceleration depend on the reference position \mathbf{X}_α of a constituent and on time. This corresponds to the situation of an observer following a material point \mathcal{P}^α along its path χ_α through space and time and is commonly referred to as the *Lagrangian* description. A different description can be given by an observer fixed in space, watching material points passing by (*Eulerian* specification). Such a specification can be achieved by inverting (3.5), yielding a function that depends on the current position \mathbf{x} and time t ,

$$\mathbf{X}_\alpha = \chi_\alpha^{-1}(\mathbf{x}, t). \quad (3.8)$$

Physically, this inversion implies that only one material point \mathcal{P}^α of a constituent φ^α can occupy a specific spatial position \mathbf{x} at a specific time t , and that this material

point started from exactly one reference position. The velocity and acceleration can then be written as

$$\begin{aligned}\mathbf{v}_\alpha(\mathbf{x}, t) &= \mathbf{v}_\alpha(\chi_\alpha^{-1}(\mathbf{x}, t), t), \\ \mathbf{a}_\alpha(\mathbf{x}, t) &= \mathbf{a}_\alpha(\chi_\alpha^{-1}(\mathbf{x}, t), t).\end{aligned}\tag{3.9}$$

The *mixture velocity*, called the *barycentric velocity*, is defined as

$$\mathbf{v} = \frac{1}{\rho} \sum_\alpha \rho^\alpha \mathbf{v}_\alpha.\tag{3.10}$$

The *deformation gradient* corresponding to constituent α is defined as the gradient of (3.5) with respect to the reference configuration \mathbf{X}_α

$$\mathbf{F}_\alpha = \text{Grad}_\alpha \mathbf{x} = \frac{d}{d\mathbf{X}_\alpha} (\chi_\alpha(\mathbf{X}_\alpha, t)).\tag{3.11}$$

It constitutes a linear mapping of line elements $d\mathbf{X}_\alpha$ in the reference configuration into line elements $d\mathbf{x}$ in the current configuration,

$$d\mathbf{x} = \mathbf{F}_\alpha \cdot d\mathbf{X}_\alpha.\tag{3.12}$$

The *velocity gradient* \mathbf{L}_α is defined as

$$\mathbf{L}_\alpha = \text{grad } \mathbf{v}_\alpha(\mathbf{x}, t).\tag{3.13}$$

Since by the chain rule we have

$$\text{Grad}_\alpha \mathbf{v}_\alpha(\mathbf{X}_\alpha, t) = \text{Grad}_\alpha \mathbf{v}_\alpha(\mathbf{x}, t) = \text{grad } \mathbf{v}_\alpha(\mathbf{x}, t) \text{Grad}_\alpha \mathbf{x} = \mathbf{L}_\alpha \mathbf{F}_\alpha,\tag{3.14}$$

and, on the other hand,

$$\begin{aligned}\text{Grad}_\alpha \mathbf{v}_\alpha(\mathbf{X}_\alpha, t) &= \text{Grad}_\alpha \frac{d}{dt} (\chi_\alpha(\mathbf{X}_\alpha, t)) \\ &= \frac{d}{dt} (\text{Grad}_\alpha \chi_\alpha(\mathbf{X}_\alpha, t)) = \frac{d}{dt} \mathbf{F}_\alpha := \dot{\mathbf{F}}_\alpha,\end{aligned}\tag{3.15}$$

we obtain

$$\mathbf{L}_\alpha \mathbf{F}_\alpha = \dot{\mathbf{F}}_\alpha,\tag{3.16}$$

and therefore

$$\mathbf{L}_\alpha = \dot{\mathbf{F}}_\alpha \mathbf{F}_\alpha^{-1}.\tag{3.17}$$

Like any tensor, \mathbf{L}_α can be decomposed into a symmetric part \mathbf{D}_α and a skew-symmetric part \mathbf{W}_α ,

$$\mathbf{L}_\alpha = \mathbf{D}_\alpha + \mathbf{W}_\alpha = \frac{1}{2} (\mathbf{L}_\alpha + \mathbf{L}_\alpha^T) + \frac{1}{2} (\mathbf{L}_\alpha - \mathbf{L}_\alpha^T).\tag{3.18}$$

\mathbf{D}_α is referred to as deformation or strain rate tensor, where the superposed T denotes the transposition and \mathbf{W}_α is the spin tensor. In the following, we will only use \mathbf{D}_α .

3.4 Balance equations

It is known from experience that within a closed system, certain measurable physical quantities can neither be created nor destroyed, they can only be redistributed in space - that is, these physical quantities are *conserved*. Examples are mass, momentum and energy, among others. This conservation property of a physical quantity is mathematically stated as a *conservation law*.

For open systems, i.e. systems where some quantity (conserved or not) can enter or leave via a system boundary, one can devise a *balance equation*, stating how much of the quantity enters the domain within a fixed amount of time, how much leaves the domain, how much is created or consumed within the domain and, consequently, by how much the amount of the quantity inside the domain increases or decreases. Such balance equations are useful for the mathematical description of physical systems; and if the equations can be solved either analytically or numerically, they can be used for the prediction of the behavior of a system subjected to a set of specified boundary conditions.

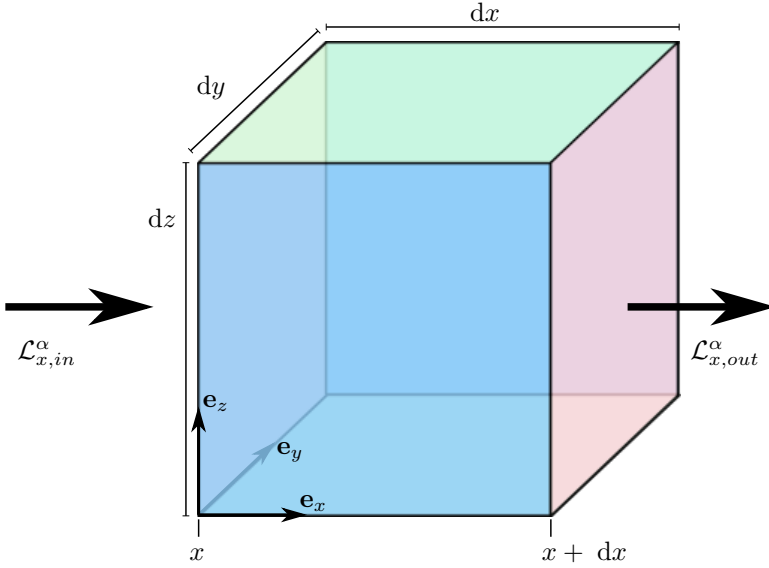


Figure 3.3: A control volume with crossflow.

In this section, the balance equations of the hybrid mixture model are derived. First, before resorting to the actual model equations, it is shown how a general balance equation for a mixture constituent can be derived based on physical intuition. For mathematically and thermodynamically rigorous derivations of the general equations, the reader is referred to e.g. [22, 23, 40, 44].

A general derivation of the balance equations used hereinafter in the framework of Mixture Theory is as follows: Imagine a control volume $dv = dx dy dz$ (see Figure 3.3) with a mixture of, for example, N components entering at the coordinate x and leaving at $x + dx$. The mixture as a whole is a superposition of its N constituents. Let \mathcal{L}^α be a conserved quantity of constituent α and $\hat{\mathcal{L}}^\alpha = \frac{\mathcal{L}^\alpha}{dv^\alpha}$ the *specific* amount of the physical quantity per unit volume. Further, let us denote by \mathcal{Q}^α the *supply*, that is, any *external* sources or sinks for the quantity \mathcal{L}^α ; and, in analogy with $\hat{\mathcal{L}}^\alpha$,

$\tilde{Q}^\alpha = \frac{\mathcal{Q}^\alpha}{dv^\alpha}$. For instance, if the conserved quantity was heat, a good example of a source would be a flame underneath the control volume, heating the mixture inside. Moreover, we also have to account for *internal* sources and sinks for \mathcal{L}^α originating from within the mixture: One constituent may receive a portion of the quantity \mathcal{L}^α from another one, either due to direct exchange or indirectly due to mass exchange. To understand this, imagine a) that \mathcal{L}^α denotes momentum; b) that the mixture consists of ice and water. The two constituents may exchange momentum directly within the control volume. Now imagine that c) some of the ice melts within the control volume: The momentum that was formerly attributed to the (now molten) ice must be attributed to water. These two contributions are lumped in an *exchange term*, also called *production*, denoted by \mathcal{S}^α and $\tilde{\mathcal{S}}^\alpha = \frac{\mathcal{S}^\alpha}{dv^\alpha}$. Note that, because \mathcal{L}^α is a conserved quantity, $\sum_\alpha \mathcal{S}^\alpha = 0$. Considering only flow in x -direction and assuming zero flow in y - and z -directions, the balance equation for the quantity \mathcal{L}^α reads in the most general form:

$$\frac{\partial \mathcal{L}^\alpha}{\partial t} = \frac{\partial \mathcal{L}_{x,in}^\alpha}{\partial t} - \frac{\partial \mathcal{L}_{x,out}^\alpha}{\partial t} + \mathcal{Q}^\alpha + \mathcal{S}^\alpha. \quad (3.19)$$

That is, simply speaking, the rate of change of quantity \mathcal{L}^α per unit volume is the difference between in- and outflow plus what is created / consumed within the volume plus what is exchanged between the constituents within the volume. Next, assume that the control volume has a unit cross section da perpendicular to the x -direction, and unit volume $dv = da \, dx$. The constituent α flows into the control volume at velocity $u_{\alpha,x} = \left. \frac{dv^\alpha}{\partial t \, da} \right|_{\alpha,x}$ and leaves at velocity $u_{\alpha,x+dx} = \left. \frac{dv^\alpha}{\partial t \, da} \right|_{\alpha,x+dx}$. We obtain from (3.19):

$$\begin{aligned} \frac{\partial \mathcal{L}^\alpha}{\partial t} &= \tilde{\mathcal{L}}_x^\alpha u_{\alpha,x} \, da - \tilde{\mathcal{L}}_{x+dx}^\alpha u_{\alpha,x+dx} \, da + \mathcal{Q}^\alpha + \mathcal{S}^\alpha \\ &= \tilde{\mathcal{L}}_x^\alpha u_{\alpha,x} \, da - \left(\tilde{\mathcal{L}}_x^\alpha u_{\alpha,x} \, da + \frac{\partial}{\partial x} \left(\tilde{\mathcal{L}}_x^\alpha u_{\alpha,x} \right) dx \, da \right) + \mathcal{Q}^\alpha + \mathcal{S}^\alpha \\ &= -\frac{\partial}{\partial x} \left(\tilde{\mathcal{L}}_x^\alpha u_{\alpha,x} \right) dv + \mathcal{Q}^\alpha + \mathcal{S}^\alpha, \end{aligned} \quad (3.20)$$

and, dividing by dv ,

$$\frac{\partial \tilde{\mathcal{L}}^\alpha}{\partial t} = -\frac{\partial}{\partial x} \left(\tilde{\mathcal{L}}_x^\alpha u_{\alpha,x} \right) + \tilde{\mathcal{Q}}^\alpha + \tilde{\mathcal{S}}^\alpha. \quad (3.21)$$

If we now consider also flow in the y - and z -directions, the spatial derivative turns into a divergence, and we arrive at

$$\frac{\partial \tilde{\mathcal{L}}^\alpha}{\partial t} + \operatorname{div} \left(\tilde{\mathcal{L}}^\alpha \mathbf{v}_\alpha \right) = \tilde{\mathcal{Q}}^\alpha + \tilde{\mathcal{S}}^\alpha, \quad (3.22)$$

with the velocity vector $\mathbf{v}_\alpha = [u_\alpha \, v_\alpha \, w_\alpha]^T$. Introducing the concept of mass fractions from (3.3), we obtain

$$\frac{\partial}{\partial t} \left(n^\alpha \tilde{\mathcal{L}}^{\alpha R} \right) + \operatorname{div} \left(n^\alpha \tilde{\mathcal{L}}^{\alpha R} \mathbf{v}_\alpha \right) = \tilde{\mathcal{Q}}^\alpha + \tilde{\mathcal{S}}^\alpha. \quad (3.23)$$

Equation (3.23) represents the general balance equation for constituent α . We assume here isothermal conditions during the flow process, so that a mass and a momentum balance are sufficient to describe the system.

3.4.1 Balance of mass

After this general derivation, let us now come to the balance equations used for the sedimentation model. To obtain the mass balance, we have to replace the arbitrary conserved quantity \mathcal{L}^α by mass m^α and its specific counterpart $\tilde{\mathcal{L}}^{\alpha R}$ in (3.23) by the true density $\rho^{\alpha R}$. Clearly, during sedimentation, there is no phase change between the two constituents (water and solid grains), and mass is not produced or destroyed inside the system, therefore the exchange term $\tilde{\mathcal{S}}^\alpha$ and the source term $\tilde{\mathcal{Q}}^\alpha$ are zero. Hence, the mass balance reads:

$$\frac{\partial}{\partial t} (n^\alpha \rho^{\alpha R}) + \operatorname{div} (n^\alpha \rho^{\alpha R} \mathbf{v}_\alpha) = 0. \quad (3.24)$$

As noted earlier, it is usually assumed in flow models for solid-liquid mixtures that both phases are incompressible, that is, ρ^{sR} and ρ^{fR} are constant. Here, however, we assume that the solid grains are incompressible and the fluid is *weakly* compressible, meaning that density variations are assumed to be small but non-zero:

$$\rho^{sR} = \rho_0^{sR} = \text{const}, \quad (3.25)$$

$$\rho^{fR} \neq \text{const}. \quad (3.26)$$

The solid is assumed incompressible, so that the mass balance can be divided by the true density, transforming the solid's mass balance into a volume balance, while the mass balance for the fluid remains unchanged:

$$\frac{\partial n^s}{\partial t} + \operatorname{div} (n^s \mathbf{v}_s) = 0 \quad (3.27)$$

$$\frac{\partial}{\partial t} (n^f \rho^{fR}) + \operatorname{div} (n^f \rho^{fR} \mathbf{v}_f) = 0. \quad (3.28)$$

3.4.2 Balance of momentum

To obtain the momentum balance, we replace \mathcal{L}^α by momentum $m^\alpha \mathbf{v}_\alpha$ and $\tilde{\mathcal{L}}^{\alpha R} \mathbf{v}_\alpha$ in (3.23) by $\rho^{\alpha R} \mathbf{v}_\alpha$. The source term $\tilde{\mathcal{Q}}^\alpha$ in (3.23) is denoted by \mathbf{q}^α and the exchange term $\tilde{\mathcal{S}}^\alpha$ by $\hat{\mathbf{s}}^\alpha$,

$$\frac{\partial}{\partial t} (n^\alpha \rho^{\alpha R} \mathbf{v}_\alpha) + \operatorname{div} (n^\alpha \rho^{\alpha R} \mathbf{v}_\alpha \otimes \mathbf{v}_\alpha) = \mathbf{q}^\alpha + \hat{\mathbf{s}}^\alpha. \quad (3.29)$$

The *total momentum production* $\hat{\mathbf{s}}^\alpha$ is decomposed into the *direct momentum production* $\hat{\mathbf{p}}^\alpha$ and a term $\hat{\boldsymbol{\ell}}^\alpha$ that is due to mass exchange between the constituents,

$$\hat{\mathbf{s}}^\alpha = \hat{\mathbf{p}}^\alpha + \hat{\boldsymbol{\ell}}^\alpha, \quad (3.30)$$

with

$$\hat{\boldsymbol{\ell}}^\alpha = \hat{n}^\alpha \rho^{\alpha R} \mathbf{v}_\alpha. \quad (3.31)$$

and \hat{n}^α the volume production of constituent α , which in this case is zero (no mass exchange between the constituents, see Section 3.4.1). In the sedimentation case, drag between the fluid phase and settling grains is an example of direct momentum production. The mixture as a whole is assumed to behave like a single continuum body, so that the total momentum production of the mixture must vanish:

$$\sum_\alpha \hat{\mathbf{s}}^\alpha = \mathbf{0}. \quad (3.32)$$

As noted earlier, in the sedimentation problem there is no mass exchange between solid grains and fluid, and hence

$$\begin{aligned}\hat{\ell}^\alpha &= 0, \\ \hat{\mathbf{s}}^\alpha &= \hat{\mathbf{p}}^\alpha.\end{aligned}\tag{3.33}$$

A statement of the classical dynamics of Newton and Euler is that a change in the motion, and hence momentum, of a continuous body is produced by external forces. One may differentiate between forces \mathbf{f}_c^α that are applied via direct contact on the surface of a body, and volume or body forces \mathbf{f}_b^α originating from sources like gravity. The source term \mathbf{q}^α sums up to

$$\mathbf{q}^\alpha = \mathbf{f}_c^\alpha + \mathbf{f}_b^\alpha.\tag{3.34}$$

The surface forces are expressed by integrating all stress vectors \mathbf{t}^α on the surface $\partial\Omega^\alpha$ of the control volume,

$$\mathbf{f}_c^\alpha = \int_{\partial\Omega} \mathbf{t}^\alpha \, da.\tag{3.35}$$

Exploiting Gauss' theorem $\int_\Omega \operatorname{div}(\bullet) \, dv = \int_{\partial\Omega} (\bullet) \mathbf{n} \, da$ and Cauchy's theorem $\mathbf{t} =: \mathbf{T} \cdot \mathbf{n}$, with the Cauchy stress tensor \mathbf{T} and the normal vector \mathbf{n} on the surface da , the above integral can be rewritten as a volume integral:

$$\mathbf{f}_c^\alpha = \int_\Omega \operatorname{div} \mathbf{T}^\alpha \, dv.\tag{3.36}$$

The total body force (in the sedimentation problem: gravity) applied to a constituent α is expressed as

$$\mathbf{f}_b^\alpha = \int_\Omega \mathbf{b} \, dm^\alpha = \int_\Omega \rho^\alpha \mathbf{b} \, dv.\tag{3.37}$$

Equations (3.36) and (3.37) must hold for arbitrary volumes, thus we can drop the volume integrals:

$$\mathbf{f}_c^\alpha = \operatorname{div} \mathbf{T}^\alpha, \quad \mathbf{f}_b^\alpha = \rho^\alpha \mathbf{b}.\tag{3.38}$$

Plugging (3.38), (3.30) and (3.34) into (3.29), we arrive at the following general form of the momentum balance of constituent α in conservative form:

$$\frac{\partial}{\partial t} (n^\alpha \rho^{\alpha R} \mathbf{v}_\alpha) + \operatorname{div} (n^\alpha \rho^{\alpha R} \mathbf{v}_\alpha \otimes \mathbf{v}_\alpha - \mathbf{T}^\alpha) = \rho^\alpha \mathbf{b} + \hat{\mathbf{s}}^\alpha.\tag{3.39}$$

In the sedimentation case, the relations for solid and fluid are

$$\frac{\partial}{\partial t} (n^s \rho^{sR} \mathbf{v}_s) + \operatorname{div} (n^s \rho^{sR} \mathbf{v}_s \otimes \mathbf{v}_s - \mathbf{T}^s) = \rho^s \mathbf{b} + \hat{\mathbf{s}}^s,\tag{3.40}$$

$$\frac{\partial}{\partial t} (n^f \rho^{fR} \mathbf{v}_f) + \operatorname{div} (n^f \rho^{fR} \mathbf{v}_f \otimes \mathbf{v}_f - \mathbf{T}^f) = \rho^f \mathbf{b} - \hat{\mathbf{s}}^s.\tag{3.41}$$

3.5 Constitutive relations for batch sedimentation

To this point, the general balance equations for a mixture of an incompressible granular solid and a weakly compressible fluid, equations (3.27), (3.28), (3.40) and (3.41)

were derived. For the two constituents (water and sediment, $\alpha = \{\mathbf{f}, \mathbf{s}\}$), the system consists of four vectorial equations. The unknowns are $n^{\mathbf{s}}, n^{\mathbf{f}}, \rho^{\mathbf{f}R}, \mathbf{v}_{\mathbf{s}}, \mathbf{v}_{\mathbf{f}}, \mathbf{T}^{\mathbf{s}}, \mathbf{T}^{\mathbf{f}}$ and $\hat{\mathbf{s}}^{\mathbf{s}}$. Note that $\rho^{\mathbf{s}R} = \text{const}$, cf. equation (3.25). Further, note that due to the saturation condition, equation (3.4), $n^{\mathbf{s}}$ and $n^{\mathbf{f}}$ are not independent variables and the number of unknowns reduces by one. To close the system of equations, constitutive relations must be found for the stress tensors $\mathbf{T}^{\mathbf{s}}$ and $\mathbf{T}^{\mathbf{f}}$, and for the momentum exchange terms $\hat{\mathbf{s}}^{\mathbf{s}} = -\hat{\mathbf{s}}^{\mathbf{f}}$. Regarding the latter two terms, note that due to (3.33), we are seeking constitutive equations for the *direct* momentum production only. These constitutive equations are now derived for the case of batch sedimentation; thus we change now from the general equations to a specific application that can be used as a benchmark for validation of the model.

Let us start with the partial Cauchy stress tensors. Here, both constituents (fluid and aggregates of solid grains) are modeled as linear viscous fluids. That is, the stress tensor \mathbf{T}^{α} is decomposed into the sum of hydrostatic and extra stresses,

$$\mathbf{T}^{\alpha} = -p^{\alpha} \mathbf{I} + \mathbf{T}_E^{\alpha}, \quad (3.42)$$

where p^{α} denotes the partial pressure and \mathbf{T}_E^{α} is the viscous or extra stress tensor of the constituent α . The partial pressure corresponds to the stress within the constituent at rest. Constitutive assumptions must be postulated for both p^{α} and \mathbf{T}_E^{α} . Although this treatment is straight-forward in case of the fluid phase because it shows a strain rate dependent (i.e. viscous) behavior, a different treatment is possible for the solid phase and has been applied in debris flow models; see e.g. [68, Appendix B] and citations therein.

The extra stresses for a compressible fluid are commonly assumed as (cf. [74]):

$$\mathbf{T}_E^{\alpha} = 2\mu^{\alpha} \left(\mathbf{D}_{\alpha} - \frac{1}{3} \text{div } \mathbf{v}_{\alpha} \mathbf{I} \right), \quad (3.43)$$

with

$$\mathbf{D}_{\alpha} = \frac{1}{2} \left(\text{grad } \mathbf{v}_{\alpha} + \text{grad}^T \mathbf{v}_{\alpha} \right) \quad (3.44)$$

and the scalar coefficient μ^{α} is the dynamic viscosity. Here, we adopt the assumption (3.43) for both phases. If the dynamic viscosity, μ^{α} , is constant, the extra stresses depend linearly on the shear rate, and the fluid follows a Newtonian rheology. In our case, this rheology is realistic for the fluid phase, and we prescribe

$$\mu^{\mathbf{f}} = 10^{-3} \text{ Pa s}. \quad (3.45)$$

For the solid, however, the situation is different. Ishii & Zuber [42] describe how the apparent viscosity of a mixture changes due to the presence of a dispersed solid: A single particle P moving through the fluid will impart a motion on the fluid. The motion of the fluid yet again imparts forces on particles in the neighborhood. As the particles are rigid, they do not deform as the fluid does. For the original particle P this results in an apparent increase of the viscosity of the fluid around it. When the solid volume fraction further increases, the particles may interact directly, creating friction between the particles and further increasing the mixture viscosity. It is clear, however, that it is impossible to give a relation for the viscosity of the grains directly, because it cannot be measured; but one can give a relation for the viscosity of the mixture, and, if the fluid viscosity is known, calculate the solid viscosity from the

mixture and fluid viscosity by assuming that the mixture viscosity is the arithmetic mean of the constituent viscosities,

$$\mu^{mixture} = n^s \mu^s + n^f \mu^f. \quad (3.46)$$

A multitude of viscosity equations for fluid-granular mixtures exist; examples are [12, 26, 29, 71] to name just a few. Most viscosity corrections have in common that they give an exponential dependence of mixture viscosity on the solid volume fraction; cf. [42, figure 3] for a comparison. We choose the relation proposed by Ishii & Zuber [42],

$$\mu^{mixture} = \mu^f \left(1 - \frac{n^s}{n_{max,\mu}^s} \right)^{-2.5n_{max,\mu}^s}, \quad (3.47)$$

which shows the desired properties while being relatively simple. The formulation in (3.47) implies that $\mu^{mixture} \rightarrow \infty$ as a close packing of grains is approached, $n^s \rightarrow n_{max}^s$. This leads to undesired model behavior in the close packing limit, because the mixture would turn almost rigid before the densest packing is reached, and a sedimentation process would become unrealistically slow in the vicinity of the bed front. Hence, in (3.47) $n_{max,\mu}^s$ is viewed as a *model* parameter (as opposed to a *physical* parameter describing a specific property of the physical problem) that must be greater than n_{max}^s and can be adjusted to fit experimental results. The reaction of the model to a variation in $n_{max,\mu}^s$ is investigated in Chapter 5. The solid viscosity can now be calculated from (3.46) and (3.47):

$$\mu^s = \frac{\mu^f}{n^s} \left[\left(1 - \frac{n^s}{n_{max,\mu}^s} \right)^{-2.5n_{max,\mu}^s} - n^f \right]. \quad (3.48)$$

At this point, the extra stresses \mathbf{T}_E^α of (3.42) are specified, and we are left with the definition of the pressure part p^α of the partial stress tensor \mathbf{T}^α . In analogy with kinetic gas theory, the total pressure of a mixture is the sum of the partial pressures of the constituents (cf. Dalton's law of partial pressures in a mixture of non-reacting gases), so that the partial pressure of the fluid *phase* is given by

$$p^f = n^f p^{fR}, \quad (3.49)$$

where p^{fR} denotes the *true* fluid pressure, i.e. the fluid pressure in presence of only one single phase. Here, we assume a barotropic fluid, whose true pressure depends on its density only. For water, the relation between pressure and density is generally nonlinear, and can be approximated by the Tait equation [6, 17, 56, 63].

$$p^{fR} = \frac{K_0^f}{\gamma} \left(\left(\frac{\rho^{fR}}{\rho_{ref}^{fR}} \right)^\gamma - 1 \right) + p_0^{fR}. \quad (3.50)$$

Here, K_0^f is the fluid bulk modulus, $\rho_{ref}^{fR} = 1000 \text{ kg/m}^3$ is a reference density, γ is an empirical parameter that is usually set to a value of

$$\gamma \approx 7, \quad (3.51)$$

see [6, 17, 63], and p_0^{fR} is a reference pressure, for example atmospheric pressure. In the model equations, the pressure occurs only in gradient expressions, so that we set

$$p_0^{fR} = 0. \quad (3.52)$$

The Tait equation is in agreement with experimental measurements for water within a few per cent accuracy over a range of pressures of several hundred Megapascal, cf. [6, p. 56], [17, p. 38f.]. If the density variation in a given physical problem is small, (3.50) can be approximated by a linear relation:

$$p^{fR} = c_f^2 \left(\rho^{fR} - \rho_{ref}^{fR} \right) + p_0^{fR}, \quad (3.53)$$

where c_f is the speed of sound in the fluid, which is connected to the fluid bulk modulus via the Newton-Laplace equation, $c_f^2 = K^f / \rho^{fR}$, and is assumed constant here. In a real batch sedimentation process, the density variations will be less than one per mille for water column heights of up to 100 m. In this regime, it is certainly sufficient to use equation (3.53) instead of (3.50), cf. Figure 3.4. In Section 4.2.3, the two pressure laws are compared using a classical, single-fluid CFD example.

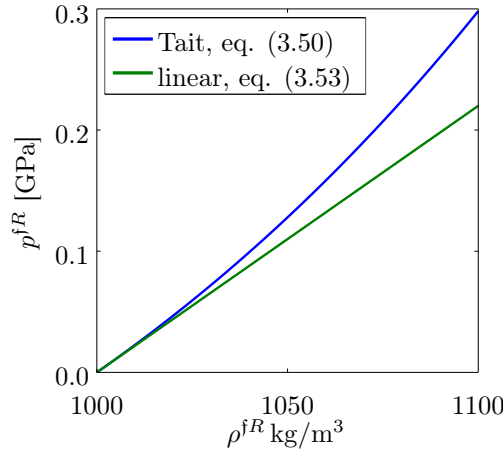


Figure 3.4: Comparison of the pressure laws (3.50) and (3.53), assuming $K_0^f = 2.2$ GPa, $\gamma = 7$, $\rho^{fR} = 1000$ kg/m³, $p_0^{fR} = 0$ and $c^f = 1483$ m/s.

The definition of the fluid pressure is a key relation in the model. On the one hand, it allows to realistically depict the propagation of acoustic waves in the medium, and the reaction of the fluid pressure to volumetric deformation of the fluid – and hence, the ability to describe flow processes where this is of major importance, cf. Chapter 2. On the other hand, the high acoustic wave velocity leads to the necessity to choose small timesteps in order to resolve the rapid wave propagation; especially in explicit time stepping schemes this requirement can be unfavorable or even devastating. In flow situations when both wave propagation and reaction of pressure to volumetric deformation of the fluid are not important, c_f can be treated as a *model* parameter rather than a *physical* parameter, and greater time step sizes can be achieved by setting the speed of sound (and hence, the fluid compressibility) to unphysically low values. In that case, it must be assured that density variations are less than $\approx 10\%$, which can be achieved by setting $c_f \approx 10V$, where V is the maximum velocity of the fluid throughout the entire simulation and must be estimated a priori or found by numerical experiments, see [63].

Relation (3.49) attributes only a part of the true fluid pressure to the fluid phase. The solid particles are incompressible, so that their true pressure p^{sR} does not depend

on their true density ρ^{sR} . Instead, the fluid imparts forces on the surfaces of the incompressible solid particles, so that we can assume that the true pressure within each of the solid particles is solely determined by the true fluid pressure surrounding the particle, and

$$p^{sR} = p^{fR}. \quad (3.54)$$

Hence the difference between the fluid pressure p^f and the true fluid pressure p^{fR} , given by $n^s p^{fR}$, will enter the expression for the granular solid pressure.

With respect to the solid, yet another contribution to the pressure must be accounted for. The highest physically possible volume fraction for solid particles is the densest packing, so that some mechanism must assure that $n^s < n_{max}^s$. This is achieved via a so-called configuration [40] or particle pressure [45, 65] p_{conf}^s . The partial solid pressure, in analogy to the partial fluid pressure, is hence given by

$$p^s = n^s p^{fR} + p_{conf}^s. \quad (3.55)$$

The idea behind the configuration pressure term is an analogy observation between gases and granular media, called kinetic theory of granular flow [18, 33, 59]. The constitutive equation for p_{conf}^s is similar to the equation of state for ideal gases, but additionally accounts for collisions and maximum volume fraction:

$$p_{conf}^s = \Theta^s \rho^{sR} 2(1 + e^s) (n^s)^2 g_0^s, \quad (3.56)$$

see [79]. Here, Θ^s is the granular temperature, which is analogous to the temperature in kinetic gas theory and accounts for random fluctuations in solid grain velocity; $e^s = 0.9$ is the coefficient of restitution for solid glass spheres, and $g_0^s(n^s)$ is the radial distribution function, for which we choose the relation

$$g_0^s = \left(\frac{1}{1 - \frac{n^s}{n_{max}^s}} \right)^{1/3}, \quad (3.57)$$

see [64]. Hence, the configurational pressure is calculated from an exponential function of solid volume fraction. At low volume fractions, the particles can move freely within the fluid, and the configurational pressure gradient of the dispersed phase disappears. However, when $n^s \rightarrow n_{max}^s$, the pressure gradient increases, resulting in a repulsive force between the particles; and hence, the maximum solid volume fraction cannot be exceeded. If we express the number of neighbours within a certain distance of a given particle in terms of a coordination number \bar{K} , then (3.57) implies that $\bar{K} \rightarrow 0$ for $n^s \rightarrow 0$. When the solid volume fraction increases, the particles slowly start to interact, until $\bar{K} \rightarrow \bar{K}_{max}$ for $n^s \rightarrow n_{max}^s$ and no further compression is possible. The random fluctuations, described by Θ^s , of non-colloidal spheres in case of batch sedimentation are assumed to be constant and small. From a modeling point of view, the configuration pressure is responsible for keeping the solid volume fraction below the maximum value. At the same time, the sharp interface between settled bed and sedimenting grains should be depicted, which requires that the grains slow down from their equilibrium settling velocity to zero within a very short distance. In terms of the solid configuration pressure, this behavior can be attained by keeping Θ^s as low as possible. In this case, p_{conf}^s reacts very slowly to increasing values of n^s as long as the solid volume fraction is low, and very strongly when the solid volume fraction is high. However, when the value of Θ^s is too low, the configuration pressure increases too fast near the interface, so that a good compromise must be found. The sedimentation model is tested for a range of values of Θ^s in Chapter 5.

Up to this point, the stress tensors of both solid and fluid are fully specified, and only the constitutive assumption on the momentum exchange term is left to be defined. It can be decomposed into an equilibrium, $\hat{\mathbf{s}}_{eq}^\alpha$, and a non-equilibrium contribution $\hat{\mathbf{s}}_{neq}^\alpha$, see [41, 78]:

$$\hat{\mathbf{s}}^\alpha = \hat{\mathbf{s}}_{eq}^\alpha + \hat{\mathbf{s}}_{neq}^\alpha. \quad (3.58)$$

Let us investigate the equilibrium part. To do this, we first analyze the contribution of the pressure to the divergence of the stress tensor in equation (3.39). Recall from (3.42) that the stress tensor is decomposed into a pressure and an extra stress contribution. Noting that $p^\alpha = n^\alpha p^{\alpha R}$ and taking the divergence of the pressure contribution only, we can write

$$\operatorname{div}(-n^\alpha p^{\alpha R} \mathbf{I}) = -n^\alpha \operatorname{grad} p^{\alpha R} - p^{\alpha R} \operatorname{grad} n^\alpha. \quad (3.59)$$

Now assume an "equilibrium" situation where velocities, pressure gradients and body forces are zero. The momentum balance (3.39) becomes:

$$p^{\alpha R} \operatorname{grad} n^\alpha = \hat{\mathbf{s}}_{eq}^\alpha \quad (3.60)$$

i.e., even in a situation where the whole system is at rest, the contribution from the equilibrium part of the exchange term is non-zero. The term on the left side was called the *buoyancy force* by Drew [22]. Exploiting (3.54) for the present biphasic model, (3.60) corresponds to

$$\hat{\mathbf{s}}_{eq}^f = -p^{fR} \operatorname{grad} n^s, \quad (3.61)$$

$$\hat{\mathbf{s}}_{eq}^s = p^{fR} \operatorname{grad} n^s, \quad (3.62)$$

respectively, for the fluid and the solid equilibrium momentum exchange term. In the most general case, the non-equilibrium term $\hat{\mathbf{s}}_{neq}^\alpha$ may consist of a multitude of contributions (see e.g. [44, 68]), among which the most important ones are lift and virtual mass forces, momentum exchange due to mass exchange and viscous drag. In our case, there is no mass exchange between solid and fluid, and lift and virtual mass forces are considered to be small and are therefore neglected. We are left with the viscous drag force, for which, according to Jackson [44], Ishii & Zuber [42] have proposed "perhaps the best known attempt [...], valid over the whole range of [particle] Reynolds numbers and particle concentrations". The relation can be derived from the drag force on a single sphere immersed in an infinite fluid:

$$\mathbf{F}_D(\mathbf{w}) = C_D(Re_d) \frac{1}{2} A \rho^f \mathbf{w} |\mathbf{w}|. \quad (3.63)$$

Here, $A = \pi (d/2)^2$ is the particle's cross section with d the diameter of the sphere; $\mathbf{w} = \mathbf{v}_f - \mathbf{v}_s$ is the difference between fluid velocity and particle velocity, and C_D is the drag coefficient that depends on the local grain Reynolds number Re_d ,

$$Re_d = \frac{|\mathbf{w}| d \rho^f}{\mu^f}. \quad (3.64)$$

In (3.63), the modulus of the term $1/2 A \rho^f \mathbf{w} |\mathbf{w}|$ corresponds to the kinetic energy of the fluid which is displaced by the particle. In general, the viscous drag is due to form drag and skin friction. For Reynolds numbers $Re < 1$ however, drag is only

due to skin friction, the drag coefficient is given by Stokes' law $C_D = 24/Re$, and \mathbf{F}_D reduces to Stokes' drag $\mathbf{F}_D = 3\mu^f \pi d \mathbf{w}$. For higher Reynolds numbers, many empirical expressions have been proposed to fit the experimentally observed dependence of C_D on Re . Ishii & Zuber [42] chose

$$C_D = \frac{24}{Re_d} (1 + 0.1 Re_d^{0.75}). \quad (3.65)$$

It is well-known since the famous experiments of Richardson & Zaki [70] that the settling velocity of a particle is reduced in the presence of other particles. Ishii & Zuber [42] propose to handle this effect by simply replacing the fluid viscosity in Re_d by an expression for the mixture viscosity:

$$Re_d = \frac{|\mathbf{w}| d \rho^{fR}}{\mu^m}. \quad (3.66)$$

Here, μ^m is given by equation (3.47). It is clear, as Jackson [44] notes, that this procedure cannot yield correct results if the value $n_{max,\mu}^s$ is set equal to the physically correct value n_{max}^s because in that case,

$$\lim_{n^s \rightarrow n_{max}^s} |\mathbf{F}_D| = \infty. \quad (3.67)$$

The above relation cannot be correct because even at close packing, an assembly of grains retains a finite permeability and hence, a finite drag force. Moreover, the sedimentation velocity would tend to zero in the vicinity of the bed front, which is not in agreement with experimental observations. Consequently, as noted earlier, $n_{max,\mu}^s$ is seen here as a *modeling* parameter that can be adjusted to fit e.g. experimental results. The specific momentum exchange term is finally calculated from the drag force as

$$\hat{\mathbf{s}}_{neq}^s = \frac{n^s \mathbf{F}_D}{V} \quad (3.68)$$

with $V = 1/6\pi d^3$ the volume of a particle.

3.6 Summary and discussion of the hybrid model

The main feature of the hybrid model is its ability to capture physical effects (e.g. acoustic wave propagation, cf. Chapter 5) associated with the compressibility of the fluid and the bulk flow behavior of the mixture within a single framework. The model allows for a relatively simple extension to a specific type of flow by adjusting the constitutive laws. For example, the flow described in Chapter 2 could be described by using constitutive relations commonly used in landslide and debris flow modeling, see e.g. [67, 68]. An extension to n solid phases with slightly different physical properties (e.g. different grain sizes) is also straightforward by adding mass and momentum balances for each additional solid phase. In incompressible models, the pressure does not appear as a free variable, but rather as a Lagrange multiplier, requiring more sophisticated implicit pressure projection methods for numerical solution. For the hybrid model, the pressure is defined constitutively, permitting the use of simple explicit time integration schemes. However, explicit integration leads to the necessity of choosing small time steps in the numerical integration. This issue is further discussed in Section 4.5.

Chapter 4

Numerical implementation - discontinuous Galerkin method

The equations derived in Chapter 3 are numerically implemented using a nodal discontinuous Galerkin (nodal dG) method, based on the ideas outlined in [35]. In this thesis, the aim is to understand and explain physical effects in flows of fluid-solid mixtures, and the numerical method is understood as a tool. Consequently, the theory, notations and illustrations in this chapter are and largely inspired by [35]. However, the chapter thoroughly introduces the dG method in 1-D using simple examples, so that it might serve a reader who is unfamiliar with numerical methods at large and with discontinuous Galerkin methods in particular as a good introduction to the method, and an aid in understanding the derivations and example codes presented in [35].

The structure of the chapter is as follows: First, the focus will be on the implementation of a simple advection problem in 1-D. Next, the treatment of second spatial derivatives in partial differential equations is covered, using advection-diffusion as an example. Then, the ideas and principles presented so far are transferred to a 2-D geometry. Two examples are shown implementing the weakly compressible Navier-Stokes equations. Two physical effects acting at very different timescales are described by these equations: mass transport is described on a long timescale; yet, the propagation of acoustic waves, which usually acts on very short timescales, is also captured. One problem emerging from the existence of acoustic waves in the model is the treatment of in- and outflow boundaries, where it is desirable to avoid reflections. Hence the treatment of open, non-reflecting in- and outflow boundaries is studied in the context of compressible Navier-Stokes equations. Next, the implementation of the mixture model equations presented in Chapter 3 is explained, before turning to the time marching scheme, which must assure that both the short and long timescales are properly captured.

4.1 Introduction to the discontinuous Galerkin method

4.1.1 Idea

The idea behind discontinuous Galerkin methods is to combine the advantages of the Finite-Volume (FVM) and the Finite-Element (FEM) methods. In short, this aim is achieved by using spaces of basis and test functions that mimic the FE method, but - and this is important - only at the element level. At this stage, the single elements are disconnected from each other. The global solution, i.e. the solution in the computational domain, is then recovered by connecting the elements via numerical fluxes over the element boundaries, similarly as in FV methods (cf. Figure 4.1). This way, FEM's advantages of high-order approximations, flexible geometries and relatively straight-forward p-adaptivity (i.e., variation of polynomial degree) is combined with FVM's advantages of h-adaptivity (i.e., variation of mesh cell size), and stability and robustness for conservation laws.

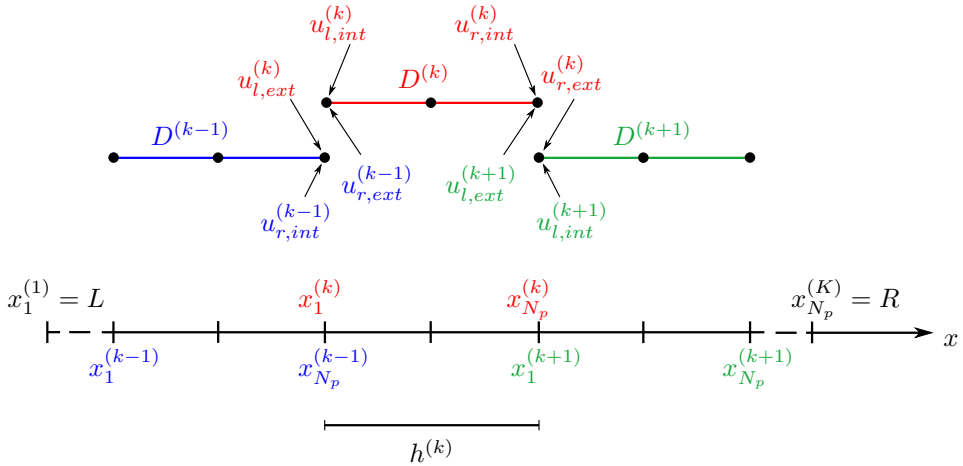


Figure 4.1: Illustration of element connectivity in 1-D. Example is for polynomial order $N = 2$, so that each element contains $N_p = 3$ vertices (black points in upper panel). The single elements $D^{(k)}$ are not connected, so that at faces which are not a domain boundary, two vertices share a single coordinate. The single elements are only connected via the numerical flux, which is a linear combination of the solution value u_{int} of one face of element k and the solution value u_{ext} of the adjacent face of element $k + 1$ or $k - 1$. The adjacent face shares the same physical coordinate but belongs to a neighboring element. The indices l, r relate to the left and right face of an element and in 1-D, have the same meaning as the indices 1, N_p . Hence, the numerical flux can be seen as a "boundary condition for an element".

4.1.2 The nodal basis

Before we can start with the actual derivations of the advection problem from its partial differential equation to numerical implementation, some preliminaries are needed. Namely, a solution u that is continuous in physical space somehow has to be represented by a discrete approximation u_h on the computer. In particular, a polynomial expansion, consisting of a polynomial basis and expansion coefficients is used for this

approximation. To understand the principles behind the dG method, it is sufficient to have a very basic understanding of how the basis is computed; however, some notation will be introduced in this section that is used in the remainder of the chapter. For all numerical computations shown in this thesis, the computation of the basis was achieved using algorithms from the open-source code Pydgon by Andreas Klöckner [49].

In many dG methods, a so-called *modal* expansion is used:

$$u(x, t) \simeq u_h^{(k)}(x, t) = \sum_{n=1}^{N_p} \hat{u}_n^{(k)}(t) \psi_n(x), \quad x \in D^{(k)}. \quad (4.1)$$

Here, $u_h^{(k)}(x, t)$ is the discrete approximation of $u(x, t)$ on the element $D^{(k)}$, ψ_n is a *basis* of the polynomial space, and $\hat{u}_n^{(k)}(t)$ are the expansion coefficients that we need to calculate to recover the solution. N_p is the number of expansion coefficients, which is related to the polynomial order N by $N_p = N + 1$ in 1-D. Note that the coefficients are functions of t only.

If in (4.1) the polynomial basis consists of the Lagrange polynomials

$$\ell_i^{(k)}(x) \equiv \prod_{\substack{j=1 \\ j \neq i}}^{N_p} \frac{x - x_j^{(k)}}{x_i^{(k)} - x_j^{(k)}} \quad (4.2)$$

for some points $x_1^{(k)}, \dots, x_{N_p}^{(k)}$ in element $D^{(k)}$, that is, $u(x, t)$ is approximated by

$$u(x, t) \simeq u_h^{(k)}(x, t) = \sum_{i=1}^{N_p} u_h^{(k)}(x_i, t) \ell_i^{(k)}(x), \quad x \in D^{(k)}, \quad (4.3)$$

we refer to the approximation (4.3) as the *nodal* representation of $u_h^{(k)}$. The expansion coefficients are exactly the values of the approximate solution $u_h^{(k)}$ at the *nodal points* $x_i^{(k)}$ in $D^{(k)}$. Hence, the nodal approach directly mimics the behavior of the solution within one element, which is useful in the graphical analysis of the solutions of applied problems. The nodal representation (4.3) was used for computations throughout this thesis. Let us now discuss how to choose the nodal points. We introduce a mapping from a reference element,

$$I = [r = -1, r = 1], \quad (4.4)$$

to the element

$$D^{(k)} = [x = x_l^{(k)}, x = x_r^{(k)}] \quad (4.5)$$

by

$$x^{(k)}(r) = x_l^{(k)} + \frac{1+r}{2} (x_r^{(k)} - x_l^{(k)}) \quad (4.6)$$

$$= x_l^{(k)} + \frac{1+r}{2} h^{(k)}, \quad h^{(k)} = x_r^{(k)} - x_l^{(k)}, \quad (4.7)$$

so that

$$x_1^{(k)} = x^{(k)}(r_1), \dots, x_{N_p}^{(k)} = x^{(k)}(r_{N_p}) \quad (4.8)$$

for all elements k . The Lagrange polynomials (4.2) are related to the Lagrange polynomials on the reference element

$$\ell_i(r) \equiv \prod_{\substack{j=1 \\ j \neq i}}^{Np} \frac{r - r_j}{r_i - r_j}, \quad r \in I, \quad i = 1, \dots, Np \quad (4.9)$$

by the formula

$$\ell_i^{(k)}(x) \Big|_{x=x^{(k)}(r)} = \ell_i(r). \quad (4.10)$$

Consequently, in computations, derivatives and integrals on each element $D^{(k)}$ can be expressed in terms of quantities defined on the reference element I , independent of k , and the basis needs to be computed just once (for the reference element). The Lagrange polynomials imply orthogonality,

$$\ell_i(r_j) = \delta_{ij}, \quad (4.11)$$

which will be useful in the further derivations.

For the nodal points $r_1, \dots, r_{Np} \in I$, we choose the so-called Legendre-Gauss-Lobatto quadrature points. This choice assures that u_h given in (4.3) is the interpolant polynomial of order N that is (in a precise mathematical sense) closest to the best approximating polynomial of order N (see [35, Sec. 3.1]).

4.1.3 Deriving the weak form in a dG framework

Let us consider the 1-D pure advection problem to demonstrate the steps that are necessary to derive a weak formulation in the dG framework:

$$\begin{aligned} \frac{\partial u}{\partial t} + a \frac{\partial u}{\partial x} &= 0 & \text{on } \Omega = (L, R), \quad t > 0 \\ u(x, 0) &= u_0(x) & \text{on } \Omega \\ u(L, t) &= g(t) & \text{for } t \geq 0 \end{aligned} \quad (4.12)$$

We assume $a = \text{const}$, $a > 0$, and $u_0(x)$ and $g(t)$ denote initial and Dirichlet boundary conditions, respectively. To understand the physical meaning of equation (4.12), let us say that the solution variable u denotes a particle concentration. Imagine a single neutrally buoyant particle that is released into a flow of pure water, for example in a pipe, at coordinate $x = L$. The particle concentration at $t = 0$ is denoted by c_0 . Experience tells us that the particle would be transported through the domain at the velocity a of the fluid towards the other end of the domain, $x = R$; and with it, a peak in particle concentration is advectively transported through the domain.

4.1.4 Step 1: Weak formulation

Equation (4.12) holds in each material point of the domain. For computational purposes, (4.12) is usually restated in an equivalent weak formulation that relaxes the requirement of pointwise validity. To derive the weak formulation, we first multiply

equation (4.12) with an arbitrary test function φ . We require the resulting equation to be zero in an average sense, i.e. when multiplied by φ and then integrated over each element:

$$\int_{D^{(k)}} \frac{\partial u}{\partial t} \varphi \, dx + \int_{D^{(k)}} a \frac{\partial u}{\partial x} \varphi \, dx = 0, \quad k = 1, \dots, K. \quad (4.13)$$

Note that the above formulation applies to each single element; there is no formalism so far connecting the elements to each other. We now integrate the second integral in (4.13) by parts using the product rule:

$$\int_{D^{(k)}} \frac{\partial u}{\partial t} \varphi \, dx - a \int_{D^{(k)}} u \frac{\partial \varphi}{\partial x} \, dx + a \int_{D^{(k)}} \frac{\partial u}{\partial x} \varphi \, dx = 0. \quad (4.14)$$

Next, Gauss' theorem

$$\int_{D^{(k)}} \partial_x(\bullet) = \int_{\partial D^{(k)}} (\bullet) \hat{n}_x, \quad (4.15)$$

is exploited to obtain a surface integral from the last term. Here, \hat{n}_x is the outward facing normal of the element boundary (in 1D, \hat{n}_x has the value -1 on the left and 1 on the right boundary of an element). We obtain:

$$\int_{D^{(k)}} \frac{\partial u}{\partial t} \varphi \, dx - a \int_{D^{(k)}} u \frac{\partial \varphi}{\partial x} \, dx = -a \int_{\partial D^{(k)}} (u \varphi) \hat{n}_x \, dx, \quad (4.16)$$

and equivalently,

$$\int_{D^{(k)}} \frac{\partial u}{\partial t} \varphi \, dx - a \int_{D^{(k)}} u \frac{\partial \varphi}{\partial x} \, dx = -[a u \varphi]_{x_l^{(k)}}^{x_r^{(k)}}. \quad (4.17)$$

and $x_l^{(k)}$ and $x_r^{(k)}$ are the coordinates of the right and left element boundaries, respectively, cf. Figure 4.1. The term on the right hand side

$$-[a u \varphi]_{x_l^{(k)}}^{x_r^{(k)}} = -a \left(u(x_r^{(k)}) \varphi(x_r^{(k)}) - u(x_l^{(k)}) \varphi(x_l^{(k)}) \right) \quad (4.18)$$

is defined only on the boundary of the element. Hence, as the elements of the computational domain are formally disconnected, this term establishes a connection between the elements.

In a Finite Element framework, the derivation of the weak form is similar, but the integration is not over one element, $\int_{D^{(k)}}$, but over the whole domain, \int_{Ω} . In FEM, the connection between the elements is established by requiring the basis functions to be continuous at element boundaries. In that case, the right-hand side term of (4.17) would be related to the boundary of the computational domain, and can be used e.g. to apply a Neumann boundary condition. In the dG context, the right-hand side term is related to the boundary of a single *element*, and can be used to apply "boundary conditions" to the single elements. These "element boundary conditions" are termed *numerical flux*, and connect the single elements to each other, cf. Section 4.1.8.

4.1.5 Step 2: Weak form in discrete setting

The weak form of (4.12), equation (4.17), will now be discretized as follows:

- The numerical approximation of the value of u on element k will be called $u_h^{(k)}$ and approximated using a nodal expansion, equation (4.3).
- The Lagrange polynomials $\ell_i^{(k)}$ are used for the test function φ .
- The value of u on the element boundary is approximated by a *numerical flux* u^* .

We obtain the following discrete weak form:

$$\int_{D^{(k)}} \frac{du_h^{(k)}}{dt} \ell_i^{(k)} dx - a \int_{D^{(k)}} u_h^{(k)} \frac{d\ell_i^{(k)}}{dx} dx = - \left[a u^* \ell_i^{(k)} \right]_{x_l^{(k)}}^{x_r^{(k)}} \quad (4.19)$$

The introduction of the numerical flux is the crucial step in the dG approach. Recall that we have an element-wise defined formulation, where the elements are only connected via the right-hand side term. The introduction of the numerical flux implies the assumption that a global solution can be recovered by correctly choosing the inter-element flux. The question is of course how to formulate this numerical flux in a way that a meaningful global solution is recovered. Although there are guidelines for the choice of the flux, we have considerable freedom in this regard [35].

By integrating equation (4.19) by parts again, we obtain a formulation that Hesthaven [35] calls "strong form", but should not be confused with the strong form used in a Finite Element context. We will refer to this formulation as "discrete strong form":

$$\int_{D^{(k)}} \frac{d}{dt} \left(u_h^{(k)} \right) \ell_i^{(k)} dx + a \int_{D^{(k)}} \ell_i^{(k)} \frac{d}{dx} \left(u_h^{(k)} \right) dx = \left[a \left(u - u^* \right) \ell_i^{(k)} \right]_{x_\ell}^{x_r}. \quad (4.20)$$

4.1.6 Useful relations in 1D

At this stage, it makes sense to introduce the following definitions and relations that will be necessary for a compact notation of the further derivations. First, integrals over the physical elements $D^{(k)}$ and the unit element I of products of Lagrange polynomials are expressed as so-called mass matrices $\mathbf{M}^{(k)}$, \mathbf{M} ,

$$M_{ij}^{(k)} = \int_{D^{(k)}} \ell_i^{(k)}(x) \ell_j^{(k)}(x) dx, \quad \mathbf{M}^{(k)} = \left(M_{ij}^{(k)} \right), \quad (4.21)$$

$$M_{ij} = \int_I \ell_i(r) \ell_j(r) dr, \quad \mathbf{M} = \left(M_{ij} \right), \quad (4.22)$$

related by

$$M_{ij}^{(k)} = \frac{h^{(k)}}{2} M_{ij}, \quad \mathbf{M}^{(k)} = \frac{h^{(k)}}{2} \mathbf{M}. \quad (4.23)$$

Integrals of products of a Lagrange polynomial and its derivative define the stiffness matrices $\mathbf{S}^{(k)}$, \mathbf{S} ,

$$S_{ij}^{(k)} = \int_{D^{(k)}} \ell_i^{(k)}(x) \frac{\partial}{\partial x} (\ell_j^{(k)}(x)) \, dx, \quad \mathbf{S}^{(k)} = (S_{ij}^{(k)}), \quad (4.24)$$

$$S_{ij} = \int_I \ell_i(r) \frac{\partial}{\partial r} (\ell_j(r)) \, dr, \quad \mathbf{S} = (S_{ij}), \quad (4.25)$$

related by

$$S_{ij}^{(k)} = S_{ij}, \quad \mathbf{S}^{(k)} = \mathbf{S}. \quad (4.26)$$

Numerical derivatives are computed using the matrix

$$(D_r)_{ij} = \frac{d}{dr} (\ell_j(r))|_{r_i}, \quad \mathbf{D}_r = ((D_r)_{ij}), \quad (4.27)$$

which is related to the Vandermonde matrix \mathbf{V} and the matrix \mathbf{V}_r given by

$$V_{ij} = \tilde{P}_{j-1}(r_i), \quad \mathbf{V} = (V_{ij}), \quad (4.28)$$

$$(V_r)_{ij} = \left. \frac{d}{dr} (\tilde{P}_{j-1}(r)) \right|_{r_i}, \quad \mathbf{V}_r = ((V_r)_{ij}), \quad (4.29)$$

see (4.31) below. Here, $\tilde{P}_0, \dots, \tilde{P}_N$ are the (orthonormal) Legendre polynomials¹ of order N . Finally, the connections between the above definitions are given by the relations

$$\mathbf{M} = (\mathbf{V}\mathbf{V}^T)^{-1}, \quad (4.30)$$

$$\mathbf{D}_r = \mathbf{V}_r \mathbf{V}^{-1}, \quad (4.31)$$

$$\mathbf{S} = \mathbf{M}\mathbf{D}_r. \quad (4.32)$$

For the derivations of (4.30) and (4.31) see [35, Ch. 3]. Note that the two matrices \mathbf{V} and \mathbf{V}_r are sufficient to express all the matrices, that is, \mathbf{M} , \mathbf{D}_r , \mathbf{S} , that are necessary to compute the approximate solution.

4.1.7 From weak form and basis to computer implementation

We shall now see how the above strong form can be transferred into a formulation that is suitable for computer implementation. The following derivations may appear a bit tedious; however they will lead to a final formulation that illustrates some of the advantages of the nodal dG method and can directly be implemented in a computer code. Moreover, the derivations should facilitate the understanding of the example codes in the book by Hesthaven & Warburton [35]. The general strategy outlined in this section is the same for most conservation laws. Some additional complications arise when second derivatives must be approximated (cf. 4.1.9) or

¹The Legendre polynomials of order n are obtained by the Gram-Schmidt orthonormalization process with respect to the inner product $\langle f, g \rangle = \int_{-1}^1 f(x)g(x) \, dx$, and starting from the linearly independent polynomials $1, x, x^2, \dots, x^n$.

when solutions are discontinuous, but those complications will just add some details, while the basic approach is the same. In that sense, this section may serve as a cookbook on the derivation of a spatially discretized version of a conservation law for numerical implementation.

The polynomial expansion introduced in (4.3) is used for the approximation of $u_h^{(k)}$ and repeated here for clarity:

$$u(x, t) \simeq u_h^{(k)}(x, t) = \sum_{j=1}^{N_p} u_h^{(k)}(x_j, t) \ell_j^{(k)}(x) \quad (4.33)$$

Plugging into the strong form (4.20), on the left hand side we have

$$\begin{aligned} \int_{D^{(k)}} \frac{\partial}{\partial t} \left(\sum_{j=1}^{N_p} u_h^{(k)}(x_j, t) \ell_j^{(k)}(x) \right) \ell_i^{(k)}(x) \, dx \\ + a \int_{D^{(k)}} \ell_i^{(k)}(x) \frac{\partial}{\partial x} \left(\sum_{j=1}^{N_p} u_h^{(k)}(x_j, t) \ell_j^{(k)}(x) \right) \, dx. \end{aligned} \quad (4.34)$$

Recalling the definitions (4.21) and (4.24) and introducing the vector

$$\mathbf{u}_h^{(k)}(t) = \begin{pmatrix} u_h^{(k)}(x_1, t) \\ \vdots \\ u_h^{(k)}(x_{N_p}, t) \end{pmatrix}, \quad (4.35)$$

one can easily see that (4.34) is the i^{th} component of the vector

$$\mathbf{M}^{(k)} \frac{d}{dt} \left(\mathbf{u}_h^{(k)} \right) + a \mathbf{S}^{(k)} \mathbf{u}_h^{(k)}. \quad (4.36)$$

Next, we refer to the right-hand side of (4.20) and introduce the vector

$$\boldsymbol{\ell}^{(k)}(x) = \begin{pmatrix} \ell_1^{(k)}(x) \\ \vdots \\ \ell_{N_p}^{(k)}(x) \end{pmatrix}, \quad (4.37)$$

so that the right-hand side of (4.20) is the i^{th} component of the vector

$$\left[a (u - u^*) \boldsymbol{\ell}^{(k)} \right]_{x_l^{(k)}}^{x_r^{(k)}} \quad (4.38)$$

Using the property $\ell_i^{(k)}(x_j^{(k)}) = \delta_{ij}$ of the Lagrange polynomials, we have

$$\boldsymbol{\ell}^{(k)}(x_l^{(k)}) = \begin{pmatrix} 1 \\ 0 \\ \vdots \\ 0 \end{pmatrix}, \quad \boldsymbol{\ell}^{(k)}(x_r^{(k)}) = \begin{pmatrix} 0 \\ \vdots \\ 0 \\ 1 \end{pmatrix}. \quad (4.39)$$

Defining the new matrix

$$\boldsymbol{\xi} = \begin{pmatrix} \ell^{(k)}(x_l^{(k)}) & \ell^{(k)}(x_r^{(k)}) \end{pmatrix} = \begin{pmatrix} 1 & 0 \\ 0 & \vdots \\ \vdots & 0 \\ 0 & 1 \end{pmatrix} \quad (4.40)$$

and the vector

$$\mathbf{d}_{\mathbf{u}}^{(k)}(t) = \begin{pmatrix} -a \left(u_l^{(k)} - u^*(x_l^{(k)}) \right) \\ a \left(u_r^{(k)} - u^*(x_r^{(k)}) \right) \end{pmatrix}, \quad (4.41)$$

expression (4.38) can be compactly written as

$$\boldsymbol{\xi} \mathbf{d}_{\mathbf{u}}^{(k)}. \quad (4.42)$$

Now that we have (4.36) and (4.42), the N_p equations in (4.20) can be written in matrix form as

$$\mathbf{M}^{(k)} \frac{d}{dt} \left(\mathbf{u}_h^{(k)} \right) + a \mathbf{S}^{(k)} \mathbf{u}_h^{(k)} = \boldsymbol{\xi} \mathbf{d}_{\mathbf{u}}^{(k)}. \quad (4.43)$$

Our goal is to derive a spatial semidiscretization, that is, to have an expression on the right-hand side that is discretized in space and can be calculated on the computer; and to have the time derivative on the left hand side, whose discretization is left for later. So let us rearrange (4.43) using some of the relations in Section 4.1.6. We obtain:

$$\begin{aligned} \frac{d}{dt} \left(\mathbf{u}_h^{(k)} \right) &= -a \frac{2}{h^{(k)}} \mathbf{M}^{-1} \mathbf{S} \mathbf{u}_h^{(k)} + \frac{2}{h^{(k)}} \mathbf{M}^{-1} \boldsymbol{\xi} \mathbf{d}_{\mathbf{u}}^{(k)} \\ &= -a \frac{2}{h^{(k)}} \mathbf{D}_r \mathbf{u}_h^{(k)} + \frac{2}{h^{(k)}} \Upsilon \mathbf{d}_{\mathbf{u}}^{(k)}. \end{aligned} \quad (4.44)$$

Here, the so-called lift matrix

$$\Upsilon = \mathbf{M}^{-1} \boldsymbol{\xi} \quad (4.45)$$

was introduced. The superscript (k) indicates that this expression is valid for each single element. We could easily calculate the right-hand side on the computer by simply looping over all elements. However, by introducing a few more matrices, a compact notation can be obtained for (4.44) that allows the calculation of the right-

hand side for the complete domain in one single step. The required matrices are:

$$\mathbf{u}_h = \begin{pmatrix} \mathbf{u}_h^{(1)} & \dots & \mathbf{u}_h^{(K)} \end{pmatrix} = \begin{pmatrix} u_1^{(1)} & \dots & u_1^{(K)} \\ \vdots & \ddots & \vdots \\ u_{N_p}^{(1)} & \dots & u_{N_p}^{(K)} \end{pmatrix}, \quad (4.46)$$

$$\mathbf{J} = \mathbf{x}_r = \begin{pmatrix} \frac{h^{(1)}}{2} & \dots & \frac{h^{(K)}}{2} \\ \vdots & \ddots & \vdots \\ \frac{h^{(1)}}{2} & \dots & \frac{h^{(K)}}{2} \end{pmatrix}, \quad \mathbf{r}_x = \begin{pmatrix} \frac{2}{h^{(1)}} & \dots & \frac{2}{h^{(K)}} \\ \vdots & \ddots & \vdots \\ \frac{2}{h^{(1)}} & \dots & \frac{2}{h^{(K)}} \end{pmatrix}, \quad (4.47)$$

$$\begin{aligned} \mathbf{d}_u &= \begin{pmatrix} \mathbf{d}_u^{(1)} & \dots & \mathbf{d}_u^{(K)} \end{pmatrix} \\ &= \begin{pmatrix} -a \left(u_l^{(1)} - u^*(x_l^{(1)}) \right) & \dots & -a \left(u_l^{(K)} - u^*(x_l^{(K)}) \right) \\ a \left(u_r^{(1)} - u^*(x_r^{(1)}) \right) & \dots & a \left(u_r^{(K)} - u^*(x_r^{(K)}) \right) \end{pmatrix}, \text{ and} \end{aligned} \quad (4.48)$$

$$\mathbf{F}_{sc} = \begin{pmatrix} \frac{h^{(1)}}{2} & \dots & \frac{h^{(K)}}{2} \\ \frac{h^{(1)}}{2} & \dots & \frac{h^{(K)}}{2} \end{pmatrix} \quad (4.49)$$

Now, the semi-discretized equation can be formulated as

$$\frac{d}{dt} (\mathbf{u}_h) = -a \mathbf{r}_x \odot (\mathbf{D}_r \otimes \mathbf{u}_h) + \Upsilon \otimes (\mathbf{F}_{sc} \odot \mathbf{d}_u). \quad (4.50)$$

It is important to note that in this expression, the symbols \odot and \otimes were used to clearly discriminate between component-wise matrix multiplication $(\mathbf{A} \odot \mathbf{B})_{ij} = A_{ij}B_{ij}$ and the usual matrix product $(\mathbf{A} \otimes \mathbf{B})_{ij} = \sum_k A_{ik}B_{kj}$ (i.e., \otimes does *not* relate to a dyadic product here).

Let us now note some properties of the formulation (4.50). First, we refer to the first term on the right-hand side of (4.50), $-a \mathbf{r}_x \odot (\mathbf{D}_r \otimes \mathbf{u}_h)$. Here, the variable a and the matrices \mathbf{r}_x and \mathbf{D}_r are constants and have to be defined or calculated just once at the beginning of a computation. The values of the solution variable \mathbf{u}_h are stored in a matrix where each column contains only the information from one single element, cf. (4.46). The first right-hand side term of (4.50) can easily be computed on n parallel processors by splitting the matrices \mathbf{r}_x and \mathbf{u}_h column-wise into n submatrices and letting each processor calculate the term $-a \mathbf{r}_x^i \odot (\mathbf{D}_r \otimes \mathbf{u}_h^i)$, $i = 1, \dots, n$. No communication between the processors is necessary, there is no information exchange between the elements here. For the term $\Upsilon \otimes (\mathbf{F}_{sc} \odot \mathbf{d}_u)$ in (4.50), the situation is slightly different: Υ and \mathbf{F}_{sc} are constant matrices that are calculated only once, and \mathbf{d}_u can be subdivided column-wise. However, to *assemble* the matrix \mathbf{d}_u , information from each adjacent element is necessary, cf. equation (4.48). These facts reveals one of the major strengths of the nodal dG method: Apart from the flux term, all operations are element-local, which makes them extremely suitable for parallel computation.

In particular, decades of research have been devoted to efficient parallel implementations of matrix multiplications, and hence, sophisticated libraries exist that can be used off-the-shelf to compute these products. The algorithms written for this thesis were implemented in Python. The Python package for numerical computing, NumPy, was used. The NumPy package can be custom-compiled to use optimized BLAS libraries (Basic Linear Algebra Subprograms), for example OpenBLAS (cf. [85] and references therein) or ATLAS (Automatically Tuned Linear Algebra Subsystems, cf.

[86]). In the numerical tests carried out for this thesis, OpenBLAS turned out to deliver the better overall performance. Yet, the problem sizes investigated were so small that enhanced parallelism (more than two processors) yielded no advantages in computation times.

4.1.8 The numerical flux

Thus far, no assumptions or choices were made regarding the numerical flux u^* . As the flux is the only connection between the adjacent elements, it is now time to make this choice. We recall that a dG scheme is identical to an FE scheme as long as we pick out just a single element, and ignore the other elements. The role of the numerical flux is to provide "boundary conditions" for the otherwise disconnected elements (here the term *boundary* refers to the boundary of an *element*, hence the quotation marks. Element boundaries are called *faces* for a clear distinction, and the intersection of two faces is called *vertex*). Taking the simple advection example, the first and simplest idea would be to just consider a central flux $u^* = \{\{u\}\}$, which is the average of the values at each side of the vertex. However, if we know from our knowledge of the equation in which way the information is traveling, it would intuitively be advisable to have a stronger weighting of the upstream information, because any downstream information will anyway "flow out of the element" in the next timestep. That is exactly the idea behind upwind numerical fluxes, which are suitable for all convection dominated problems because they involve information flowing in a preferred direction. We introduce the upwind Lax-Friedrichs flux

$$u^* = \{\{u\}\} + \frac{1-\alpha}{2} [[u]] = \frac{u_{int} + u_{ext}}{2} + \frac{1-\alpha}{2} (\hat{n}_{int} u_{int} + \hat{n}_{ext} u_{ext}). \quad (4.51)$$

Here, u_{int} denotes the *interior* value of u_h at the left or right face of element k ; while u_{ext} denotes the *exterior* value of u_h at the left or right face of element k , cf. Figure 4.1. The parameter α specifies the amount of upwinding. In case of $\alpha = 1$, a purely central flux is recovered, while $\alpha = 0$ involves a stronger weighting of upstream information, which is termed upwinding. In (4.51), we have used the *average* value of the interior and exterior solution values,

$$\{\{u\}\} = \frac{u_{int} + u_{ext}}{2}, \quad (4.52)$$

and the *jump* of the interior and exterior solution values,

$$[[u]] = \hat{n}_{int} u_{int} + \hat{n}_{ext} u_{ext}. \quad (4.53)$$

With the flux (4.51), we obtain in the first line of (4.48) the connection between the left face of element k and the right face of element $k-1$:

$$\begin{aligned} u_1^{(k)} - u^*(x_1^{(k)}) &= \\ u_1^{(k)} - \left[\frac{u_1^{(k)} + u_{Np}^{(k-1)}}{2} + \frac{1-\alpha}{2} \left((-1) u_1^{(k)} + (+1) u_{Np}^{(k-1)} \right) \right] &= \\ \frac{1}{2} \left(u_1^{(k)} - u_{Np}^{(k-1)} \right) (1 + (1-\alpha)) & \end{aligned} \quad (4.54)$$

and in the second line the connection between the right face of element k and the left face of element $k + 1$

$$\begin{aligned} u_{N_p}^{(k)} - u^*(x_{N_p}^{(k)}) &= \\ u_{N_p}^{(k)} - \left[\frac{u_{N_p}^{(k)} + u_1^{(k+1)}}{2} + \frac{1-\alpha}{2} \left((+1) u_{N_p}^{(k)} + (-1) u_1^{(k+1)} \right) \right] &= \\ \frac{1}{2} \left(u_{N_p}^{(k)} - u_1^{(k+1)} \right) (1 - (1-\alpha)). \end{aligned} \quad (4.55)$$

The importance of the choice of the flux - in particular, the importance of using an upwind flux for convective problems - is nicely illustrated by Figures 4.2 and 4.3. A multitude of other choices for the flux are available (cf. [35, p.32]), originating from FV methods. The simple Lax-Friedrichs flux, in general form given by

$$f^{LF}(u_{int}, u_{ext}) = \{\{u\}\} + \frac{C}{2} \hat{n} \cdot [[u]] = \frac{f(u_{int}) + f(u_{ext})}{2} + \frac{C}{2} \hat{n} \cdot (u_{int} - u_{ext}) \quad (4.56)$$

is efficient for most problems, but not very accurate, as it is somewhat dissipative, cf. [35]. In case of the flux function $f(u) = au$, the simple upwind flux (4.51) is recovered, i.e. $C = a$. The significance of C is that it is a maximum linearized acoustic wave speed for a given system. In case of a system of conservation laws, e.g. the Euler or compressible Navier-Stokes equations, C is determined by the maximum eigenvalue λ of the flux Jacobian,

$$C = \max_u \left| \lambda \left(\hat{n} \cdot \frac{\partial \mathbf{f}}{\partial \mathbf{u}} \right) \right|, \quad (4.57)$$

where \mathbf{f} denotes the vector of flux functions and \mathbf{u} the vector of unknown fields.

Applying boundary conditions - advection

As outlined above, on the element level, the dG-formulation corresponds to a FEM formulation, and we use the numerical flux to apply boundary conditions for each element. The application of outer boundary conditions is now straightforward: if we encounter a value of u in the expression for $\mathbf{d}_{\mathbf{u}}$ that lies outside the domain, we just insert the value of the boundary condition. For this 1D case, the expression for element $D^{(1)}$ at the left end of the domain would be

$$\mathbf{d}_{\mathbf{u}}^{(1)} = \left(\frac{a}{2} \left\{ \left(u_l^{(1)} - g(t) \right) (-1 - (1-\alpha)) \right\} \right) \quad (4.58)$$

with $g(t)$ being the boundary condition. We recall that the flow direction is assumed from left to right, $a > 0$, and the boundary condition is given at the left domain boundary, $x = L$. In this case, where we only have a first derivative, it suffices to have just one boundary condition on u . Physical intuition tells us that the boundary condition must be applied at the inflow, i.e. on the left end of the domain if $a > 0$ and on the right end if $a < 0$, because we know from the physics behind the equation that the information is flowing downstream. Thus, a boundary condition applied upstream results in the boundary information being transported advectively through the domain at velocity a , while applying a boundary condition on the downstream end

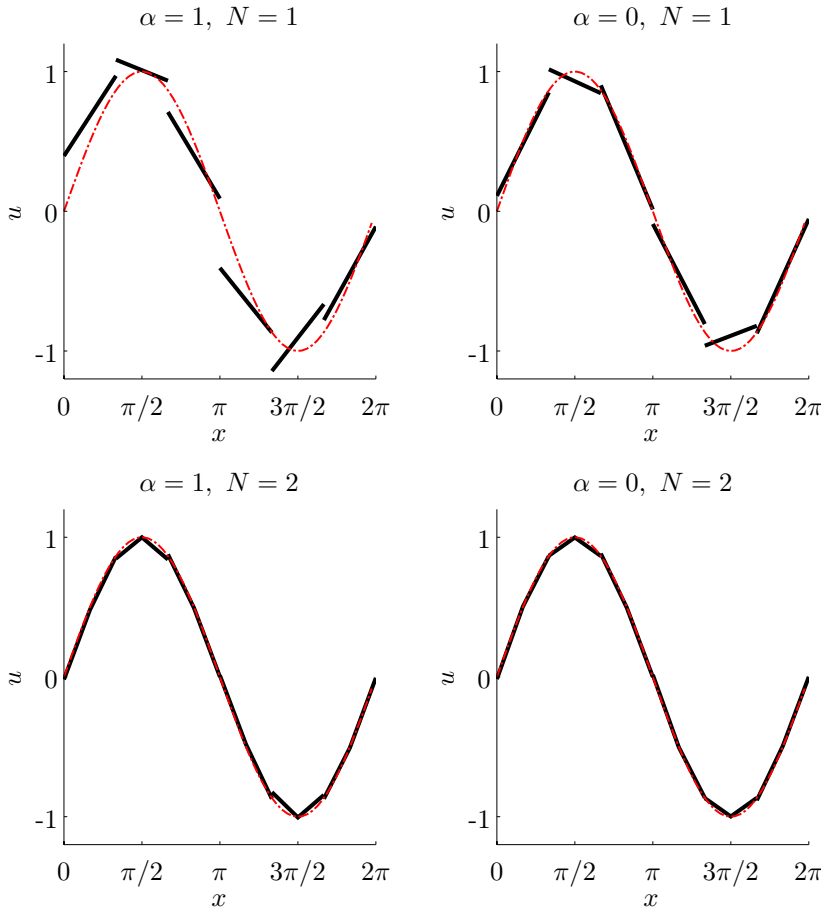


Figure 4.2: Element-wise results (black) and analytic solution (red) for the simple advection problem (4.12) at time $t = 2\pi$ with initial condition $u_0 = \sin(x)$, boundary condition $u_L = \sin(t)$ at the left boundary, advection speed $a = 1$ and $K = 6$ elements. The upper two panels show the results for approximation order $N = 1$ (cf. Section 4.1.2), the lower panels for $N = 2$. The left two panels illustrate the results using a central flux, that is, $\alpha = 1$ in (4.51), and right two panels for an upwind flux, $\alpha = 0$ in (4.51). If the upwind flux is used, i.e., when the numerical flux is adjusted to the propagation direction of the advective information transport, the numerical solution is closer to the analytical solution and the jumps between the element endpoints are diminished. If the approximation order is increased, the straight black lines representing the elementwise solution are allowed to have a kink in the middle. The solution within one element is continuous, while at the element boundaries, the solution is allowed to be discontinuous.

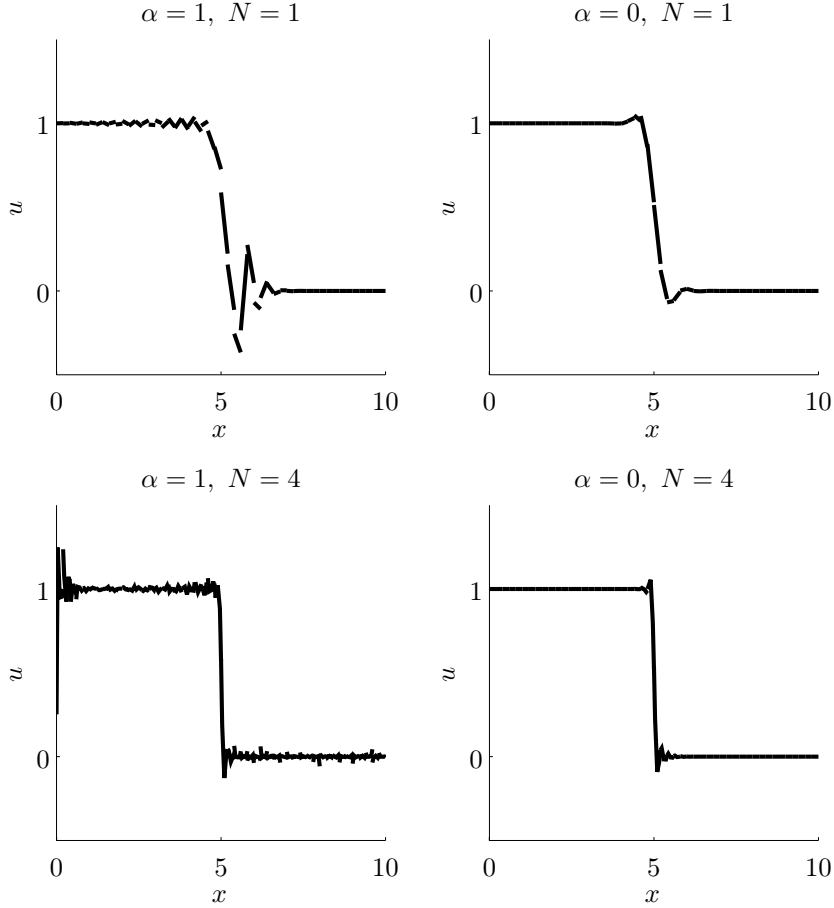


Figure 4.3: Element-wise results for the simple advection problem (4.12) at time $t = 5$ with initial condition $u_0 = 0$, boundary condition $u_L = 1$ at the left boundary, advection speed $a = 1$ and $K = 50$ elements. The upper two panels show results for approximation order $N = 1$ (cf. Section 4.1.2), the lower panels for $N = 4$. The left two panels illustrate results using a central flux, that is, $\alpha = 1$ in (4.51), and right two panels for an upwind flux, that is, $\alpha = 1$ in (4.51). The oscillations of the solution near the jump are due to the well-known Gibbs' phenomenon. In case of a central flux, the oscillations propagate into both directions, while the upwind flux keeps the oscillations localized. Higher approximation order leads to more oscillations due to the Gibbs' phenomenon.

of the domain would result in the boundary information never entering the domain. It remains the question which value to prescribe for u on the downstream boundary. According to the considerations above, an arbitrary value can be prescribed, because the information never enters the domain. Hence zero is prescribed for the whole second line of $\mathbf{d}_u^{(K)}$, resulting in

$$\mathbf{d}_u^{(K)} = \begin{pmatrix} \frac{a}{2} \left\{ \left(u_1^{(K)} - u_{Np}^{(K-1)} \right) (-1 - (1 - \alpha)) \right\} \\ 0 \end{pmatrix}. \quad (4.59)$$

Here, we have focused on the application of Dirichlet boundary conditions. Neumann boundary conditions are discussed in Section 4.1.9.

4.1.9 Treatment of second spatial derivatives - the mixed method

So far, we have been concerned with the spatial discretization of a first spatial derivative $\frac{\partial u}{\partial x}$. When it comes to the discretization of derivatives of higher order, there are two possible ways to go: one can either construct operators calculating those derivatives directly (analogously to the operator \mathbf{S} , which calculates first derivatives); or one can write the original equation as a system of equations where each equation contains only first derivatives. It turns out that the second path is computationally more convenient [35]. It will be described here.

The 1-D advection-diffusion equation is taken as a sample problem:

$$\begin{aligned} \frac{\partial u}{\partial t} + a \frac{\partial u}{\partial x} - \epsilon \frac{\partial^2 u}{\partial x^2} &= 0 && \text{on } \Omega = (L, R), \quad t > 0 \\ u(x, 0) &= c_0(x) && \text{on } \Omega \\ u(L, t) = g(t), \quad u(R, t) &= h(t) && \text{for } t \geq 0 \end{aligned} \quad (4.60)$$

We assume $a > 0$, $\epsilon > 0$ and Dirichlet boundary conditions. Physically, equation (4.60) describes a process similar to that described in equation (4.12), just as an additional feature, the variable u is also transported diffusively through the domain. Readopting the example of water and a single neutrally buoyant grain flowing through a pipe at velocity a , imagine that the grain is replaced by a droplet of ink. As ink and water are miscible, the droplet is advectively transported at velocity a , but it also changes its shape and "smears out" due to the fact that miscible mixtures always try to achieve uniform distribution of the constituents within the domain. Hence when we observe how the concentration of paint within the domain evolves, we see a sharp concentration peak starting at the left end of the domain, and while that peak is translated, it also gets wider due to diffusion.

Introducing the auxiliary variable

$$q = \sqrt{\epsilon} \frac{\partial u}{\partial x}, \quad (4.61)$$

equation (4.60) can be written as a system of first-order equations (cf. [5]),

$$\frac{\partial u}{\partial t} + a \frac{\partial u}{\partial x} + \frac{\partial}{\partial x} (-\sqrt{\epsilon} q) = 0, \quad (4.62)$$

$$q + \frac{\partial}{\partial x} (-\sqrt{\epsilon} u) = 0. \quad (4.63)$$

Equations (4.62) and (4.63) are both discretized using the 'cookbook' method outlined above. The steps necessary are repeated here in short for clarity:

- Multiply with a test function and require the resulting equation to be orthogonal to all test functions.
- Integrate by parts using product rule and Gauss' theorem to obtain the weak form.
- Go to the discrete setting:
 - Replace all solution variables (\bullet) inside the volume by their discrete counterparts (\bullet_h).
 - Replace all solution variables on the boundary $[\bullet]_{x_r}^{x_l}$ by a numerical flux $[\bullet^*]_{x_r}^{x_l}$. In this case, as the numerical flux of u occurs in two different equations, and hence we will differentiate between u_u^* and u_q^* .
 - Replace the test functions with their discrete counterparts, the Lagrange polynomials, to arrive at the "discrete weak form".
- Integrate by parts again to obtain the "discrete strong form":

$$\begin{aligned} \int_{D^{(k)}} \frac{\partial}{\partial t} \left(u_h^{(k)} \right) \ell_j^{(k)} dx + a \int_{D^{(k)}} \ell_j^{(k)} \frac{\partial}{\partial x} \left(u_h^{(k)} \right) dx - \sqrt{\epsilon} \int_{D^{(k)}} \ell_j^{(k)} \frac{\partial}{\partial x} \left(q_h^{(k)} \right) dx \\ = [a (u - u_u^*) \ell_j]_{x_l}^{x_r} + [-\sqrt{\epsilon} (q - q^*) \ell_j]_{x_l}^{x_r}, \end{aligned} \quad (4.64)$$

$$\int_{D^{(k)}} q_h^{(k)} \ell_j^{(k)} dx - \sqrt{\epsilon} \int_{D^{(k)}} \ell_j^{(k)} \frac{\partial}{\partial x} \left(u_h^{(k)} \right) dx = [-\sqrt{\epsilon} (u - u_q^*) \ell_j]_{x_l}^{x_r}. \quad (4.65)$$

- Express the solution variables as polynomial expansions using the Lagrange polynomials as a basis.
- Express all integrals over products of Lagrange polynomials in terms of the local operators $\mathbf{M}^{(k)}$ and $\mathbf{S}^{(k)}$ and obtain

$$\mathbf{M}^{(k)} \frac{d}{dt} \left(\mathbf{u}_h^{(k)} \right) + a \mathbf{S}^{(k)} \mathbf{u}_h^{(k)} - \sqrt{\epsilon} \mathbf{S}^{(k)} \mathbf{q}_h^{(k)} = \boldsymbol{\xi} \mathbf{d}_{u_u}^{(k)} + \boldsymbol{\xi} \mathbf{d}_{\mathbf{q}}^{(k)}, \quad (4.66)$$

$$\mathbf{M}^{(k)} \mathbf{q}_h^{(k)} - \sqrt{\epsilon} \mathbf{S}^{(k)} \mathbf{u}_h^{(k)} = \boldsymbol{\xi} \mathbf{d}_{u_q}^{(k)}, \quad (4.67)$$

with the definition of $\mathbf{d}_{u_u}^{(k)}$, $\mathbf{d}_{\mathbf{q}}^{(k)}$ and $\mathbf{d}_{u_q}^{(k)}$ analogous to the definition of $\mathbf{d}_{\mathbf{u}}^{(k)}$ (4.48) in the pure advection case.

- Introduce the mapping from the physical elements $D^{(k)}$ to the unit element $I^{(k)}$
- Rearrange, putting all spatial derivatives to the RHS and using the relations in Section 4.1.6:

$$\frac{d}{dt} \left(\mathbf{u}_h^{(k)} \right) = -a \frac{2}{h^{(k)}} \mathbf{D}_r \mathbf{u}_h^{(k)} + \sqrt{\epsilon} \frac{2}{h^{(k)}} \mathbf{D}_r \mathbf{q}_h^{(k)} + \Upsilon \mathbf{d}_{u_u}^{(k)} + \Upsilon \mathbf{d}_{\mathbf{q}}^{(k)}, \quad (4.68)$$

$$\mathbf{q}_h^{(k)} = \sqrt{\epsilon} \frac{2}{h^{(k)}} \mathbf{D}_r \mathbf{u}_h^{(k)} + \Upsilon \mathbf{d}_{u_q}^{(k)}. \quad (4.69)$$

- Use the matrices \mathbf{r}_x and \mathbf{F}_{sc} to come from the element-local to a global formulation:

$$\begin{aligned} \frac{d}{dt}(\mathbf{u}_h) = & -a \mathbf{r}_x \odot (\mathbf{D}_r \otimes \mathbf{u}_h) + \sqrt{\epsilon} \mathbf{r}_x \odot (\mathbf{D}_r \otimes \mathbf{q}_h) \\ & + \Upsilon \otimes (\mathbf{F}_{sc} \odot \mathbf{d}_{u_u}) + \Upsilon \otimes (\mathbf{F}_{sc} \odot \mathbf{d}_q), \end{aligned} \quad (4.70)$$

$$\mathbf{q}_h = \sqrt{\epsilon} \mathbf{r}_x \odot (\mathbf{D}_r \otimes \mathbf{u}_h) + \Upsilon \otimes (\mathbf{F}_{sc} \odot \mathbf{d}_{u_q}). \quad (4.71)$$

It turns out that we have obtained an explicit algebraic relation for \mathbf{q}_h which can be computed first and then used in the equation for \mathbf{u}_h . What remains is to choose the fluxes u_u^* , u_q^* and q^* . Intuitively, one would probably choose the upwind flux from the pure advection case for u_u^* because it has proven to work well and because we have a preferred propagation direction, which is reflected by the upwinding; and a central flux for u_q^* and q^* , because the diffusion term has no preferred direction of propagation. Another possibility is to choose only upwind fluxes, which leads to a more stable scheme, known as local discontinuous Galerkin (LDG) method in the literature, first proposed by Cockburn & Shu [16].

$$u_u^* = \{\{u\}\} + \frac{1-\alpha}{2} [[u]] = \frac{u_{int} + u_{ext}}{2} + \frac{1-\alpha}{2} (\hat{\mathbf{n}}_{int} u_{int} + \hat{\mathbf{n}}_{ext} u_{ext}) \quad (4.72)$$

$$q^* = \{\{q\}\} + \frac{1-\alpha}{2} [[q]] = \frac{q_{int} + q_{ext}}{2} + \frac{1-\alpha}{2} (\hat{\mathbf{n}}_{int} q_{int} + \hat{\mathbf{n}}_{ext} q_{ext}) \quad (4.73)$$

$$u_q^* = \{\{u\}\} - \frac{1-\alpha}{2} [[u]] = \frac{u_{int} + u_{ext}}{2} - \frac{1-\alpha}{2} (\hat{\mathbf{n}}_{int} u_{int} + \hat{\mathbf{n}}_{ext} u_{ext}) \quad (4.74)$$

Note that u_u^* is different from u_q^* in that the upwinding terms have opposite signs and hence upwinding of u and q is done in opposite directions, which is essential for stability. We obtain the following expressions for $\mathbf{d}_{u_u}^{(k)}$, $\mathbf{d}_q^{(k)}$ and $\mathbf{d}_{u_q}^{(k)}$:

$$\mathbf{d}_{u_u}^{(k)} = \begin{pmatrix} \frac{a}{2} \left\{ \left(u_1^{(k)} - u_{Np}^{(k-1)} \right) (-1 - (1-\alpha)) \right\} \\ \frac{a}{2} \left\{ \left(u_{Np}^{(k)} - u_1^{(k+1)} \right) (1 - (1-\alpha)) \right\} \end{pmatrix} \quad (4.75)$$

$$\mathbf{d}_q^{(k)} = \begin{pmatrix} -\frac{\sqrt{\epsilon}}{2} \left\{ \left(q_1^{(k)} - q_{Np}^{(k-1)} \right) (-1 - (1-\alpha)) \right\} \\ -\frac{\sqrt{\epsilon}}{2} \left\{ \left(q_{Np}^{(k)} - q_1^{(k+1)} \right) (1 - (1-\alpha)) \right\} \end{pmatrix} \quad (4.76)$$

$$\mathbf{d}_{u_q}^{(k)} = \begin{pmatrix} -\frac{\sqrt{\epsilon}}{2} \left\{ \left(u_1^{(k)} - u_{Np}^{(k-1)} \right) (-1 + (1-\alpha)) \right\} \\ -\frac{\sqrt{\epsilon}}{2} \left\{ \left(u_{Np}^{(k)} - u_1^{(k+1)} \right) (1 + (1-\alpha)) \right\} \end{pmatrix} \quad (4.77)$$

Applying boundary conditions - advection-diffusion

The technical principle of applying the boundary conditions is as before, i.e. boundary conditions are put into the \mathbf{d}_\bullet terms whenever a value outside the domain is encountered in one of the expressions. In case of the \mathbf{d}_{u_u} term, this is straight forward, as there is no difference to the advection case. But as we have written the equation as a system, the question remains what to impose in \mathbf{d}_q and \mathbf{d}_{u_q} .

If homogeneous Dirichlet boundary conditions are applied, that is, no external forcing exists and the solution is allowed to evolve naturally, exterior values $u_{Np}^{(0)}$, $q_{Np}^{(0)}$

at the left boundary and $u_1^{(K+1)}, q_1^{(K+1)}$ at the right boundary are not prescribed as fixed values, but are instead coupled to the values at the inner side of the boundary. Specifically, $u_{ext} = -u_{int}$, $q_{ext} = q_{int}$, in which case the average of u would be zero and the jump would be twice the interior value, while the average of q would be the interior value and the jump zero:

$$\{\{u\}\} = 0 \quad [[u]] = 2\hat{\mathbf{n}}_{int} u_{int} \quad (4.78)$$

$$\{\{q\}\} = q_{int} \quad [[q]] = 0 \quad (4.79)$$

For Neumann BC's, the coupling will be the other way around, i.e. $u_{ext} = u_{int}$, $q_{ext} = -q_{int}$. In case of inhomogeneous Dirichlet boundary conditions, $u_{ext} = -u_{int} + 2f(t)$, $q_{ext} = q_{int}$ is proposed with $f(t)$ the external forcing, see [35].

4.2 2-D problems

Although some complexity is added by changing the perspective to 2-D, the main principles are very similar to the 1-D case. Hence we restrict ourselves to a relatively short explanation of the necessary two-dimensional operators, and otherwise focus on a computational benchmark. For a full derivation of the operators, the reader is referred to the book by Hesthaven & Warburton [35].

4.2.1 Useful relations in 2-D

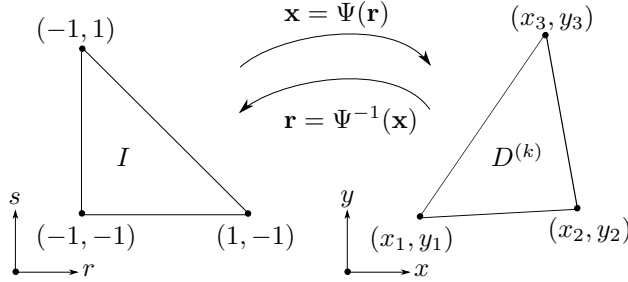


Figure 4.4: Illustration of the mapping between reference triangle I (left) and physical triangle $D^{(k)}$ (right)

In 2-D, the 1-D geometric variables x and r will be replaced by the vectors $\mathbf{x} = (x \ y)^T$ and $\mathbf{r} = (r \ s)^T$, cf. Figure 4.4. The mapping function, now from the reference triangle I to the element $D^{(k)}$ is given by

$$\mathbf{x}_i^{(k)} = \Psi^{(k)}(\mathbf{r}_i) = -\frac{r_i + s_i}{2} \mathbf{x}_1^{(k)} + \frac{r_i + 1}{2} \mathbf{x}_2^{(k)} + \frac{s_i + 1}{2} \mathbf{x}_3^{(k)}, \quad (4.80)$$

with $\mathbf{x}_1^{(k)}$, $\mathbf{x}_2^{(k)}$ and $\mathbf{x}_3^{(k)}$ denoting the vertex coordinates of the triangle $D^{(k)}$. The Jacobian of the mapping Ψ is

$$J^{(k)} = \frac{\partial x^{(k)}}{\partial r} \frac{\partial y^{(k)}}{\partial s} - \frac{\partial x^{(k)}}{\partial s} \frac{\partial y^{(k)}}{\partial r}. \quad (4.81)$$

The discrete approximation of a variable $u(\mathbf{x}, t)$ is exactly analogous to the 1-D case:

$$u(\mathbf{x}, t) \simeq u_h^{(k)}(\mathbf{x}, t) = \sum_{i=1}^{N_p} u_h^{(k)}(\mathbf{x}_i, t) \ell_i^{(k)}(\mathbf{x}) \quad (4.82)$$

Here we have introduced the two-dimensional Lagrange polynomials $\ell_i^{(k)}(\mathbf{x})$ corresponding to some grid points \mathbf{x}_i in $D^{(k)}$. The nodal points \mathbf{r}_i are first selected in the reference triangle, and the points $\mathbf{x}_i^{(k)}$ are then computed via

$$\mathbf{x}_i^{(k)} = \Psi^{(k)} \mathbf{r}_i. \quad (4.83)$$

In the 2-D case, the order N of the polynomial and the number N_p of grid points on the triangle, which is equal to the number of terms in the polynomial expansion, are connected by the relation

$$N_p = \frac{(N+1)(N+2)}{2}. \quad (4.84)$$

The 2-D Vandermonde matrix is introduced as in the 1-D case,

$$V_{ij} = \tilde{P}_{j-1}(\mathbf{r}_i), \quad \mathbf{V} = (V_{ij}) \quad (4.85)$$

with $\tilde{P}_{j-1}(\mathbf{r}_i)$ the normalized Legendre polynomial of order $j-1$ and the matrices analogous to the 1-D matrix \mathbf{V}_r defined in (4.29) are

$$(V_r)_{ij} = \left. \frac{\partial}{\partial r} (\tilde{P}_j) \right|_{\mathbf{r}_i}, \quad \mathbf{V}_r = \left((V_r)_{ij} \right), \quad (4.86)$$

$$(V_s)_{ij} = \left. \frac{\partial}{\partial s} (\tilde{P}_j) \right|_{\mathbf{r}_i}, \quad \mathbf{V}_s = \left((V_s)_{ij} \right). \quad (4.87)$$

\mathbf{V} , \mathbf{V}_r and \mathbf{V}_s are necessary to express the matrices

$$(D_r)_{ij} = \left. \frac{\partial}{\partial r} (\ell_j(r, s)) \right|_{\mathbf{r}_i}, \quad \mathbf{D}_r = \left((D_r)_{ij} \right), \quad (4.88)$$

$$(D_s)_{ij} = \left. \frac{\partial}{\partial s} (\ell_j(r, s)) \right|_{\mathbf{r}_i}, \quad \mathbf{D}_s = \left((D_s)_{ij} \right), \quad (4.89)$$

see (4.100), (4.101) below. Now, integrals of products of the Lagrange polynomials are collected in so-called mass matrices on the physical and the reference triangles:

$$M_{ij}^{(k)} = \int_{D^{(k)}} \ell_i^{(k)}(\mathbf{x}) \ell_j^{(k)}(\mathbf{x}) \, d\mathbf{x}, \quad \mathbf{M}^{(k)} = \left(M_{ij}^{(k)} \right), \quad (4.90)$$

$$M_{ij} = \int_I \ell_i(\mathbf{r}) \ell_j(\mathbf{r}) \, d\mathbf{r}, \quad \mathbf{M} = \left(M_{ij} \right), \quad (4.91)$$

related by

$$M_{ij}^{(k)} = J^{(k)} M_{ij}, \quad \mathbf{M}^{(k)} = J^{(k)} \mathbf{M}. \quad (4.92)$$

Integrals of products of a Lagrange polynomial and a derivative of a Lagrange polynomial are collected in so-called stiffness matrices, on both the physical and reference

triangles:

$$S_{x,ij}^{(k)} = \int_{D^{(k)}} \ell_i^{(k)}(\mathbf{x}) \frac{\partial}{\partial x} (\ell_j^{(k)}(\mathbf{x})) \, d\mathbf{x}, \quad \mathbf{S}_x^{(k)} = \left(S_{x,ij}^{(k)} \right), \quad (4.93)$$

$$S_{y,ij}^{(k)} = \int_{D^{(k)}} \ell_i^{(k)}(\mathbf{x}) \frac{\partial}{\partial y} (\ell_j^{(k)}(\mathbf{x})) \, d\mathbf{x}, \quad \mathbf{S}_y^{(k)} = \left(S_{y,ij}^{(k)} \right), \quad (4.94)$$

$$S_{r,ij} = \int_I \ell_i(\mathbf{r}) \frac{\partial}{\partial r} (\ell_j(\mathbf{r})) \, d\mathbf{r}, \quad \mathbf{S}_r = (S_{r,ij}), \quad (4.95)$$

$$S_{s,ij} = \int_I \ell_i(\mathbf{r}) \frac{\partial}{\partial s} (\ell_j(\mathbf{r})) \, d\mathbf{r}, \quad \mathbf{S}_s = (S_{s,ij}), \quad (4.96)$$

which are related by

$$S_{x,ij}^{(k)} = S_{r,ij}, \quad \mathbf{S}_x^{(k)} = \mathbf{S}_r, \quad (4.97)$$

$$S_{y,ij}^{(k)} = S_{s,ij}, \quad \mathbf{S}_y^{(k)} = \mathbf{S}_s. \quad (4.98)$$

The connections between the matrices referring to the reference triangle are given via the following relations:

$$\mathbf{M} = (\mathbf{V}\mathbf{V}^T)^{-1}, \quad (4.99)$$

$$\mathbf{D}_r = \mathbf{V}^{-1}\mathbf{V}_r, \quad (4.100)$$

$$\mathbf{D}_s = \mathbf{V}^{-1}\mathbf{V}_s, \quad (4.101)$$

$$\mathbf{S}_r = \mathbf{M}^{-1}\mathbf{D}_r, \quad (4.102)$$

$$\mathbf{S}_s = \mathbf{M}^{-1}\mathbf{D}_s. \quad (4.103)$$

We will also need the definitions

$$\mathbf{D}_x = \frac{\partial r}{\partial x} \mathbf{D}_r + \frac{\partial s}{\partial x} \mathbf{D}_s, \quad (4.104)$$

$$\mathbf{D}_y = \frac{\partial r}{\partial y} \mathbf{D}_r + \frac{\partial s}{\partial y} \mathbf{D}_s. \quad (4.105)$$

The definitions and relations shown above are sufficient to implement a partial differential equation in 2-D. This is exemplified in the following section for the weakly compressible Navier-Stokes equations.

4.2.2 Weakly compressible Navier-Stokes equations assuming isothermal conditions

The compressible Navier-Stokes equations for a single, weakly compressible fluid under isothermal conditions are a perfect test case for the numerical implementation of the model outlined in Chapter 3, because they are structurally very similar to the mixture equations. Moreover, numerous numerical benchmarks exist for the incompressible Navier-Stokes equations, which can be used as a validation of the approach followed in this thesis, as long as only weak compressibility is assumed. The compressible

Navier-Stokes equations in conservation form read:

$$\begin{aligned}\frac{\partial \rho}{\partial t} &= -\operatorname{div}(\rho \mathbf{u}) \\ \frac{\partial \rho \mathbf{u}}{\partial t} &= -\operatorname{div}(\rho \mathbf{u} \otimes \mathbf{u} - \mathbf{T}) + \rho \mathbf{b},\end{aligned}\tag{4.106}$$

where ρ , \mathbf{u} , \mathbf{T} and \mathbf{b} denote the fluid density, the velocity vector $\mathbf{u} = [u \ v]^T$, the viscous stress tensor and gravity, respectively. The mixture model equations presented in Chapter 3 differ from the above only in that the number of the equations is doubled, in the strong coupling which is introduced via the solid volume fraction occurring in all equations, and, less severely, the momentum interaction.

The stress tensor is decomposed into a hydrostatic pressure and an extra stress contribution,

$$\mathbf{T} = -p\mathbf{I} + \mathbf{T}_E,\tag{4.107}$$

where

$$\mathbf{T}_E = 2\mu \left(\mathbf{D} - \frac{1}{3} \operatorname{tr}(\mathbf{D}) \mathbf{I} \right)\tag{4.108}$$

and in two dimensions of a Cartesian system,

$$\mathbf{D} = \begin{pmatrix} \frac{\partial u}{\partial x} & \frac{1}{2} \left(\frac{\partial u}{\partial y} + \frac{\partial v}{\partial x} \right) \\ \frac{1}{2} \left(\frac{\partial u}{\partial y} + \frac{\partial v}{\partial x} \right) & \frac{\partial v}{\partial y} \end{pmatrix}\tag{4.109}$$

is the rate of deformation tensor (cf. Section 3.3). Hence,

$$\mathbf{T}_E = \mu \begin{pmatrix} 2 \frac{\partial u}{\partial x} - \frac{2}{3} \left(\frac{\partial u}{\partial x} + \frac{\partial v}{\partial y} \right) & \frac{\partial u}{\partial y} + \frac{\partial v}{\partial x} \\ \frac{\partial u}{\partial y} + \frac{\partial v}{\partial x} & 2 \frac{\partial v}{\partial y} - \frac{2}{3} \left(\frac{\partial u}{\partial x} + \frac{\partial v}{\partial y} \right) \end{pmatrix}.\tag{4.110}$$

The viscosity μ is assumed constant. For the pressure p , the Tait's law (3.50) or the linear pressure law (3.53) are suitable candidates. Both laws are tested in the numerical example described in Section 4.2.3. Writing the equations (4.106) in scalar form, we obtain the system

$$\frac{\partial \rho}{\partial t} = -\frac{\partial \rho u}{\partial x} - \frac{\partial \rho v}{\partial y}\tag{4.111}$$

$$\frac{\partial \rho u}{\partial t} = -\frac{\partial (\rho u^2 + p)}{\partial x} - \frac{\partial \rho u v}{\partial y} + \frac{\partial T_{E11}}{\partial x} + \frac{\partial T_{E12}}{\partial y}\tag{4.112}$$

$$\frac{\partial \rho v}{\partial t} = -\frac{\partial \rho u v}{\partial x} - \frac{\partial (\rho v^2 + p)}{\partial y} + \frac{\partial T_{E21}}{\partial x} + \frac{\partial T_{E22}}{\partial y}\tag{4.113}$$

All three equations (4.111) to (4.113) can be combined in a single generic equation

$$\frac{\partial \mathbf{U}}{\partial t} = \frac{\partial (-\mathbf{F}(\mathbf{U}) + \mathbf{t}_1(\mathbf{U}, \nabla \mathbf{U}))}{\partial x} + \frac{\partial (-\mathbf{G}(\mathbf{U}) + \mathbf{t}_2(\mathbf{U}, \nabla \mathbf{U}))}{\partial y}\tag{4.114}$$

by defining the vectors

$$\mathbf{U} = \begin{pmatrix} U_1 \\ U_2 \\ U_3 \end{pmatrix} = \begin{pmatrix} \rho \\ \rho u \\ \rho v \end{pmatrix}, \quad \mathbf{F}(\mathbf{U}) = \begin{pmatrix} \rho u \\ \rho u^2 + p \\ \rho u v \end{pmatrix}, \quad \mathbf{G}(\mathbf{U}) = \begin{pmatrix} \rho v \\ \rho u v \\ \rho v^2 + p \end{pmatrix},$$

$$\mathbf{t}_1(\mathbf{U}, \nabla \mathbf{U}) = \begin{pmatrix} 0 \\ T_{E_{11}} \\ T_{E_{21}} \end{pmatrix}, \quad \mathbf{t}_2(\mathbf{U}, \nabla \mathbf{U}) = \begin{pmatrix} 0 \\ T_{E_{12}} \\ T_{E_{22}} \end{pmatrix}. \quad (4.115)$$

For numerical implementation, we follow the approach outlined in [35] for the compressible Navier-Stokes equations of gas dynamics, with modifications to account for the assumption of constant temperature and weak compressibility. The information contained in the convective terms \mathbf{F} and \mathbf{G} have a preferred propagation direction given by the local speed of sound, while the viscous terms \mathbf{t}_1 and \mathbf{t}_2 are dissipative in nature and have no preferred propagation direction. Physically speaking, the convective terms correspond to an advection problem, where the solution is known along lines of characteristics (cf. Section 4.3), and hence it is straight forward to use an upwind flux for these terms. The viscous terms, however, are similar to the heat in a heat diffusion problem, and so they are discretized using a central flux. To avoid confusion, note that we do *not* solve for the *primitive* variables ρ , u and v , but for the *conserved* variables ρ , ρu , ρv instead, from which the primitive variables can be calculated.

For the discretization of equation (4.114), the mixed method outlined in Section 4.1.9 for the convection-diffusion equation is used, i.e. the spatial derivatives $\frac{\partial u}{\partial x}$, $\frac{\partial u}{\partial y}$, $\frac{\partial v}{\partial x}$ and $\frac{\partial v}{\partial y}$ arising in \mathbf{t}_1 and \mathbf{t}_2 are discretized first by using the standard dG and a central flux. The solutions are then used in the discretization of equation (4.114). The derivatives of the velocity components are however not discretized directly; instead, the derivatives of the conserved variables are discretized and the derivatives of the velocity components are calculated using the chain rule

$$\frac{\partial u_i}{\partial x_j} = \frac{1}{U_1} \left(\frac{\partial U_{i+1}}{\partial x_j} - \frac{U_{i+1}}{U_1} \frac{\partial U_1}{\partial x_j} \right), \quad i = 1, 2, \quad (4.116)$$

with $u_1 = u$ and $u_2 = v$. The equations to be discretized for the auxiliary variables \mathbf{q}_x , \mathbf{q}_y are

$$\mathbf{q}_x = \frac{\partial \mathbf{U}}{\partial x} = \frac{\partial}{\partial x} \begin{pmatrix} U_1 \\ U_2 \\ U_3 \end{pmatrix} \quad \text{and} \quad \mathbf{q}_y = \frac{\partial \mathbf{U}}{\partial y} = \frac{\partial}{\partial y} \begin{pmatrix} U_1 \\ U_2 \\ U_3 \end{pmatrix}. \quad (4.117)$$

For readability, let us go through the process for only one component of \mathbf{U} and drop the index. Then, the generic equations to be discretized are

$$q_x = \frac{\partial U}{\partial x} \quad \text{and} \quad q_y = \frac{\partial U}{\partial y}. \quad (4.118)$$

Using the approach outlined in Section 4.1 (integration by parts, use of Gauss' theorem and discretization), we arrive at the following discrete weak formulations:

$$\int_{D^{(k)}} (q_x)_h^{(k)} \ell_j^{(k)} d\mathbf{x} = - \int_{D^{(k)}} U_h^{(k)} \frac{\partial \ell_j^{(k)}}{\partial x} d\mathbf{x} + \int_{\partial D^{(k)}} U^* \ell_j^{(k)} \hat{n}_x d\mathbf{x}, \quad (4.119)$$

$$\int_{D^{(k)}} (q_y)_h^{(k)} \ell_j^{(k)} d\mathbf{x} = - \int_{D^{(k)}} U_h^{(k)} \frac{\partial \ell_j^{(k)}}{\partial y} d\mathbf{x} + \int_{\partial D^{(k)}} U^* \ell_j^{(k)} \hat{n}_y d\mathbf{x}. \quad (4.120)$$

Note that here, we do not integrate by parts twice, but instead, we implement the weak form directly. Using a central flux

$$U^* = \{\{U\}\} = \frac{U_{int} + U_{ext}}{2}, \quad (4.121)$$

expressing $q_h^{(k)}$ and $U_h^{(k)}$ in terms of the Lagrange polynomials,

$$q_h^{(k)} = \sum_i q_i^{(k)} \ell_i^{(k)}, \quad U_h^{(k)} = \sum_i U_i^{(k)} \ell_i^{(k)} \quad (4.122)$$

and expressing integrals of the Lagrange polynomials in terms of the mass and stiffness matrices $\mathbf{M}^{(k)}$, $\mathbf{S}_x^{(k)}$ and $\mathbf{S}_y^{(k)}$, we obtain

$$\mathbf{M}^{(k)}(\mathbf{q}_x)_h^{(k)} = -\mathbf{S}_x^{(k)} \mathbf{U}_h^{(k)} + \hat{\mathbf{n}}_x^{(k)} \boldsymbol{\xi} \mathbf{d}_U^{(k)}, \quad (4.123)$$

$$\mathbf{M}^{(k)}(\mathbf{q}_y)_h^{(k)} = -\mathbf{S}_y^{(k)} \mathbf{U}_h^{(k)} + \hat{\mathbf{n}}_y^{(k)} \boldsymbol{\xi} \mathbf{d}_U^{(k)}. \quad (4.124)$$

Here, $\hat{\mathbf{n}}_x^{(k)}$ and $\hat{\mathbf{n}}_y^{(k)}$ are the x - and y -components of the outward facing normal vector on an element face, and $\boldsymbol{\xi}$ and $\mathbf{d}_U^{(k)}$ were constructed in exact analogy to the 1-D case, see (4.40) and (4.41):

$$\boldsymbol{\xi} = \begin{pmatrix} \ell^{(k)}(\mathbf{x}_{f1}^{(k)}) & \ell^{(k)}(\mathbf{x}_{f2}^{(k)}) & \ell^{(k)}(\mathbf{x}_{f3}^{(k)}) \end{pmatrix}, \quad (4.125)$$

$$\mathbf{d}_U^{(k)} = \begin{pmatrix} U^*(\mathbf{x}_{f1}^{(k)}) \\ U^*(\mathbf{x}_{f2}^{(k)}) \\ U^*(\mathbf{x}_{f3}^{(k)}) \end{pmatrix}, \quad (4.126)$$

where the indices $f1$, $f2$ and $f3$ relate to the three faces of the triangular element. Now, multiplying by \mathbf{M}^{-1} and mapping from the physical to the reference triangle, we obtain

$$(\mathbf{q}_x)_h^{(k)} = -\frac{1}{J^{(k)}} \mathbf{D}_x \mathbf{U}_h^{(k)} + \frac{1}{J^{(k)}} \hat{\mathbf{n}}_x^{(k)} \Upsilon \mathbf{d}_U^{(k)}, \quad (4.127)$$

$$(\mathbf{q}_y)_h^{(k)} = -\frac{1}{J^{(k)}} \mathbf{D}_y \mathbf{U}_h^{(k)} + \frac{1}{J^{(k)}} \hat{\mathbf{n}}_y^{(k)} \Upsilon \mathbf{d}_U^{(k)}, \quad (4.128)$$

where the definition of the lift matrix Υ is identical to the 1-D case, see equation (4.45). At this point, the discretization of the expressions arising in \mathbf{t}_1 and \mathbf{t}_2 is known, and we can return to the discretization of (4.114). For better readability,

the discretization procedure will again be shown for one element U_i of (4.114), and without index. Defining the vector

$$\mathcal{F} = \begin{pmatrix} \mathcal{F}_1 \\ \mathcal{F}_2 \end{pmatrix} = \begin{pmatrix} -F(U) + t_1(U, \nabla U) \\ -G(U) + t_2(U, \nabla U) \end{pmatrix}, \quad (4.129)$$

equation (4.114) can be conceived as a divergence operation:

$$\frac{\partial U}{\partial t} = \text{div } \mathcal{F} = \frac{\partial \mathcal{F}_1}{\partial x} + \frac{\partial \mathcal{F}_2}{\partial y} \quad (4.130)$$

The weak form of the above equation reads

$$\int_{D^{(k)}} \frac{\partial U_h^{(k)}}{\partial t} \ell_j^{(k)} = - \int_{D^{(k)}} (\mathcal{F}_1)_h^{(k)} \frac{\partial \ell_j^{(k)}}{\partial x} - \int_{D^{(k)}} (\mathcal{F}_2)_h^{(k)} \frac{\partial \ell_j^{(k)}}{\partial y} + \int_{\partial D^{(k)}} (\hat{n}_x \mathcal{F}_1 + \hat{n}_y \mathcal{F}_2)^* \ell_j^{(k)}. \quad (4.131)$$

For the flux, we use the upwinding expression

$$(\hat{n}_x \mathcal{F}_1 + \hat{n}_y \mathcal{F}_2)^* = \hat{n}_x \{ \{ \mathcal{F}_1 \} \} + \hat{n}_y \{ \{ \mathcal{F}_2 \} \} + \frac{\lambda}{2} [[U]]. \quad (4.132)$$

Here, λ is a local maximum linearized acoustic wave speed. Physically, it is the maximum velocity that the information of the convective part of the equation can travel with. It corresponds to the advection speed a in the simple 1-D advection problem. In simple terms, λ is calculated as follows: Consider an element face. Calculate the expression in parentheses at that face and at the adjacent face of the neighboring element. Then, take the maximum of the two values. Do this for each face in the computational domain. In mathematical terms:

$$\lambda = \max \left\{ \left(|\mathbf{u}| + \sqrt{\frac{\partial p}{\partial \rho}} \right)_{\mathbf{U}_h^{int}}, \left(|\mathbf{u}| + \sqrt{\frac{\partial p}{\partial \rho}} \right)_{\mathbf{U}_h^{ext}} \right\}. \quad (4.133)$$

(4.133) results from applying the two-dimensional version of (4.57) to the system (4.114). The second term in (4.133) represents the speed of sound in the fluid, c , which in case of the linear pressure law (3.53) is a constant. Proceeding as usual by expressing $(\mathcal{F}_1)_h^{(k)}$, $(\mathcal{F}_2)_h^{(k)}$ and $U_h^{(k)}$ in terms of the Lagrange polynomials and expressing integrals of products of Lagrange polynomials and derivatives thereof in terms of the mass and stiffness matrices, we obtain

$$\mathbf{M}^{(k)} \frac{d\mathbf{U}_h^{(k)}}{dt} = -\mathbf{S}_x^{(k)} (\mathcal{F}_1)_h^{(k)} - \mathbf{S}_y^{(k)} (\mathcal{F}_2)_h^{(k)} + \boldsymbol{\xi} \left(\hat{\mathbf{n}}_x^{(k)} \mathbf{d}_{\mathcal{F}_1}^{(k)} + \hat{\mathbf{n}}_y^{(k)} \mathbf{d}_{\mathcal{F}_2}^{(k)} \right) \quad (4.134)$$

and finally

$$\frac{d\mathbf{U}_h^{(k)}}{dt} = -\frac{1}{J^{(k)}} \mathbf{D}_x^{(k)} (\mathcal{F}_1)_h^{(k)} - \frac{1}{J^{(k)}} \mathbf{D}_y^{(k)} (\mathcal{F}_2)_h^{(k)} + \frac{1}{J^{(k)}} \Upsilon \left(\hat{\mathbf{n}}_x^{(k)} \mathbf{d}_{\mathcal{F}_1}^{(k)} + \hat{\mathbf{n}}_y^{(k)} \mathbf{d}_{\mathcal{F}_2}^{(k)} \right). \quad (4.135)$$

Although the number of dimensions is two, and the number of unknowns is three and the flux functions are nonlinear, the expression (4.135) is still very similar to equation (4.70) in the advection case. The matrices \mathcal{F}_1 and \mathcal{F}_2 contain the flux functions and are element-local, while the connection between the elements is established by the matrices $\mathbf{d}_{\mathcal{F}_1}$ and $\mathbf{d}_{\mathcal{F}_2}$.

4.2.3 Example: Driven Cavity

The so-called Lid-Driven Cavity problem has become a standard problem in Computational Fluid Dynamics and is widely used to benchmark results and efficiency of codes for the solution of the incompressible Navier-Stokes equations, see e.g [27, 32]. The test case consists of a two-dimensional, square domain with no-slip boundary conditions on all four sidewalls. Three sidewalls have zero velocity, while the top boundary (the "lid") has non-zero velocity. The boundary conditions are sketched in Figure 4.5, which also shows the mesh that was used in our simulations. Due to the lid being moved in tangential direction, one main vortex develops in the middle of the cavity, and two smaller vortices in the lower left and right corners. At small Reynolds numbers ($Re < 1$), the flow is fully symmetric and dominated by viscous forces. At higher Reynolds numbers, convective forces become more important, and the center of the main vortex moves up and to the right, while the two corner vortices grow in size. Streamlines are now asymmetric. At moderate to high Reynolds numbers ($Re > 1000$), additional vortices develop in the lower two corners, and in the upper left corner.

The standard benchmark paper for Driven Cavity flow is by Ghia et al. [32]. Erturk et al. [27] collected and compared data from numerous contributions on this flow configuration. Both papers provide streamline plots of the cavity flow, and tabulated values for vertical velocities along a horizontal line and for horizontal velocities along a vertical line through the center of the cavity.

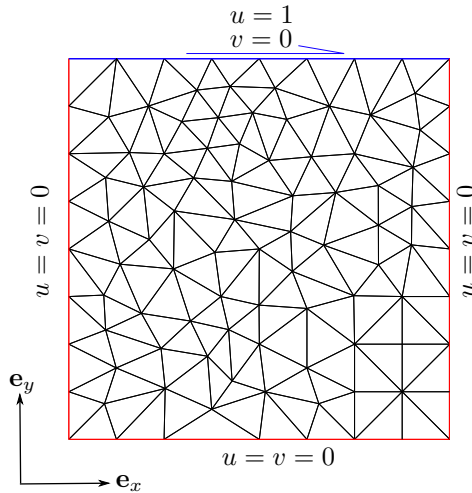


Figure 4.5: Mesh and boundary conditions for Driven Cavity problem. The mesh consists of $K = 165$ elements, and the order of approximation is $N = 6$.

Here, the Driven Cavity problem is simulated employing a weakly compressible fluid as described in section 4.2.2. In the limit of infinite fluid bulk modulus (i.e. zero compressibility), however, the solution of the compressible Navier-Stokes equations for the Driven Cavity flow converges to the incompressible solution. It is concluded that as long as the density perturbations are relatively low, the Driven Cavity problem is a suitable benchmark for the dG numerical approximation of the weakly compressible Navier-Stokes equations outlined in this chapter. Moreover, the test case can be used to assess the performance of the different pressure laws for problems with relatively

small pressure perturbations; i.e. to answer the question if the simple linear law (3.53) can be used instead of the more complex expression (3.50). Here, the Driven Cavity flow is simulated for a Reynolds number of $Re = 1000$, a Mach number $Ma = u_{lid}/c = 0.032$ with u_{lid} the velocity of the upper wall and $c = 31.6$ m/s the speed of sound in the fluid.

The two streamline plots in Figure 4.6, showing the streamlines computed with the 2-D code presented in Section 4.2 using the linear pressure law (3.53) and the Tait's law (3.50) for the computation of the fluid pressure, are virtually indistinguishable, and are in excellent qualitative agreement with the results presented by Ghia et al. [32] and Erturk et al. [27]. Figure 4.7 shows the x - and y - velocity profiles along a vertical and a horizontal line through the cavity center, respectively. The data using both pressure laws coincide exactly, and hence are not shown separately. The agreement with the benchmark solution [32] is excellent.

We conclude that the present code performs well in reproducing benchmark results, and that for low Mach numbers and density perturbations, a simple linear law for the fluid pressure is sufficient.

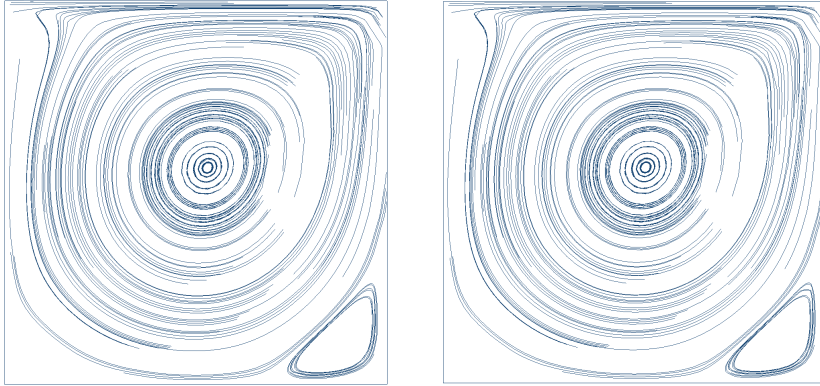


Figure 4.6: Streamline plots for Lid-Driven Cavity flow of a weakly compressible fluid for $Re = 1000$, computed using the dG method. Left: Results obtained using the linear pressure law (3.53); right: using the Tait's law (3.50) for the fluid pressure.

4.3 Open boundary conditions for the compressible Navier-Stokes equations

In numerical problems involving compressible media, and hence acoustic wave propagation, a classical problem is the treatment of boundaries where the flow field can freely enter or leave the domain. Conventional Dirichlet or Neumann boundary conditions lead to reflections of acoustic waves at the domain boundary. The problem emerges when a domain of interest is cut out from a larger physical domain for numerical computation, when the complete domain is too large to be simulated. A simple example is water flow in a pipe: To numerically investigate some subdomain of interest, the flow field at the inlet and at the outlet of that subdomain must be prescribed as boundary conditions. A whole scientific field has emerged around this problem; and depending on the author and approach, the boundary condition is

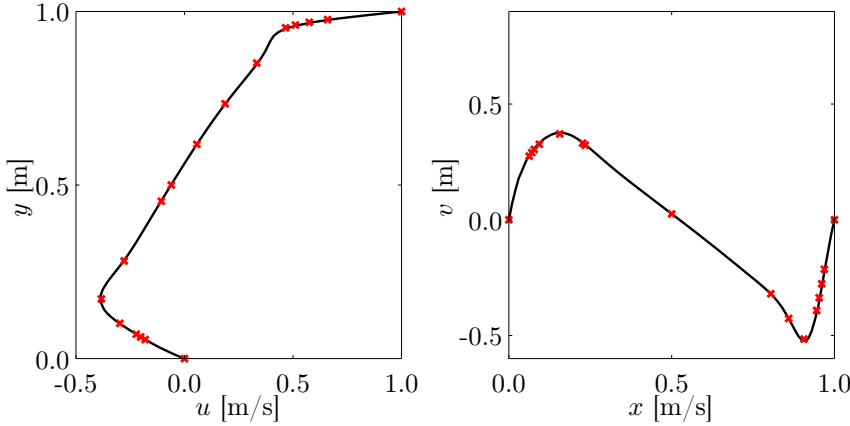


Figure 4.7: Left: Horizontal velocity profile along a vertical line through the center of the cavity. Right: Vertical velocity profile along a horizontal line through the center of the cavity. Solid line shows results computed with the present code; red crosses are benchmark results from [32]. The results obtained using the linear law (3.53) and the Tait's law (3.50) coincide exactly.

called *non-reflecting*, *artificial*, *absorbing*, *natural*, *open* or *transparent*. Hereinafter, we will use to the term *open boundary condition*.

The necessity of open boundary conditions is obvious for flows involving in- or outlets, e.g. the flow presented in Chapter 2, where a vessel is emptied at the bottom, and the discharged volume is replaced by air from the top boundary. But also for apparently simpler conditions like the batch sedimentation problem presented in Chapter 5, such boundary conditions are necessary to acoustic waves to leave the domain via some boundary instead of being reflected.

One apparently widely used way of treatment for such boundaries is the technique of *Perfectly Matched Layers* (see e.g. [37]). The method amounts to an addition of a layer to the domain boundary in question, in which the physical equations are tweaked in such a way that oscillations arising from acoustic waves are damped out, while the overall flow field is affected only to a minimum. Another, somewhat similar idea is to add a layer in which artificial viscosity is added to the equations wherever sharp gradients in the solution variables occur - which is the case in the vicinity of acoustic wavefronts (see [48] for a very nice implementation of viscous shock capturing in a nodal dG framework). Both approaches have the disadvantage that additional computational cells must be created at the open domain boundary which are not necessary for the computation of the solution, but increase the computational cost.

In the present thesis we followed the approach proposed by Feistauer et al. [28], which relies on a characteristic based method. The principal idea is to prescribe a set of conditions just outside the domain boundary that match the physical conditions arising from the simulation just inside the boundary in such a way that acoustic waves are canceled out when the solution from the computation interacts with the boundary condition.

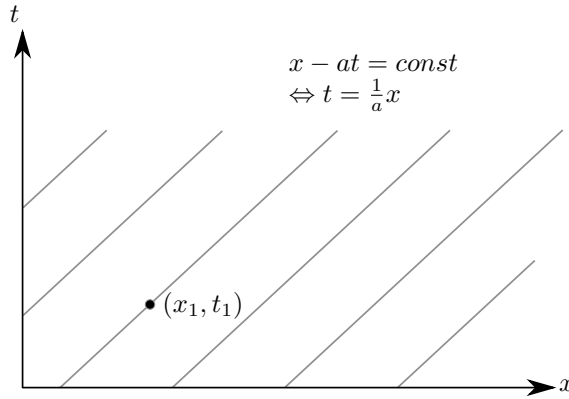


Figure 4.8: Illustration of the characteristic lines for equation (4.136) with $a > 0$. Once a solution is known for a specific space-time point (x_1, t_1) , the solution is also known for all other points along the characteristic line.

To understand the idea behind the open boundary condition proposed by [28], let us consider the simple 1-D advection equation

$$\frac{\partial u}{\partial t} + a \frac{\partial u}{\partial x} = 0 \quad (4.136)$$

with $a = \text{const.}$ The general solution of this equation is $u(x, t) = f(x - at)$. It follows that $u = \text{const}$ along the straight lines $x - at = \text{const}$ in the x, t -plane, see Figure 4.8. Once a solution is known for a specific time t_1 and a specific point x_1 , then the solution is known for all (x, t) pairs along the characteristic line that passes through that point, with a determining the slope of the line. This behavior is easily understood from the physics of the advection equation: if $u(x_1, t_1)$ denotes a concentration, then this concentration value is advectively transported through the domain at velocity a . Now, let us assume that equation (4.136) holds in a domain stretching from $x = L$ on the left to $x = R$ on the right, and that $a > 0$. Clearly, if the initial values $u(x, 0)$ within the domain $[L, R]$ are known and a boundary condition $u(L, t)$ at the left boundary is prescribed for $t > 0$, the solution u is completely determined at any $x \in [L, R]$ and $t > 0$. (If, on the other hand, $a < 0$, the advective transport is from right to left, so that boundary condition must be given at the right domain boundary $x = R$.) Next, let us assume that (4.136) holds for $x \in \mathbb{R}$, that is, in an infinite domain, and we want to solve (4.136) numerically. Of course, for a numerical calculation, we must specify some computational spatial domain $x \in [l, r]$. Then, we prescribe the initial data

$$u(x, 0) = u_0(x), \quad x \in [l, r]. \quad (4.137)$$

We recall that (4.136) holds in an infinite domain, while the computational domain is necessarily bounded. For $a > 0$, We prescribe the boundary condition on the left boundary

$$u(0, t) = u^*(t), \quad (4.138)$$

with u^* a "guessed" value for the solution u at $x < l$, $x \approx l$. The value u^* is called *far-field solution*, and (4.138) is a so-called *open boundary condition*.

Generalizing the simple advection example, consider the linear system of equations:

$$\frac{\partial \mathbf{u}}{\partial t} + \mathbf{A} \frac{\partial \mathbf{u}}{\partial x} = \mathbf{0} \quad (4.139)$$

with \mathbf{u} the vector of unknowns and a constant coefficient matrix \mathbf{A} containing the information on the characteristics of the problem. If \mathbf{A} is diagonalizable, which we assume here, such a system is called hyperbolic. We write \mathbf{A} as

$$\mathbf{A} = \mathbf{C} \mathbf{D} \mathbf{C}^{-1}, \quad (4.140)$$

where the columns of matrix \mathbf{C}^* contain the eigenvectors of \mathbf{A} and the diagonal matrix \mathbf{D} contains the eigenvalues $\lambda_1^* \dots \lambda_n^*$ of \mathbf{A} :

$$\mathbf{D} = \begin{pmatrix} \lambda_1 & & 0 \\ & \ddots & \\ 0 & & \lambda_n \end{pmatrix} \quad (4.141)$$

We insert (4.140) into (4.139) and multiply by \mathbf{C}^{-1} from the left:

$$\mathbf{C}^{-1} \frac{\partial \mathbf{u}}{\partial t} + \mathbf{D} \mathbf{C}^{-1} \frac{\partial \mathbf{u}}{\partial x} = \mathbf{0}. \quad (4.142)$$

\mathbf{C}^{-1} contains only constant values and can be written inside the spatial and temporal derivatives. Defining $\mathbf{v} = \mathbf{C}^{-1} \mathbf{u}$, (4.142) can finally be written as

$$\frac{\partial \mathbf{v}}{\partial t} + \mathbf{D} \frac{\partial \mathbf{v}}{\partial x} = \mathbf{0}, \quad (4.143)$$

corresponding to a decoupled system of equations,

$$\begin{aligned} \frac{\partial v_1}{\partial t} + \lambda_1 \frac{\partial v_1}{\partial x_1} &= 0, \\ &\vdots \\ \frac{\partial v_i}{\partial t} + \lambda_i \frac{\partial v_i}{\partial x_i} &= 0, \\ &\vdots \\ \frac{\partial v_n}{\partial t} + \lambda_n \frac{\partial v_n}{\partial x_n} &= 0. \end{aligned} \quad (4.144)$$

Each of the equations (4.144) has the form (4.136), for which the general solution is known to be constant along the characteristics (cf. Figure 4.8), with the slopes determined by the eigenvalues.

To this point, equation (4.143) is not restricted to any computational domain, i.e. the domain is infinite, and no boundary and initial conditions are imposed. Now, as in case of the advection equation (4.136), let us say that (4.139) holds for $x \in \mathbb{R}$, $t > 0$, and the computational spatial domain is $[l, r]$. From the discussion related to (4.136), it is clear that the solutions $v_1, \dots, v_i, \dots, v_n$ of the equations displayed in (4.144) are uniquely determined (and consequently, the solution \mathbf{u} of (4.139)), if the initial data

$$v_1(x, 0), \dots, v_i(x, 0), \dots, v_n(x, 0), \quad x \in [l, r] \quad (4.145)$$

and the *open boundary conditions*

$$\begin{aligned} v_i(l, t) &= v_i^*(t), & \text{if } \lambda_i > 0, \\ v_i(r, t) &= v_i^*(t), & \text{if } \lambda_i < 0 \end{aligned} \quad (4.146)$$

are prescribed. Since $\mathbf{v} = \mathbf{C}^{-1}\mathbf{u}$, (4.146) are conditions on \mathbf{u} at $x = l$ and/or $x = r$, expressed in terms of a far-field solution $\mathbf{u}^* = \mathbf{C}\mathbf{v}^*$, and depending whether the characteristics enter ($\lambda_i > 0$) or leave ($\lambda_i < 0$) the computational domain. In order to allow acoustic waves to travel out of the domain without reflection, the boundary conditions $v_i = v_i^*$ must be enforced for all i for which the characteristic lines point *into* the domain. Remember the slope of the characteristic lines is given by λ_i , so that the direction of the characteristics for a given boundary is known.

We shall now apply the approach outlined above to the 2-D weakly compressible Navier-Stokes equations, following Feistauer et al. [28]. First, equation (4.114) is rewritten as

$$\frac{\partial \mathbf{U}}{\partial t} + \frac{\partial \mathbf{F}(\mathbf{U})}{\partial x} + \frac{\partial \mathbf{G}(\mathbf{U})}{\partial y} = \mathbf{R}(\mathbf{U}, \nabla \mathbf{U}, \nabla^2 \mathbf{U}), \quad (4.147)$$

where the hyperbolic part of the equations was put on the left-hand side, and the viscous terms were lumped to the right-hand side using the definition

$$\mathbf{R}(\mathbf{U}, \nabla \mathbf{U}, \nabla^2 \mathbf{U}) = \frac{\partial \mathbf{t}_1(\mathbf{U}, \nabla \mathbf{U})}{\partial x} + \frac{\partial \mathbf{t}_2(\mathbf{U}, \nabla \mathbf{U})}{\partial y}. \quad (4.148)$$

Furthermore, equation (4.147) can be rewritten as

$$\frac{\partial \mathbf{U}}{\partial t} + \text{grad}_{\mathbf{U}} \mathbf{F}(\mathbf{U}) \frac{\partial \mathbf{U}}{\partial x} + \text{grad}_{\mathbf{U}} \mathbf{G}(\mathbf{U}) \frac{\partial \mathbf{U}}{\partial y} = \mathbf{R}(\mathbf{U}, \nabla \mathbf{U}, \nabla^2 \mathbf{U}). \quad (4.149)$$

Defining the matrices

$$\mathbf{A}_1(\mathbf{U}) = \text{grad}_{\mathbf{U}} \mathbf{F}(\mathbf{U}), \quad \mathbf{A}_2(\mathbf{U}) = \text{grad}_{\mathbf{U}} \mathbf{G}(\mathbf{U}), \quad (4.150)$$

(4.149) takes the form

$$\frac{\partial \mathbf{U}}{\partial t} + \mathbf{A}_1(\mathbf{U}) \frac{\partial \mathbf{U}}{\partial x} + \mathbf{A}_2(\mathbf{U}) \frac{\partial \mathbf{U}}{\partial y} = \mathbf{R}(\mathbf{U}, \nabla \mathbf{U}, \nabla^2 \mathbf{U}). \quad (4.151)$$

The information on the characteristic waves is contained in the matrix $\mathbf{A} = n_x \mathbf{A}_1 + n_y \mathbf{A}_2$ with $\hat{\mathbf{n}} = [n_x \ n_y]^T$ the normal vector on a boundary. The convective part of the the system (4.151), i.e. the left-hand side of (4.149) is of hyperbolic type if \mathbf{A} is diagonalizable. The eigenvalues are obtained by solving $\det \mathbf{A} - \lambda \mathbf{I}$ for λ . The result is

$$\lambda_1 = \mathbf{v} \cdot \hat{\mathbf{n}} - c, \quad \lambda_2 = \mathbf{v} \cdot \hat{\mathbf{n}}, \quad \lambda_3 = \mathbf{v} \cdot \hat{\mathbf{n}} + c, \quad (4.152)$$

where c is the speed of sound in the fluid, showing that the convective part of (4.151) is indeed hyperbolic. This result is useful in the formulation of the open boundary conditions. In the following, we need the eigenvectors of \mathbf{A} , which are obtained by solving the system

$$\mathbf{A}\mathbf{c} = \lambda_1 \mathbf{c}, \quad \mathbf{A}\mathbf{c} = \lambda_2 \mathbf{c}, \quad \mathbf{A}\mathbf{c} = \lambda_3 \mathbf{c} \quad (4.153)$$

for $\mathbf{c} \neq 0$. Three non-zero \mathbf{c} 's, say \mathbf{c}_1 , \mathbf{c}_2 , \mathbf{c}_3 , solutions of (4.153), are written as the columns of a matrix denoted by $\mathbf{C}(\mathbf{U}, \hat{\mathbf{n}})$:

$$\mathbf{C}(\mathbf{U}, \hat{\mathbf{n}}) = [\mathbf{c}_1(\mathbf{U}, \hat{\mathbf{n}}), \quad \mathbf{c}_2(\mathbf{U}, \hat{\mathbf{n}}), \quad \mathbf{c}_3(\mathbf{U}, \hat{\mathbf{n}})]. \quad (4.154)$$

We recall that \mathbf{A} depends on both \mathbf{U} and $\hat{\mathbf{n}}$, which explains the dependence of the matrix \mathbf{C} on \mathbf{U} and $\hat{\mathbf{n}}$. We have

$$\mathbf{C} = \begin{pmatrix} 1 & 0 & 1 \\ un_x + vn_y - c & 0 & un_x + vn_y + c \\ vn_x + un_y & 1 & vn_x + un_y \end{pmatrix}, \quad (4.155)$$

and inverting,

$$\mathbf{C}^{-1} = \begin{pmatrix} \frac{un_x + vn_y + c}{2c} & -\frac{1}{2c} & 0 \\ -vn_x - un_y & 0 & 1 \\ -\frac{un_x + vn_y - c}{2c} & \frac{1}{2c} & 0 \end{pmatrix}. \quad (4.156)$$

All necessary ingredients for the application of open boundary conditions have now been derived. To see how the boundary conditions are applied, let us assume that we want to simulate a horizontal pipe flow, i.e. the domain stretches from $x = L$ to $x = R$, and open boundary conditions will be applied at both boundaries $x = L$ to $x = R$, see Figure 4.9. To do this, we linearize the convective part

$$\frac{\partial \mathbf{U}}{\partial t} + \mathbf{A}_1(\mathbf{U}) \frac{\partial \mathbf{U}}{\partial x} \quad (4.157)$$

in equation (4.151) around a state \mathbf{U}^* ,

$$\frac{\partial \mathbf{U}}{\partial t} + \mathbf{A}_1(\mathbf{U}^*) \frac{\partial \mathbf{U}}{\partial x} \quad (4.158)$$

where \mathbf{U}^* is a far-field solution (one for the inlet and one for the outlet). Neglecting all but the linearized convective part (4.158), (4.151) becomes

$$\frac{\partial \mathbf{U}}{\partial t} + \mathbf{A}_1(\mathbf{U}^*) \frac{\partial \mathbf{U}}{\partial x} = 0, \quad (4.159)$$

which is a linear hyperbolic system analogous to (4.139). The eigenvalues λ_1^* , λ_2^* and λ_3^* of $\mathbf{A}_1(\mathbf{U}^*)$ and the matrix $\mathbf{C}(\mathbf{U}^*, \hat{\mathbf{n}})$ containing the eigenvectors \mathbf{c}_1^* , \mathbf{c}_2^* and \mathbf{c}_3^* of $\mathbf{A}(\mathbf{U}^*)$ can directly be obtained from (4.152) and (4.155) by taking $\hat{n}_x = 1$ and $\hat{n}_y = 0$ for a unit vector in x -direction, so that

$$\lambda_1^* = u^* - c^*, \quad \lambda_2^* = u^*, \quad \lambda_3^* = u^* + c^*. \quad (4.160)$$

From (4.156), we obtain

$$\mathbf{C}^{*-1} = \begin{pmatrix} \frac{u^* + c^*}{2c^*} & -\frac{1}{2c^*} & 0 \\ -v^* & 0 & 1 \\ -\frac{u^* - c^*}{2c^*} & \frac{1}{2c^*} & 0 \end{pmatrix}. \quad (4.161)$$

For subsonic flow conditions, the characteristics corresponding to λ_2^* and λ_3^* point into the domain at $x = L$ and the characteristic corresponding to λ_1^* points into the domain at $x = R$, see Figure 4.9.

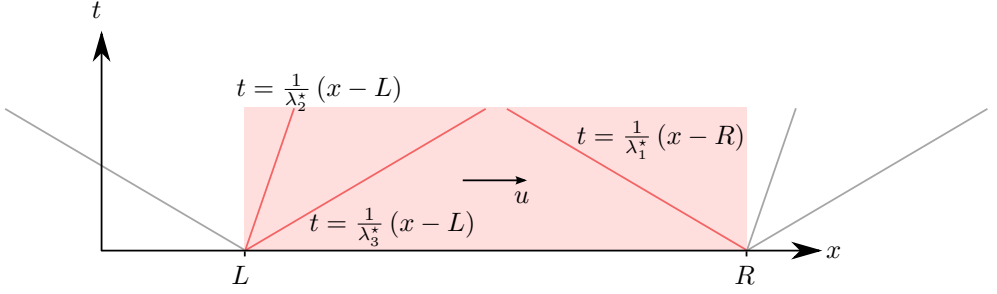


Figure 4.9: Illustration of characteristics entering a horizontal channel. We assume $\lambda_2^* = u^* > 0$ and subsonic flow conditions, so that $u^* < c^*$ and $\lambda_1^* = u^* - c^* < 0$ and $\lambda_3^* = u^* + c^* > 0$.

According to the discussion referring to (4.139), the boundary conditions at $x = L$ and $x = R$ must be given in terms of the variable $\mathbf{V} = \mathbf{C}^{*-1}\mathbf{U}$, and they are

$$\begin{aligned} V_2 &= V_2^*, & V_3 &= V_3^* & \text{at } x = L, \\ V_1 &= V_1^* & & & \text{at } x = R. \end{aligned} \quad (4.162)$$

Using $\mathbf{V} = \mathbf{C}^{*-1}\mathbf{U}$ and expression (4.161) of \mathbf{C}^{*-1} , this leads to

$$v = v^* \quad (4.163)$$

$$\rho u = \rho^* c^* + (u^* + c^*)\rho \quad (4.164)$$

at the left boundary, $x = L$ and

$$\rho u = -\rho^* c^* + (u^* - c^*)\rho \quad (4.165)$$

at the right boundary, $x = R$. The next section is concerned with a numerical example where these boundary conditions are applied.

4.3.1 Example: Flow of a weakly compressible fluid past a triangular cylinder

A widely-used 2-D CFD benchmark for unsteady flow is the channel flow past one or several objects placed in the mean flow slightly off the centerline. At low Reynolds numbers $Re < Re_c$, two stationary vortices evolve behind the obstacle. At higher Reynolds numbers, $Re > Re_c$, an instability known as the Bénard- von Kármán instability develops, and the vortices on either side are periodically detached from the rear of the obstacle. Here, Re_c is a critical Reynolds number that depends on the actual configuration of the channel and the obstacle. The flow has been investigated for a multitude of objects (e.g. circles, triangles, squares, see [31, 35, 60]) and pressure drop, lift and drag coefficients were computed for comparison. Here, however, the pattern of the fully developed flow is only of secondary importance. Our main interest concerns the question if the acoustic waves emerging from the impulsively started inlet boundary condition can freely leave the domain via the outlet, and, after being scattered by the obstacle, also via the inlet; and the vortex flow configuration appears to be a good test case.

The flow was simulated using the weakly compressible Navier-Stokes equations under isothermal conditions, as described in Section 4.2.2, with a fluid viscosity of $\mu = 0.001$

Pas. For the computation of the fluid pressure, the linear pressure law 3.53 was used assuming a sound velocity $c = 31.6$ m/s and fluid reference density $\rho_{ref} = 1$ kg/m³. The boundary conditions are given by equations (4.163) to (4.165), and the prescribed far-field states are

$$u^* = \frac{6y(y_{max} - y)}{y_{max}^2}, \quad v^* = 0, \quad \rho^* = \rho_{ref} \quad (4.166)$$

at the inlet boundary, and

$$u^* = 0, \quad \rho^* = \rho_{ref} \quad (4.167)$$

at the outlet boundary, respectively (cf. Figure 4.10). Here, $y_{max} = 0.41$ m is the height of the geometry. The unknown fields ρ, u, v are initialized by prescribing $u = v = 0$ and $\rho_0 = \rho_{ref}$. The far-field velocity at the outlet was assumed to be zero because the exact velocity distribution at the outlet is not known a priori, and some value must be prescribed. Another possibility is to give u^* at the outlet such that the mass flows at inlet and outlet coincide exactly.

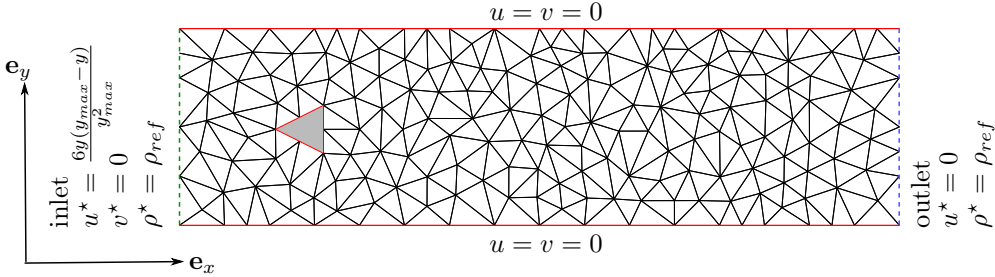


Figure 4.10: Mesh and boundary conditions for the flow past a triangular cylinder. The domain length and height are 1.5 and 0.41 m, respectively. The triangle tip is aligned at 0.2 m from the left and bottom boundaries; and the length in both x - and y - direction is 0.1 m. The mesh consists of $K = 330$ elements, and the order of approximation is $N = 4$.

Let us now come to the results of the computations. Shortly after the onset of flow, the acoustic wave is reflected at the triangle back towards the inlet and the side walls (cf. Figure 4.11). At the side walls, the wave is reflected again and travels back towards the middle of the domain, while the wave going back to the inlet can leave the channel. The measured velocity of the wavefront, as expected, is identical to the speed of sound prescribed by the constitutive relation for the fluid pressure. The acoustic wave leaves the domain through the outlet (cf. Figure 4.12). Note that wavefronts do not only leave the domain if they are aligned with the outlet, but also if they are tilted. Yet, the fraction of the waves traveling in y - direction is further reflected at the side walls and is retained in the channel for a considerable amount of time, until it is damped out by viscosity. Later, when the flow is fully developed, the famous pattern of the Karman vortex street is clearly visible (cf. Figures 4.13 and 4.14). The vortical flow structures are smeared out near the outlet as a consequence of the far-field velocity at the outlet being prescribed as zero along the whole boundary. The prescribed far-field states do not assure that mass flow at inlet and outlet coincide. Nevertheless, there is no density increase throughout the computation; instead, the maximum velocity at the inlet, which is prescribed as $u_{max,in}^* = 1.5$ m/s, adjusts to ≈ 1 m/s, while at the outlet, a velocity of $u_{out} \approx 0.5$ m/s everywhere along the outlet boundary is observed.

The resulting Reynolds number of the flow is $Re \approx 100$. This behavior reveals a feature of the used boundary condition that can be an advantage or a disadvantage, depending on the initial boundary value problem to be investigated: On the one hand, it is advantageous that the boundary condition is very indulgent to changes in the flow evolving inside the domain. On the other hand, it is disadvantageous that pressure and/or velocity at the boundary cannot be given precisely, but only as far-field conditions. Moreover, it is not possible to let the solution values on the boundary at each time step evolve freely, which would correspond to a free outflow. Some approximate, "guessed" values for both the far-field velocity and pressure must be prescribed. Regarding the flow in Chapter 2, this requirement might pose problems, because the flow and hence the velocity and pressure at the boundary are driven by gravity, and not known a priori. In case of the Karman vortex flow presented here, the situation is slightly better, because the mass flow at the outlet can be prescribed to match the mass flow at the inlet; however, as we are only prescribing far-field values, the actual solution values at the boundary may not coincide at all times with the prescribed far-field values. Both mentioned flow processes are mainly *transport* processes, but due to the compressible nature of the fluid, also include *acoustic* phenomena. Summarizing, the open boundary conditions introduced by [28] have been proven to handle acoustic wave phenomena extremely well; however, the precise prescription of mass flow rates in transport problems is somewhat difficult due to the prescription of far-field states instead of precise boundary conditions.

4.4 Numerical implementation of the hybrid model

The numerical implementation of the hybrid model presented in Chapter 3 is described in this section. The approach presented in Section 4.2.2 for the compressible Navier-Stokes equations is relatively generic, and only few adjustments must be made.

The hybrid model can be written as follows:

$$\frac{\partial \mathbf{U}}{\partial t} = \frac{\partial (-\mathbf{F}(\mathbf{U}) + \mathbf{t}_1(\mathbf{U}, \nabla \mathbf{U}))}{\partial x} + \frac{\partial (-\mathbf{G}(\mathbf{U}, \nabla \mathbf{U}) + \mathbf{t}_2(\mathbf{U}, \nabla \mathbf{U}))}{\partial y} + \mathbf{Z}(\mathbf{U}, \nabla \mathbf{U}), \quad (4.168)$$

where

$$\begin{aligned} \mathbf{U} = \begin{pmatrix} U_1 \\ U_2 \\ U_3 \\ U_4 \\ U_5 \\ U_6 \end{pmatrix} &= \begin{pmatrix} \rho^f \\ \rho^f u_f \\ \rho^f v_f \\ \rho^s \\ \rho^s u_s \\ \rho^s v_s \end{pmatrix}, \quad \mathbf{F}(\mathbf{U}) = \begin{pmatrix} \rho^f u_f \\ \rho^f u_f^2 + p^f \\ \rho^f u_f v_f \\ \rho^s u_s \\ \rho^s u_s^2 + p^s \\ \rho^s u_s v_s \end{pmatrix}, \quad \mathbf{G}(\mathbf{U}) = \begin{pmatrix} \rho^f v_f \\ \rho^f u_f v_f \\ \rho^f v_f^2 + p^f \\ \rho^s v_s \\ \rho^s u_s v_s \\ \rho^s v_s^2 + p^s \end{pmatrix}, \\ \mathbf{t}_1(\mathbf{U}, \nabla \mathbf{U}) &= \begin{pmatrix} 0 \\ T_{E11}^f \\ T_{E21}^f \\ 0 \\ T_{E11}^s \\ T_{E21}^s \end{pmatrix}, \quad \mathbf{t}_2(\mathbf{U}, \nabla \mathbf{U}) = \begin{pmatrix} 0 \\ T_{E12}^f \\ T_{E22}^f \\ 0 \\ T_{E12}^s \\ T_{E22}^s \end{pmatrix}, \quad \mathbf{Z}(\mathbf{U}, \nabla \mathbf{U}) = \begin{pmatrix} 0 \\ -\hat{s}_x^s \\ -\hat{s}_y^s - \rho^f g \\ 0 \\ +\hat{s}_x^s \\ +\hat{s}_y^s - \rho^s g \end{pmatrix} \end{aligned} \quad (4.169)$$

Equation (4.168) is identical to equation (4.114), except that the number of components is doubled, and except for the term $\mathbf{Z}(\mathbf{U}, \nabla \mathbf{U})$, which contains the momentum exchange term and gravity. The terms in $\mathbf{Z}(\mathbf{U}, \nabla \mathbf{U})$ are known explicitly, and hence do not have to be discretized. The remaining part of the equations is discretized exactly as equation (4.114), i.e. the velocity gradients in $\mathbf{t}_1(\mathbf{U}, \nabla \mathbf{U})$ and $\mathbf{t}_2(\mathbf{U}, \nabla \mathbf{U})$ are calculated via a generic weak gradient operation applied to the conserved variables using a central flux and applying the chain rule; and after that the remaining terms are discretized using a dG generic weak gradient operation and a local Lax-Friedrichs upwind flux, cf. Section 4.2.2.

One point deserving special attention when implementing the hybrid model is the application of open boundary conditions. The complication arising here is related to the equilibrium part of the momentum exchange term $\hat{\mathbf{s}}_{eq}^\alpha$, equation (3.60), because it contains a first spatial derivative of a solution variable, and must be considered in the derivation of the eigenvalues and eigenvectors of the system (4.168); i.e. $\hat{\mathbf{s}}_{eq}^\alpha$ would have to be attributed to $\mathbf{F}(\mathbf{U})$ and $\mathbf{G}(\mathbf{U})$ rather than $\mathbf{Z}(\mathbf{U}, \nabla \mathbf{U})$ before diagonalizing $\text{grad}_{\mathbf{U}} \mathbf{F}(\mathbf{U})$ and $\text{grad}_{\mathbf{U}} \mathbf{G}(\mathbf{U})$. In this case, the diagonalization of the system matrix is not only difficult to calculate; it is even unclear if the convective part of the system is still hyperbolic, which is a prerequisite for the application of the open boundary conditions according to [28]. The hyperbolicity then depends very much on the chosen pressure laws. The application of open boundary conditions is a major issue when using of the hybrid model to flows similar to the granular-water mixture flow described in Chapter 2, because that example involves mass flow across domain boundaries, and moreover, acoustic waves being reflected at the domain boundaries could potentially destroy the solution. For the batch sedimentation simulations described in the following chapter, the open boundary conditions are only needed at the top boundary. To circumvent the problems described above, it was assumed that $\text{grad } n^s$ is only different from zero at a sufficient distance from the top boundary. For batch sedimentation, this assumption is realistic, because the solid volume fraction at the top boundary tends to zero very shortly after the beginning of the simulation. This way, the equilibrium exchange term does not have to be considered in the diagonalization; i.e. $\hat{\mathbf{s}}_{eq}^\alpha$ can be treated as a right-hand side as in equation (4.168). Note, however, that for more general problems, in which the solid volume fraction near an open boundary is different from zero, the use of open boundary conditions as described in Section 4.3 may be problematic or even impossible. In case of batch sedimentation, the eigenvalues are given by

$$\begin{aligned}\lambda_1 &= \mathbf{v}_f \cdot \hat{\mathbf{n}} - c_f, \\ \lambda_2 &= \mathbf{v}_f \cdot \hat{\mathbf{n}}, \\ \lambda_3 &= \mathbf{v}_f \cdot \hat{\mathbf{n}} + c_f, \\ \lambda_4 &= \mathbf{v}_s \cdot \hat{\mathbf{n}} - c_s, \\ \lambda_5 &= \mathbf{v}_s \cdot \hat{\mathbf{n}}, \\ \lambda_6 &= \mathbf{v}_s \cdot \hat{\mathbf{n}} + c_s,\end{aligned}\tag{4.170}$$

and the resulting boundary conditions are exactly the same for both solid and fluid as they are for the fluid in the single-fluid case.

The other point deserving special interest is the linearized acoustic wave speed λ used in the expression (4.133) for the upwind flux. In principle, (4.133) translates seamlessly to the mixture case as:

$$\lambda = \max \left\{ \left(|\mathbf{u}_f| + \sqrt{\frac{\partial p^f}{\partial \rho^f}} \right)_{\mathbf{U}_h^{int}}, \left(|\mathbf{u}_f| + \sqrt{\frac{\partial p^f}{\partial \rho^f}} \right)_{\mathbf{U}_h^{ext}}, \right. \\ \left. \left(|\mathbf{u}_s| + \sqrt{\frac{\partial p^s}{\partial \rho^s}} \right)_{\mathbf{U}_h^{int}}, \left(|\mathbf{u}_s| + \sqrt{\frac{\partial p^s}{\partial \rho^s}} \right)_{\mathbf{U}_h^{ext}} \right\}. \quad (4.171)$$

However, note that p^s consists of a contribution from the true fluid pressure and the configuration pressure, cf. (3.55). The expression (3.56) of the configuration pressure makes it relatively difficult to evaluate the derivative $\partial p^s / \partial \rho^s$; moreover, the result is singular for $n^s \rightarrow n_{max}^s$. As a pragmatic solution, the following expression was used in the numerical calculations:

$$\lambda = \max \left\{ \left(|\mathbf{u}_f| + \sqrt{\frac{\partial n^f p^{fR}}{\partial \rho^f}} \right)_{\mathbf{U}_h^{int}}, \left(|\mathbf{u}_f| + \sqrt{\frac{\partial n^f p^{fR}}{\partial \rho^f}} \right)_{\mathbf{U}_h^{ext}}, \right. \\ \left. \left(|\mathbf{u}_s| + \sqrt{\frac{\partial n^s p^{fR}}{\partial \rho^s}} \right)_{\mathbf{U}_h^{int}}, \left(|\mathbf{u}_s| + \sqrt{\frac{\partial n^s p^{fR}}{\partial \rho^s}} \right)_{\mathbf{U}_h^{ext}} \right\}. \quad (4.172)$$

4.5 Time integration

Up to this point, all equations that were presented in this chapter have only been discretized in space; in space-time, they are semi-discrete. For time integration, the explicit Runge-Kutta methods presented in [35] proved to be simple and robust for the problems discussed here, and hence were used without any modification. An advantage of the hybrid model is the fact that simple, explicit time integration schemes can be used instead of more expensive implicit time stepping procedures that are necessary for incompressible models. The main disadvantage of a model involving a compressible fluid with high bulk modulus is the existence of fast acoustic waves that must be resolved by the numerical scheme. In particular, the time step is calculated by

$$\Delta t = 0.5 \left[\frac{N^2}{h} \left(\lambda + \frac{N^2}{h} \mu \right) \right]^{-1}, \quad (4.173)$$

see [35], where h is the inscribed circle of the smallest mesh element and λ is the maximum linearized acoustic wave speed (4.133). (4.173) represents the requirement that no quantity may flow further than the distance between two vertices within one timestep. The term $\lambda \frac{N^2}{h}$ in (4.173) represents this requirement for the convective part of the equations and is known as the Courant-Friedrichs-Lewy (CFL) condition; while the term $\lambda + \frac{N^4}{h^2} \mu$ represents a similar requirement for the parabolic part of the equations. In the practical numerical simulations presented here, it turned out that the CFL condition was more restrictive.

The hybrid model allows the investigation of both acoustic wave propagation and

mass transport. For the types of flow investigated in this thesis, however, the acoustic wave velocity is much larger than the bulk flow velocity, thereby dramatically decreasing the time step size compared to incompressible models and hence, increasing the computational cost. As long as the propagation of acoustic waves is of interest, this may not be a restriction; however, if the focus is on the bulk flow, the restriction is immense. Yet, there are several ways to alleviate the problem. One possibility is to use implicit time integration. Luo et al. [60] have shown that the benefit of an implicit time integration scheme can reduce the computation times by a factor of ≈ 10 compared to an explicit Runge-Kutta method using a staggered grid in a discontinuous Galerkin framework, but the programming effort and knowledge required for implementation is relatively high. Another alternative concerns the type of hardware used for numerical solution of the model equations. The computational cost of the nodal discontinuous Galerkin method used in this thesis, as discussed in this chapter, results mainly from matrix-matrix multiplications. This type of operation is known to be extremely well parallelizable, and during the recent years, the use of graphics processing units (GPUs) has emerged in scientific computing that handle this task - parallel calculation of floating point operations - extremely well. Klöckner et al. [47] report speedups of a factor of up to 60 on a single, moderately-priced GPU compared to a single CPU for a nodal discontinuous Galerkin scheme. Full three-dimensional simulations of weakly compressible mixture flows might be feasible at least for flows on the laboratory scale and on time scales of several seconds using a dG implementation of the hybrid model on GPUs. A third way to reduce the problem of small time steps lies in the fluid's bulk modulus. Depending on the type of flow, the influence of fluid compressibility on the overall flow process might only be significant in specific, rather dynamic flow situations (cf. Chapter 5). On the other hand, in situations when the flow is rather stationary, the flow pattern is not dramatically influenced by the fact that the fluid is compressible. This observation immediately suggests to increase time step size by decreasing the fluid bulk modulus and consequently, the acoustic wave velocity. This method that is quite common in the Smoothed Particle Hydrodynamics (SPH) numerical frameworks, cf. [7, 63, 76]. However, the fluid bulk modulus should be adjusted such that the Mach number $Ma = |\mathbf{u}|_{max}/c < 0.1$, see [63].

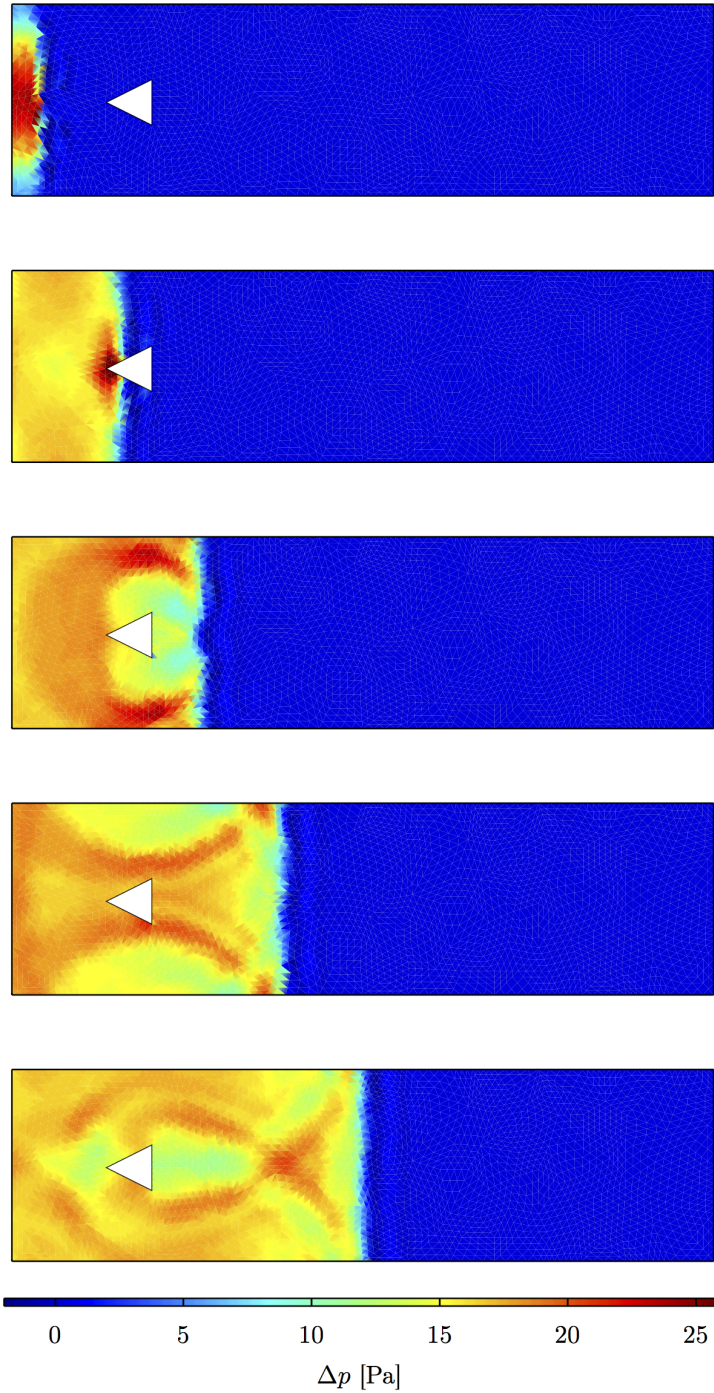


Figure 4.11: Results from the simulation of the flow of a weakly compressible fluid around a triangular obstacle. Colours indicate pressure distribution at five equidistant times from $t = 1.8$ ms to $t = 23.5$ ms after start of the simulation. Note how the acoustic wave is scattered by the obstacle and partly reflected back towards and leaving the domain at the inlet.

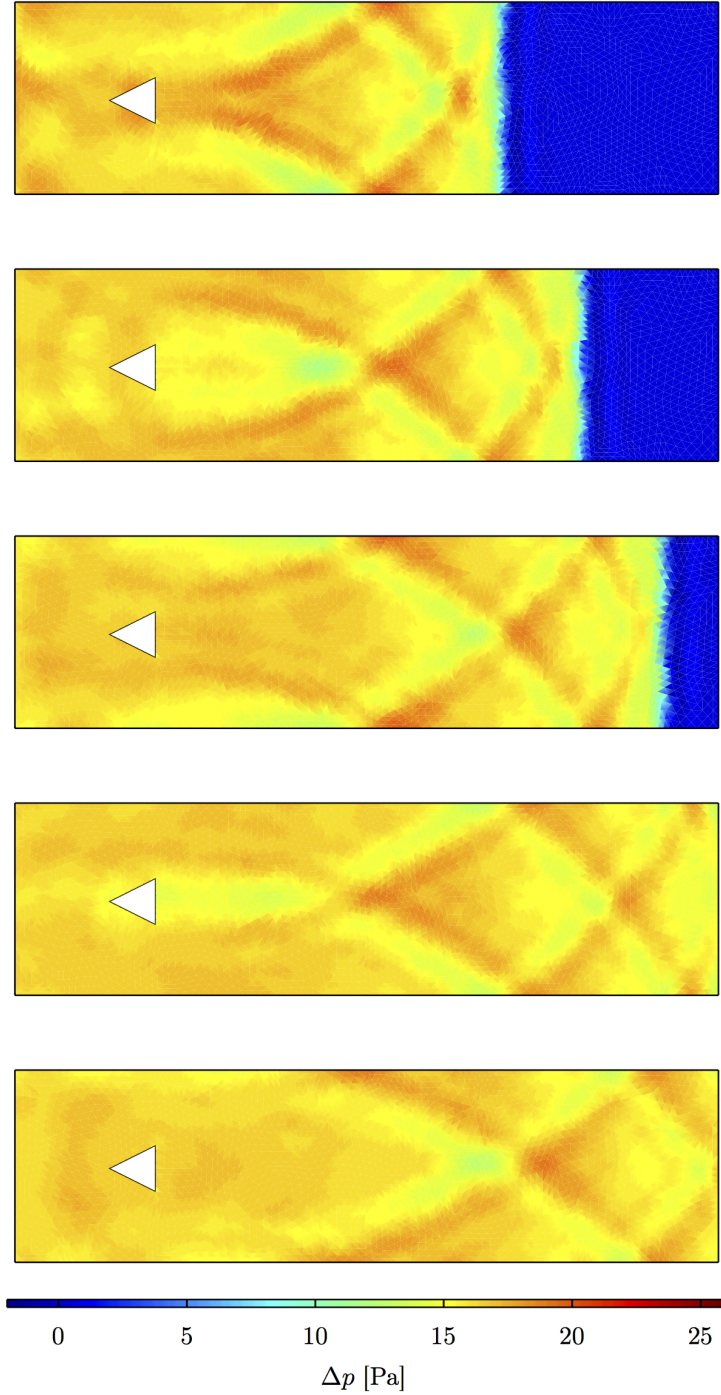


Figure 4.12: Results from the simulation of the flow of a weakly compressible fluid around a triangular obstacle. Colours indicate pressure distribution at five equidistant times from $t = 32.6$ ms to $t = 54.4$ ms after start of the simulation. Acoustic waves can freely leave the domain at the outlet, but are reflected at the upper and lower side walls.

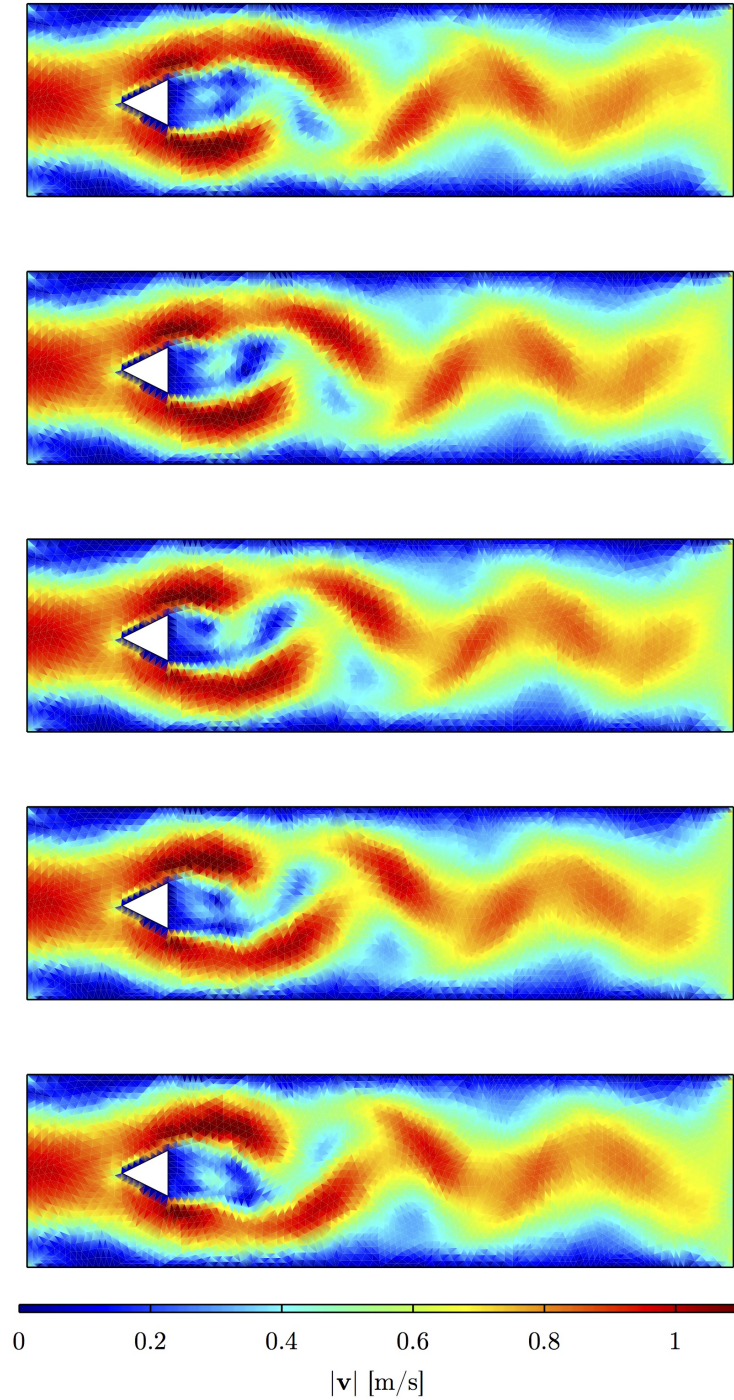


Figure 4.13: Results from the simulation of the flow of a weakly compressible fluid around a triangular obstacle. Colours indicate velocity magnitude at five equidistant times from $t = 6.0$ s to $t = 6.4$ s. The Karman vortex street is now fully developed. Even complex flow structures can leave the domain at the outlet.

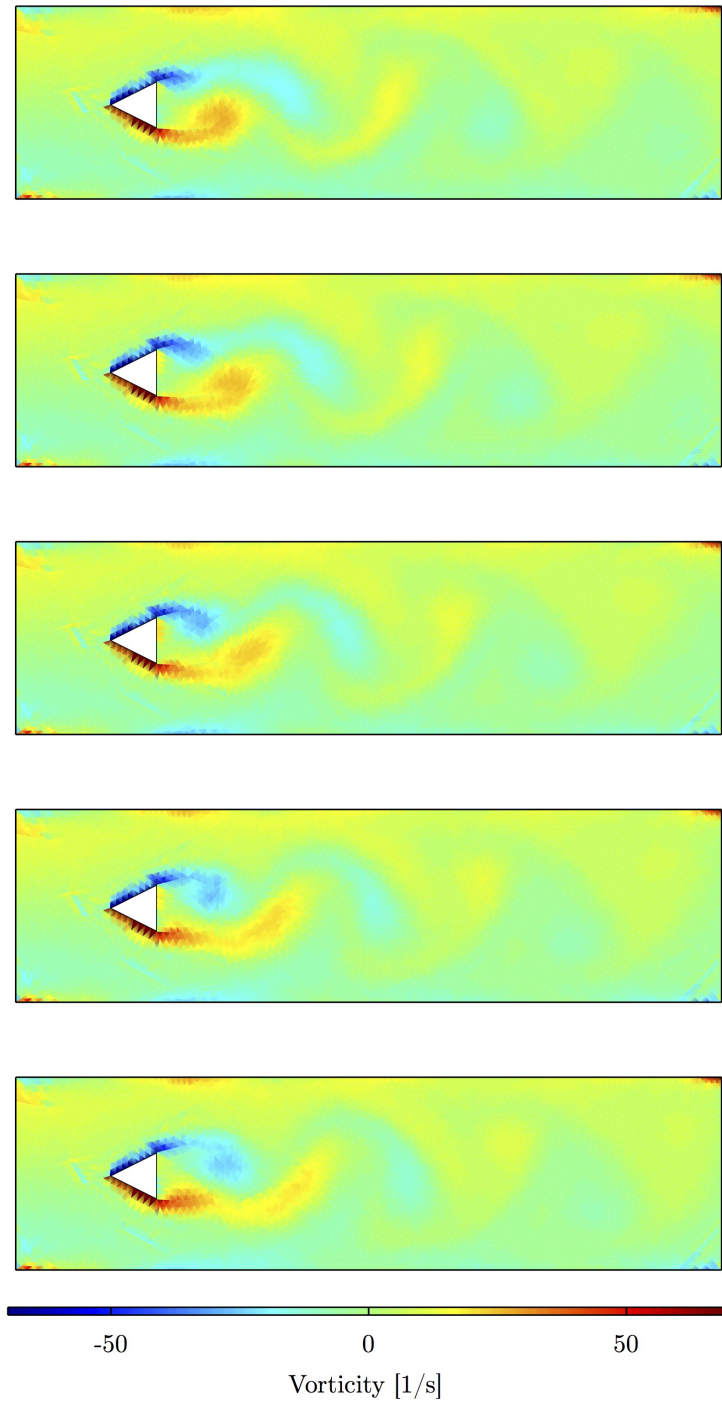


Figure 4.14: Results from the simulation of the flow of a weakly compressible fluid around a triangular obstacle. Colours indicate vorticity magnitude at five equidistant times from $t = 6.0$ s to $t = 6.4$ s.

Chapter 5

Simulations of batch sedimentation

5.1 Initial boundary value problem

We simulate the batch sedimentation of a monodisperse suspension of spheres in a vertical column. Our two-dimensional mesh consists of $K = 128$ triangular elements in z -direction and only one element in x -direction, so that the simulations are quasi-one-dimensional, cf. Figure 5.1. However, the use of a two-dimensional mesh and triangular elements guarantee straightforward extensibility to more complex geometries. No flux boundary conditions are used at the side walls, that is, the horizontal velocities u_f , u_s are put to zero, while a Neumann boundary condition $\frac{\partial w_f}{\partial x} = \frac{\partial w_s}{\partial x} = 0$ for the vertical velocities assures that w_f , w_s are allowed to evolve freely near the wall. Physically, this condition corresponds to sedimentation in a horizontally infinitely extended domain. At the bottom, zero velocity is prescribed for both phases. At the top, open boundary conditions (cf. Sections 4.3, 4.4) are used, i.e. the fluid domain is cut off at the top, but acoustic waves and material transport over the boundary are possible. The computations to obtain the open boundary conditions are analogous to those in Section 4.3 starting after equation (4.156) for two boundaries in x -direction. The only difference is that here, the boundary in question is in z -direction. The boundary conditions are the same for both solid and fluid phase, cf. the discussion in Section 4.4:

$$\rho^f w_f = -\rho^{f*} c^* + (w_f^* + c^*) \rho^f \quad (5.1)$$

$$\rho^s w_s = -\rho^{s*} c^* + (w_s^* + c^*) \rho^s \quad (5.2)$$

We prescribe zero far-field velocity w_f^* , w_s^* for both phases and far-field densities $\rho^{f*} = n^f \rho_{ref}^f$, where $\rho_{ref}^f = 1000 \text{ kg/m}^3$ is a reference density for the weakly compressible fluid phase, and $\rho^{s*} = n^s \rho^{sR}$, where $\rho^{sR} = 2600 \text{ kg/m}^3$ is the constant true density of the incompressible solid. In terms of the true fluid pressure, these boundary conditions correspond to prescribing p^{fR*} equal to the initial pressure p_0^{fR} at the top boundary. At $t = 0$ the volume fraction of grains is distributed homogeneously throughout the domain, and the true fluid pressure $p^{fR}(t_0) = \rho^{fR}(t_0)gz$ corresponds to the pressure in a quiescent fluid under the influence of gravity. We are interested in

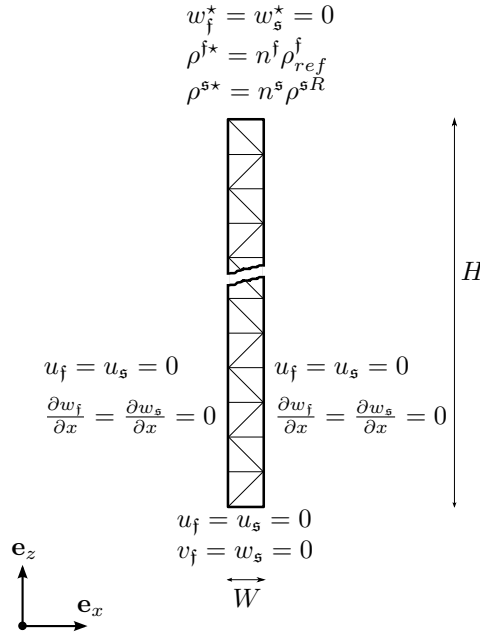


Figure 5.1: Mesh and boundary conditions for batch sedimentation simulations. Dimensions are $H = 0.5\text{m}$ and $W = 0.005\text{m}$.

- (a) the additional physical effects that can be observed in the simulation due to the weak compressibility of the fluid, which are not captured by fully incompressible models;
- (b) validating our results quantitatively by comparing the settling velocities within the homogeneous suspension layer at steady state sedimentation obtained in the simulation with the settling velocities calculated using the theory of Ishii & Zuber [42];
- (c) a better understanding of the sedimentation process by analyzing the role of single terms in the balance equations in the different layers and at different times; and
- (d) the influence of varying the model parameters given in Table 5.1, in order to understand their impact on the sedimentation process.

parameter	$n_{max,\mu}^s$ [-]	Θ^s [-]	K_0^f [Pa]	d [m]	n_0^s [-]
basic setting	0.68	0.02	10^5	0.001	0.3
variation	0.64	0.012	10^6	0.0002	0.58
	0.72	0.016	10^7		0.1

Table 5.1: Values used for parameter study in batch sedimentation simulations

Table 5.1 contains a *basic setting* box and a *variation* box. This means that the following analyses are related to the basic setting parameters. Then, to study the influence of a change in one of the listed parameters, all parameters were kept as in

the basic setting, except the parameter of interest. The parameters $n_{max,\mu}^s$ and Θ^s are parameters that emerge in the constitutive modeling process from the necessity to obtain a specific desired behavior of the model. They may be changed to accomodate a specific behavior e.g. observed in an experiment, but have no physical significance. The parameters d and n_0^s are real, physical parameters of the sedimentation process, and are varied simply in order to validate the model not only for one, but several different parameter sets. The bulk modulus of the fluid, K_0^f , can be attributed to both groups, because it can be a non-physical parameter in cases where the true compressibility of the fluid is not important for the solution of the boundary value problem - in that case, one would set K_0^f to a lower than the physical value in order to increase the time step size. For problems where the fluid compressibility is important, and compressibility effects and the velocity of acoustic waves are to be captured correctly, K_0^f can be seen as a physical parameter. The values of K_0^f in Table 5.1 are far below the bulk modulus of water, for which $K_0^f = 2.2 \cdot 10^9$ Pa. Nevertheless, in a real-world application, a value of $K_0^f = 10^7$ Pa might not be unrealistic for the fluid compressibility, because water - except if evacuated - usually contains entrained air bubbles. The bulk modulus of a liquid-air mixture is given as

$$K_0^f = \frac{K_0^{liquid}}{1 + n^{air} \left(\frac{K_0^{liquid}}{K_0^{air}} - 1 \right)}, \quad (5.3)$$

see [52, equation 8.38]. Realizing that $K_0^{water}/K_0^{air} \gg 1$ and assuming an air content of 1%, a fluid bulk modulus of $K_0^f = 10^7$ Pa is obtained. Hence, for the results evaluation, it must be kept in mind that the basic setting of the fluid bulk modulus was set to a physically too low value in order to achieve a more efficient computation.

5.2 Results and discussion

5.2.1 Overview and phenomenology of a batch sedimentation process

Let us first analyze the different intrinsic time scales of the problem, using the basic settings in Table 5.1. To do this, it is illustrative to investigate the time rate of change in the volume fraction of solid, integrated over the domain, versus time (see Figure 5.2, left panel). Four different time scales can be identified, each of them reflecting unique processes. During the first period, Δt_1 , the initially homogeneously distributed grains start to sink and the three typical batch sedimentation layers develop (see Figure 5.2, right panel): clear fluid at the top (Zone I), homogeneous suspension with $n^s = n_0^s$ in the middle (Zone II), and a sedimented bed (Zone III) at the bottom. During the development of the three layers, the time rate of change in solid volume fraction is necessarily instationary. At the beginning of the second period Δt_2 , the layers are fully developed, and the flow is stationary in the sense that the two interfaces (clear fluid / suspension; and suspension / sedimented bed, identified by the horizontal portions of the curves in Figure 5.2, right panel) approach each other at constant velocities. The time rate of change of solid volume fraction is almost zero at each nodal point within each of the three layers and non-zero at the nodal points near the interfaces. As the shape of the interfaces does not change (stationary flow), the time rate of change of solid volume fraction is constant. This period is described by the phenomenological theory of Kynch [51]. In the third period Δt_3 of the simulation,

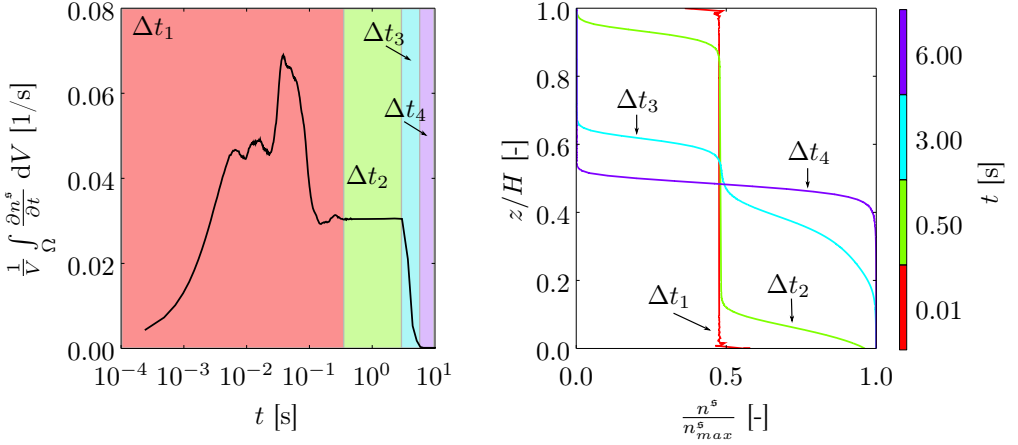


Figure 5.2: Left: Temporal evolution of the volume integral of the time rate of change of solid volume fraction. Note the four different time scales, reflecting dynamic onset of flow, stationary sedimentation, merging of the two interfaces and full sedimentation. Right: Solid volume fraction vs. column height. Each curve depicts one point in time within of the time periods depicted in the left panel.

the two interfaces merge, and the time rate of change of solid volume fraction decays and reaches zero when all particles are fully settled at the beginning of Δt_4 .

5.2.2 Dynamic effects during batch sedimentation

Even in a relatively simple problem setup as batch sedimentation, the hybrid model reveals dynamic processes on a short timescale ($\Delta t_1 \approx 0.1$ s) and non-dynamic processes on longer timescales ($\Delta t_{2,3} \approx 1...10$ s). In Figure 5.2, oscillations in the time rate of change of solid volume fraction are observed during Δt_1 .

To interpret the oscillations, we analyze Figure 5.3, showing the evolution of solid and fluid phase velocities, and the fluid excess pore pressure $\Delta p^{fR} = p^{fR} - \rho^{fR}gz - p_{atm}$. The excess pore pressure is the part of the true fluid pressure that emerges solely due to the sedimentation process, that is, without considering the hydrostatic portion of the fluid pressure and the atmospheric pressure. Equal line colors belong to one specific time for all three plots, so that the instantaneous interactions between the three variables can be analyzed. At the beginning of the simulation, the solid grains start to sink down due to gravity (orange, yellow and light green colors, 0 to 16.6 ms); the solid phase velocity increases. In a fully incompressible setting, mass conservation would yield the necessity of an immediate upward flux of fluid compensating for the downward flux of solid. Here, however, the fluid compressibility leads to a delay in this upward fluid flux; instantaneously, the fluid flux is even directed *downwards*. To understand this, imagine what happens when the simulation starts: Instantaneously, the fluid is dragged downwards by the solid phase due to momentum interaction (drag), leading to an excess pore pressure decrease at the top and increase at the bottom of the domain (lower left plot in Figure 5.3); and hence to an increased pressure gradient. The increase in pressure gradient is more notable in the lower part of the domain, due to the $w_f = w_s = 0$ bottom boundary condition. As the simulation goes on, the pressure gradient increases further, and with it, the fluid phase velocity reaches its minimum (turquoise, 23.4 ms) and then

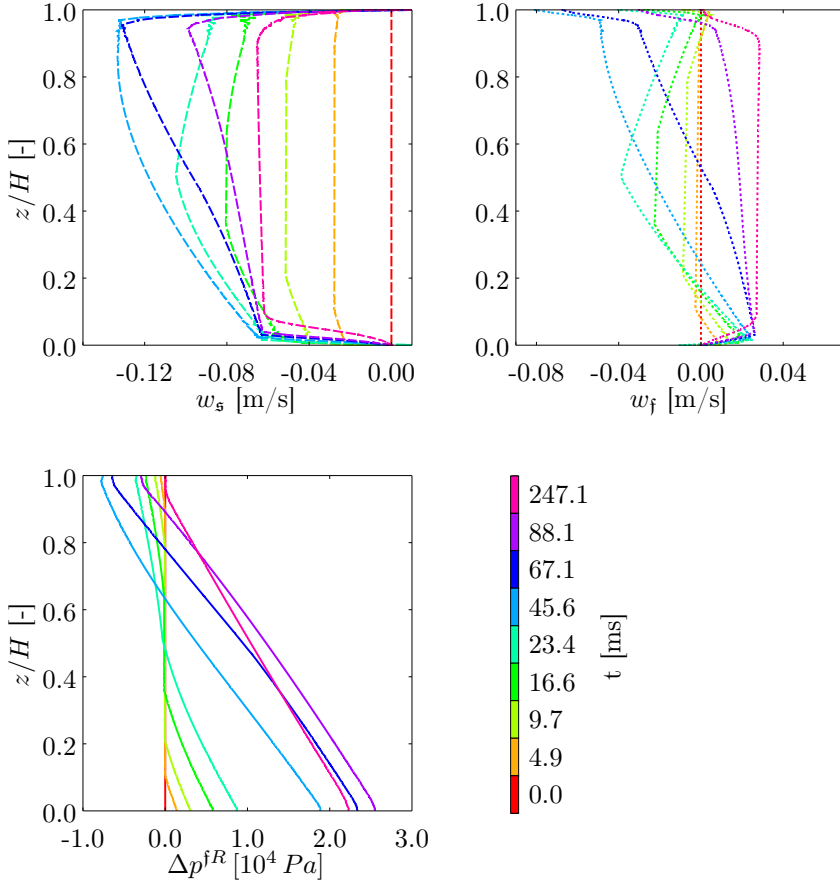


Figure 5.3: Solid velocity (upper left), fluid velocity (upper right) and excess pore pressure $\Delta p^{fR} = p^{fR} - \rho^{fR}gz - p_{atm}$ during the dynamic part of the simulation. Colorbar indicates the time for all three plots. Note that the times are non-equidistant.

starts to increase (light blue, 45.6 ms). The excess pore pressure gradient is now high enough to serve as a driving force for *upward* fluid flow. The solid phase velocity reaches its minimum when the fluid phase velocity has already started to increase again. Due to drag, the solid phase velocity now starts to increase along with the fluid velocity (blue, 67.1 ms) and both velocities reach a steady state within Zone II (the homogeneous suspension area, pink, 247.1 s). The excess pore pressure gradient is almost constant from 45.6 s onwards; only the position of the excess pressure curve shifts to the right to accommodate for the open boundary condition $p^{fR*} = p_0^{fR}$.

In a fully incompressible setting, the upward mass flow of fluid would instantaneously compensate for downward solid flux because due to the incompressibility constraint, a fluid density increase is not allowed. In a compressible setting, however, downward mass flow of solid leads to downward mass flow of fluid, in turn leading to a fluid pressure gradient, which then serves as a driving force for upward fluid

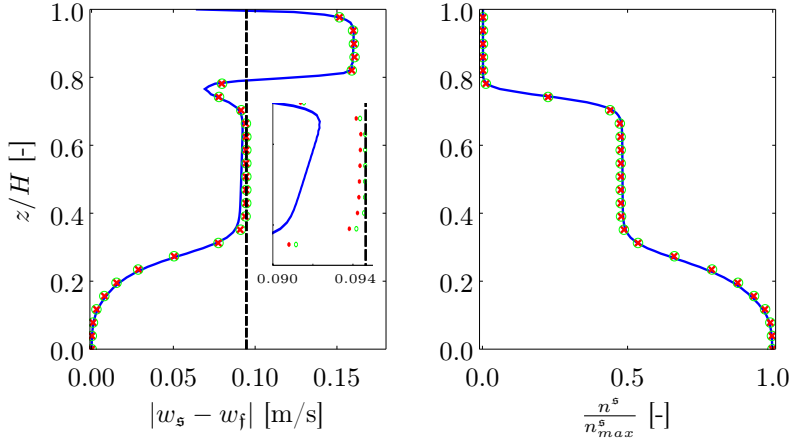


Figure 5.4: Left: Settling velocity vs. column height at $t = 2$ s for several bulk moduli, compared to analytic solution (5.7) (dashed black line). Inset shows a magnification of Zone II. Right: Solid volume fraction versus column height. Solid blue line: $K_0^f = 10^5$ Pa, red crosses: $K_0^f = 10^6$ Pa, green circles: $K_0^f = 10^7$ Pa.

mass flow. The dynamic processes described here have not yet been reported in the literature, probably because they act on a very short timescale, and may not be of great significance for real-world applications. Here, the discussion was conducted to prove the ability of the hybrid model to capture both mass transport *and* acoustic effects in conjunction with boundary conditions that allow acoustic waves to leave the computational domain. However, in a real sedimentation process, the fluid is also necessarily compressible, so we can assume that these processes are realistic. Note that in the above analysis we have assumed a very high fluid compressibility. If realistic compressibilities are assumed for the fluid, the effects shown here are less notable, but still visible. The description of these effects is made possible by using a hybrid model.

When the typical three layers of clear fluid, sedimenting grains and sediment bed are fully developed, the temporal changes in solid volume fraction become stationary at the end of Δt_1 . The new, higher pressure gradient is then the driving force for a constant upward fluid flow during Δt_2 .

5.2.3 Quantitative validation of simulation results

At the beginning of Δt_2 , the system has adjusted to a stationary state, where the driving force of gravity is in equilibrium with drag and pressure gradient and dynamic effects are negligible. Note that $\Delta t_1 \ll \Delta t_2$, cf. Figure 5.2, left panel. During Δt_2 , the three typical layers of clear fluid, sedimenting grains and sediment bed are fully developed, and the interfaces between the layers approach each other as kinematic waves, as the theory of Kynch [51] predicts.

So far, we have seen effects due to the fluid compressibility during the first period Δt_1 , but of course the model must be able to also correctly capture the physics during the stationary period Δt_2 . Ishii & Zuber [42] have derived an analytic solution for the settling velocity of spherical particles on the basis of their theory, and have verified

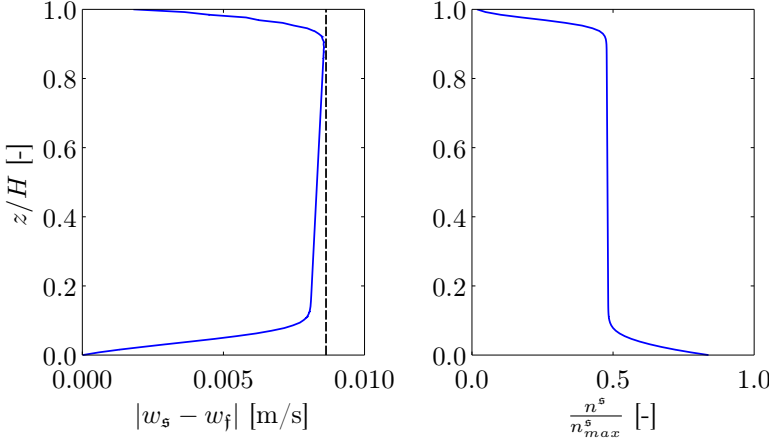


Figure 5.5: Left: Settling velocity vs. column height at $t = 2$ s for $d = 0.002$ mm, compared to analytic solution (5.7) (dashed black line). Right: Solid volume fraction versus column height.

their results against a range of experiments with relative success. Their equation can be used to verify the performance of the hybrid model. Let us now go through the derivation of their analytical solution. We start from the assumption that during Δt_2 , the flow in Zone II is essentially one-dimensional in z -direction with only gravity, pressure gradients and momentum interaction as driving forces. The momentum balance for solid can then be written as

$$0 = -n^s \frac{\partial p^m}{\partial z} - n^s \rho^{sR} g + \hat{s}^s. \quad (5.4)$$

Here it was assumed that the mixture pressure $p^m = p^{fR} = p^{sR}$. In the framework of the hybrid model presented in Chapter 3, the same assumption is made within Zone II, where $p_{conf}^s = 0$ due to relatively large distances between particles, cf. equations (3.49) and (3.55). Adding the two momentum equations, and using equation (3.32), we obtain for the mixture pressure gradient:

$$n^s \frac{\partial p^m}{\partial z} = -\rho g, \quad (5.5)$$

so that, exploiting (3.68) and (3.63), equation (5.4) becomes

$$0 = n^s \rho g - n^s \rho^{sR} g + \frac{3}{4} \frac{C_D \rho^{fR} |w_s - w_f|^2}{d}, \quad (5.6)$$

which, using $\rho = \rho^f + \rho^s$ and $n^s = 1 - n^f$, can be solved for the settling velocity:

$$|w_s - w_f|^2 = (1 - n^s) \frac{4}{3} \frac{\rho^{fR} - \rho^{sR} d}{C_D \rho^{fR}} g. \quad (5.7)$$

We may now compare the simulation results for a range of physical parameters to the analytical result (5.7).

Figures 5.4 to 5.7 show a comparison between simulated settling velocities and the analytic solution (5.7) at time $t = 2$ s using different fluid compressibilities, grain sizes and initial solid volume fractions as listed in Table 5.1. Interestingly, plots of settling

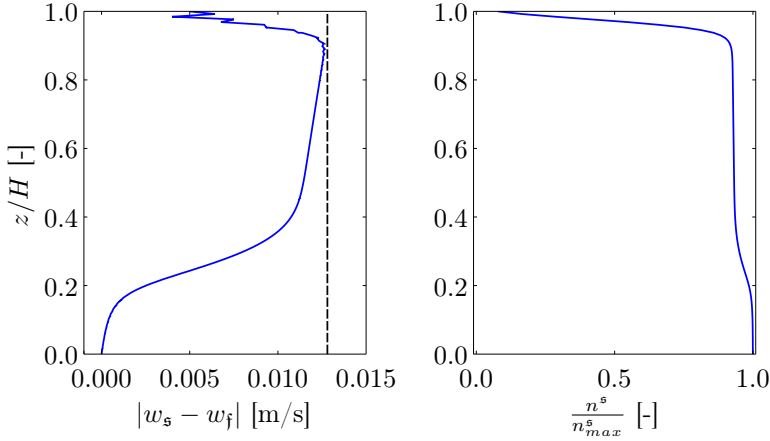


Figure 5.6: Left: Settling velocity vs. column height at $t = 2$ s for $n_0^s = 0.58$, compared to analytic solution (5.7) (dashed black line). Right: Solid volume fraction versus column height.

velocity versus height of column are rarely found in the literature, apparently due to the fact that simulations of batch sedimentation are commonly based on variants of Kynch's theory [51], and the information on the individual phase velocities at any location within the geometry is lost in that framework. We start with Figure 5.4, showing the settling velocities for a range of fluid bulk moduli. Of course, the numerical solution is expected to agree with the analytical solution only within Zone II. At the bottom, in Zone III, the velocities decrease because of two effects: First, the solid volume fraction increases and hence, also the drag. Second, as the volume fraction approaches maximum packing, the solid configuration pressure sets in and stops further compaction of the grains. In Zone I, the settling velocity increases because the solid volume fraction decreases. At the top boundary, the settling velocity tends to zero due to the boundary condition. The local minimum in settling velocity between Zones I and II is most probably a numerical artifact and will be discussed later.

For the lowest bulk modulus ($K_0^f = 10^5$ Pa, blue curve), the observed settling velocity in Zone II is lower than the analytically expected settling velocity, while for the higher bulk moduli ($K_0^f = 10^6$ and 10^7 Pa, green and red curves), the agreement between simulations and the analytical solution is very good and the two latter curves are almost indistinguishable. The deviation in the first case can be explained by observing the high variation in fluid true pressure $\rho^{fR} \approx 1000 \dots 1070$ kg/m³ throughout the domain. Clearly, these densities are unphysical, but as noted before, low fluid bulk moduli may be assumed to increase the time step size, as long as the results are not negatively affected. Here, however, ρ^{fR} is also a parameter for the calculation of the drag term, cf. equations (3.65) and (3.66). For the calculation of the analytic solution via (5.7), $\rho^{fR} = 1000$ kg/m³ was assumed. In case of the higher bulk moduli, the range of fluid true densities is orders of magnitude lower, and is hence negligible. This observation shows that the solution at steady state, when dynamic effects are negligible, is indifferent to a change in fluid compressibility only if the density variation throughout the domain is low enough, i.e. high enough bulk moduli are prescribed. Consequently, low bulk moduli should be prescribed in order to increase overall nu-

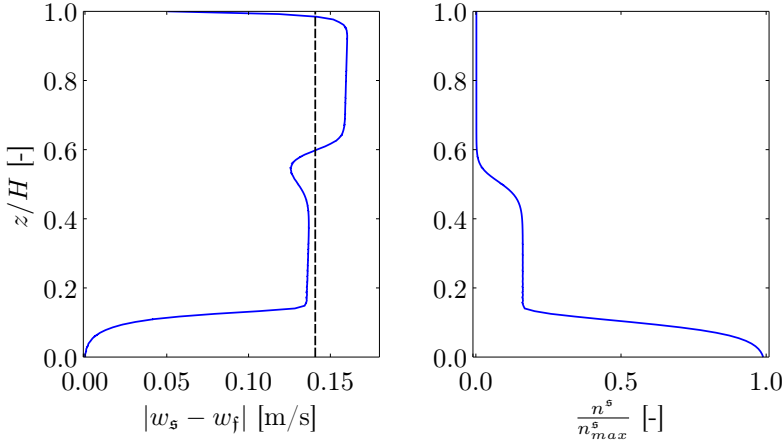


Figure 5.7: Left: Settling velocity vs. column height at $t = 2$ s for $n_0^s = 0.1$, compared to analytic solution (5.7) (dashed black line). Right: Solid volume fraction versus column height.

merical efficiency, yet assuring that the bulk moduli are high enough to keep density variations below a limit of desired accuracy. An alternative way to obtain a closer match with the analytic solution is to use the reference density ρ_{ref}^f rather than the true fluid density ρ^{fR} in the calculation of the drag term, (3.63). The true density ρ^{fR} does not correspond to the physical density in an experiment if the bulk modulus was chosen so low, so that using the physically more relevant reference density ρ_{ref}^f for the calculation of the drag term seems admissible.

Let us compare simulation result and analytic solution for a range of the parameters d and n_0^s in Table 5.1 (cf. Figures 5.5, 5.6 and 5.7). Note that all plots depict the physical time $t = 2$ s, and due to the different settling velocities resulting from the variation in physical parameters, the current state of the sedimentation process is quite different in each of the plots. In each figure, the right plot depicts the current solid volume fraction versus column height for orientation. Altogether, the results match quite well with the analytic solution (5.7), although a considerable deviation is visible in the lower part of the domain. This deviation is due to the unrealistically high fluid density in the lower part of the domain, as already noted. The simulation result approaches the analytic solution in the upper part of the domain, where the fluid density approaches its reference value. It is obvious from the results in Figure 5.4 that the deviation between simulation and analytic solution could easily be remedied by choosing a higher fluid bulk modulus, or, as noted earlier, by using the reference density ρ_{ref}^f rather than the true fluid density ρ^{fR} in the calculation of the drag term, (3.63).

The implementation of the full mixture equations allows to dissect and analyze exactly the different forces occurring in the momentum balances and their respective contribution to the overall flow in the different layers of the sedimentation column. This dissection of the momentum balance is shown in Figures 5.8 for the mixture and in Figure 5.10 for the solid. Before going into detail, let us define as positive driving forces those forces which point into the flow direction of a phase or, in case of the mixture, in the direction of the barycentric velocity at steady state sedimentation. The forces opposing these flow directions are denoted negative driving forces. Hence gravity is the positive driving force for both solid and mixture, while negative driving

forces for both solid and mixture are the gradients of fluid and solid configuration pressure, and for the solid, an additional negative driving force is momentum exchange.

Figure 5.8 depicts the driving forces of the mixture at four different times during Δt_{2-4} . Development of solid volume fraction and excess pore pressure are shown in the first two panels for orientation. Note that a gradient in excess pore pressure only exists within Zone II, where both phases are in motion. The positive driving force for the mixture is gravity (middle left panel), while the negative driving forces are the fluid pressure gradient (middle right panel) and the solid configuration pressure (lower left panel). Within Zone II, we expect the gravity to be fully opposed by the fluid pressure gradient and the configuration pressure gradient to be zero; while within Zone III, the fluid pressure gradient should only support the fluid's weight, and the extra stresses should be counteracted by the configuration pressure. This is exactly what is observed in the results. Note that at the interface between Zones II and III, gravity is opposed by the combined action of solid configuration and fluid pressure gradient; and that there is a minimum in fluid pressure gradient within the zone boundary. For the configuration pressure gradient, a small local maximum is observed at the interface between Zones I and II, which is due to the fact that $p_{conf}^s = f(n^s)$, cf. equation (3.56) and (3.57). This local minimum in solid configuration pressure is also the explanation for the local minimum in settling velocity observed in Figure 5.4. Hence, the local minimum in settling velocity is an undesired artifact. Furthermore, we observe oscillations in the solid configuration pressure gradient within Zone III when the sediment has fully settled. These oscillations are due to the fact that p_{conf}^s is singular for $n^s \rightarrow n_{max}^s$ and could for example be remedied by bounding the expression (3.57) such that a maximum value of p_{conf}^s is never exceeded.

Figure 5.9 depicts positive and negative driving forces for $t = 2.0$ s in one plot. It can be seen that the relevant forces during steady state sedimentation are gravity as positive driving force and solid configuration and fluid pressure gradients as negative driving forces. Hence during this steady state condition, the momentum balance for the mixture can be written as

$$(\rho^f + \rho^s)g = -\frac{\partial p^{fR}}{\partial z} - \frac{\partial p_{conf}^s}{\partial z}. \quad (5.8)$$

Convective and viscous contributions to the momentum balance are negligible, as assumed in the theory of Kynch [51] and derived using dimensional analysis in [14]. At steady state conditions, the mixture model approaches these solutions, which is a validation of the above theories, and for the present model.

The evolution of positive and negative driving forces for the solid phase are depicted in Figure 5.10. Again, the upper left panel gives the solid volume fraction for orientation. The positive driving force is again gravity (middle left panel), and the negative driving forces are momentum exchange (middle right), the solid contribution to the fluid pressure gradient (lower left), and the configuration pressure gradient (lower right). In Zone II, the negative driving forces are the momentum exchange term and the solid part of the fluid pressure gradient, while in the sedimented bed, gravity is opposed by the solid configuration pressure. Figure 5.11 collects all positive and negative driving forces for $t = 2$ s in one plot. Again, equilibrium is obtained by combining all positive and negative driving forces, and convective and viscous forces could be omitted in the partial momentum balance for the solid phase:

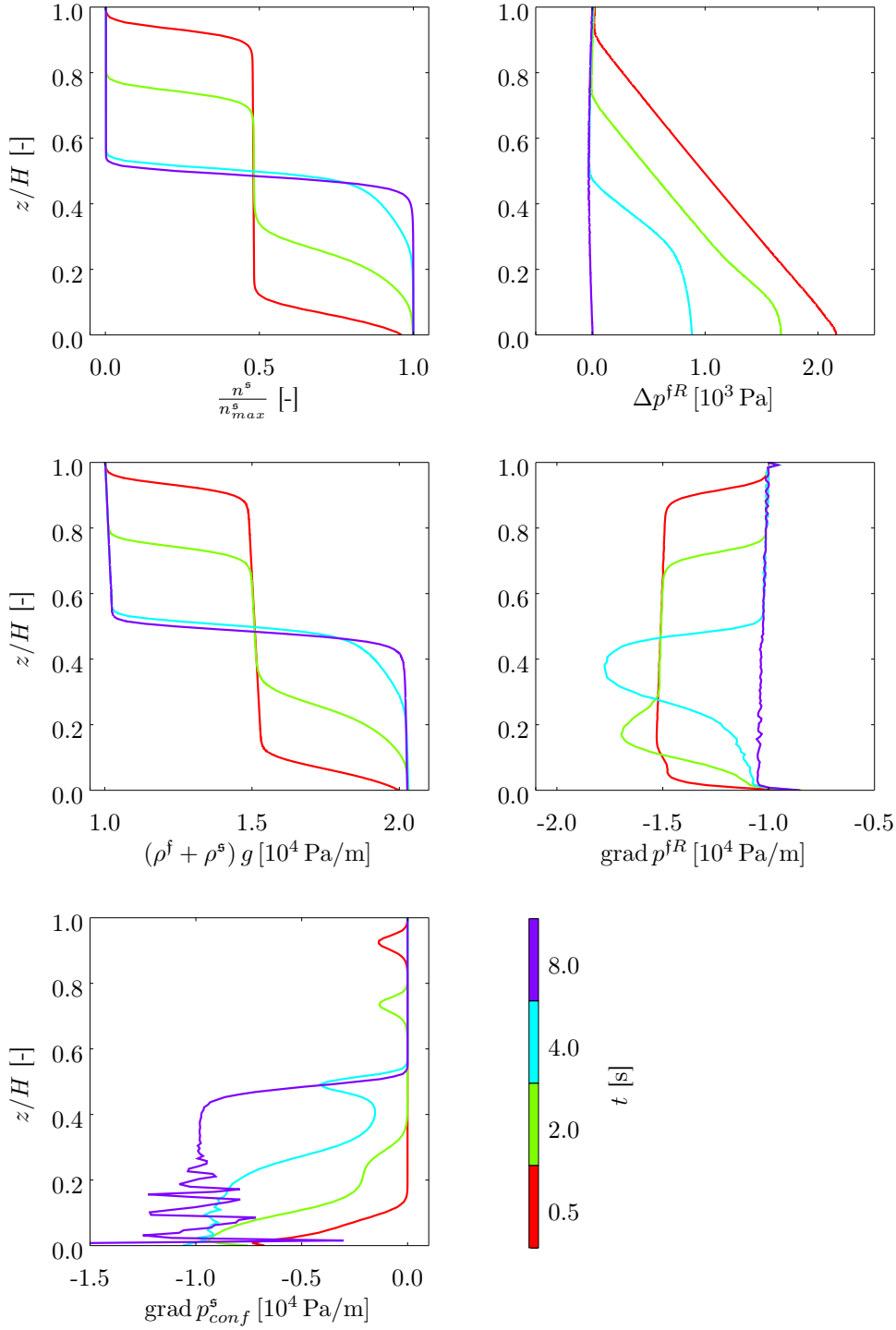


Figure 5.8: Time evolution of different quantities of the mixture vs. column height. All plots have the same x -axis scaling.

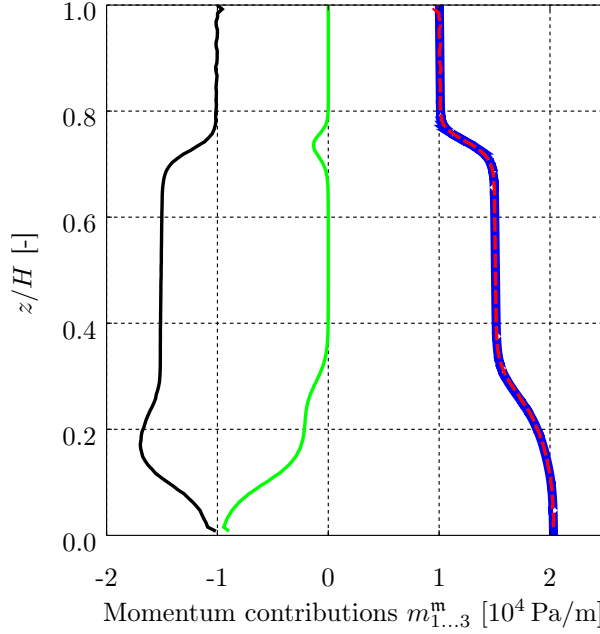


Figure 5.9: Contributions of positive and negative driving forces to the momentum balance of the mixture at $t = 2.0$ s. Blue: gravity contribution, $m_1^m = (\rho^f + \rho^s) g$, green: solid configuration pressure gradient contribution, $m_2^m = \frac{\partial n^s p_{conf}^s}{\partial z}$, black: fluid pressure gradient contribution, $m_3^m = \frac{\partial p^{fR}}{\partial z}$, red: modulus of sum of negative driving forces, $|m_2^m + m_3^m|$. Positive (blue) and negative (red) driving forces are in equilibrium.

$$\rho^s g = -n^s \frac{\partial p^{fR}}{\partial z} - \frac{\partial p_{conf}^s}{\partial z} - \hat{s}^s. \quad (5.9)$$

What is left to investigate is the influence of the model parameters K_0^f , $n_{max,\mu}^s$ and Θ^s on the model behavior. In case of K_0^f , differences are observed during the dynamic phase Δt_1 of the simulation (Figure 5.12). During this phase, the amplitudes of the oscillations in the integral time rate of change of solid volume fraction increase with decreasing fluid bulk modulus. This behavior is expected since in the limit of an incompressible fluid, we expect no oscillations at all.

Figure 5.13 depicts the influence of the parameters $n_{max,\mu}^s$ and Θ^s on the solid volume fraction profile. Variations in $n_{max,\mu}^s$ have almost no influence on the shape of the interface between Zone I and Zone II. The lower interface, however, is sharper for high values of $n_{max,\mu}^s$, and becomes less sharp as $n_{max,\mu}^s \rightarrow n_{max}^s$. This behavior is expected since the drag law given by equations (3.65) to (3.68) prescribes infinite drag for $n_{max,\mu}^s \rightarrow n_{max}^s$, cf. the discussion in Chapter 3. This effect could possibly be used as a simple means to model sedimentation-consolidation. A small granular temperature Θ^s leads to small configuration pressures p_{conf}^s for small values of n^s and a sharp increase in p_{conf}^s as $n^s \rightarrow n_{max}^s$; while larger granular temperatures lead to a more moderate increase in p_{conf}^s for all values of n^s . Consequently, the effect of lower granular temperatures is to make the two interfaces sharper, because high gradients

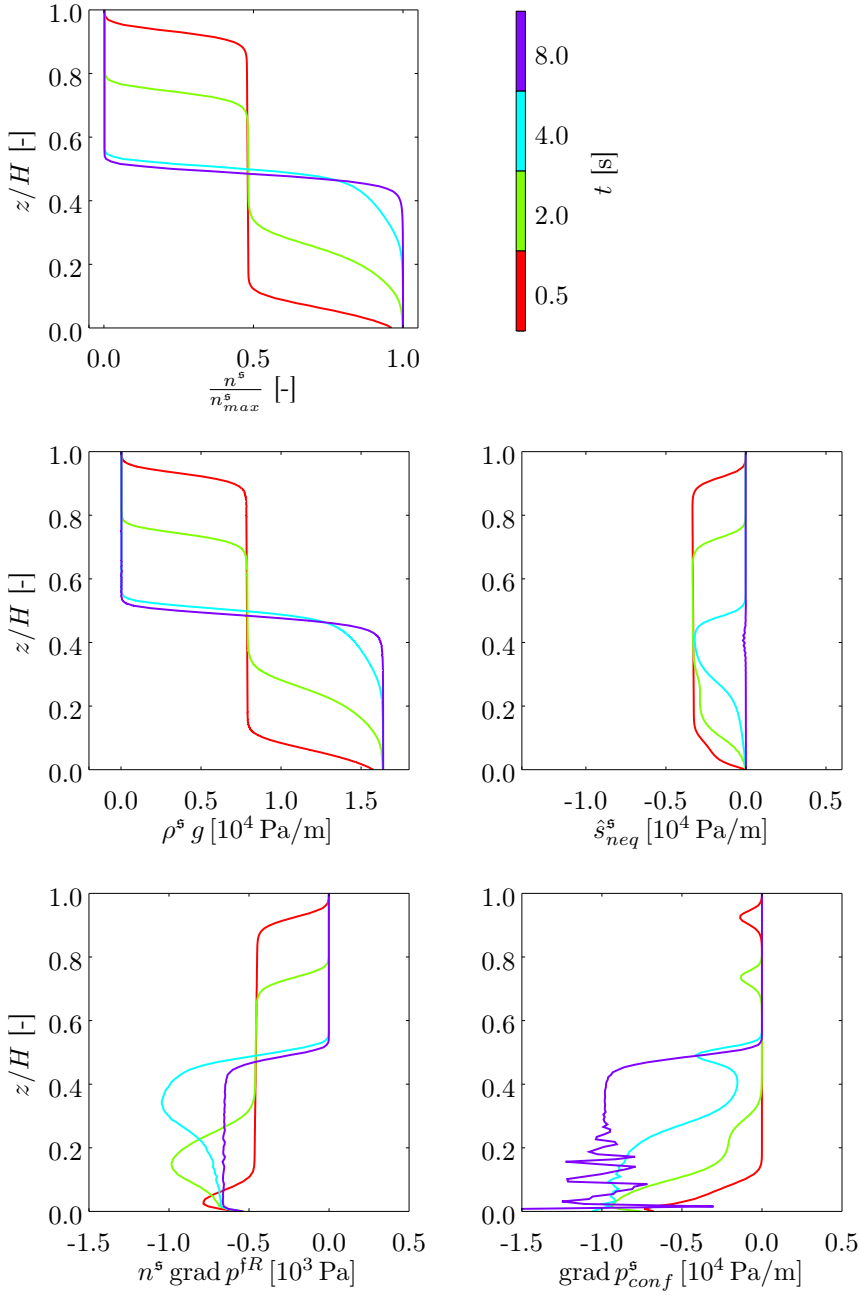


Figure 5.10: Time evolution of different quantities of the solid vs. column height. All plots have the same x-axis scaling.

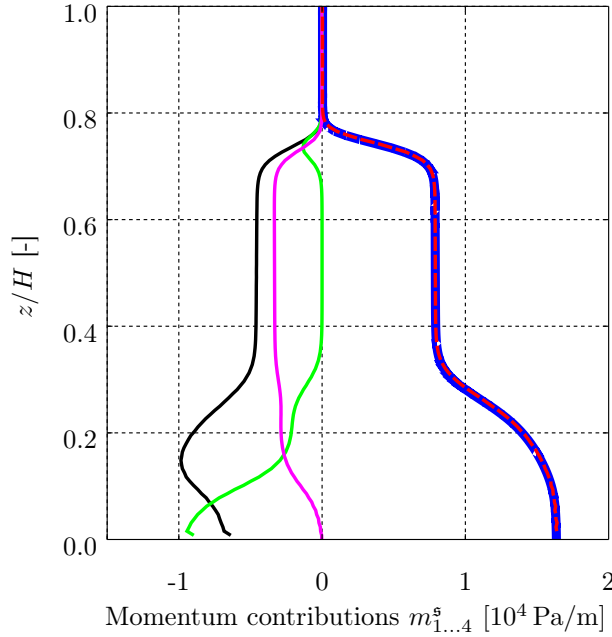


Figure 5.11: Contributions of positive and negative driving forces to the momentum balance of the solid at $t = 2.0$ s. Blue: gravity contribution, $m_1^s = \rho^s g$, green: solid configuration pressure gradient contribution, $m_2^s = \frac{\partial p_{conf}^s}{\partial z}$, black: solid part of fluid pressure gradient contribution, $m_3^s = n^s \frac{\partial p^{fR}}{\partial z}$, pink: momentum exchange term contribution, $m_4^s = \hat{s}_{neq}^s$, red: sum of negative driving forces, $|m_2^s + m_3^s + m_4^s|$. Positive (blue) and negative (red) driving forces are in equilibrium.

in p_{conf}^s are only seen where $n^s \rightarrow n_{max}^s$. In the framework of this study, it would be desirable to have sharp interfaces and hence small granular temperatures; however too small values have proven to be numerically unstable. The instability occurs at the interface between Zones II and III, and is probably due to the fact that p_{conf}^s is singular for $n^s \rightarrow n_{max}^s$, as discussed earlier in this section.

5.3 Conclusions

Discontinuous Galerkin-Finite Element calculations of batch sedimentation were presented. At the onset of flow, effects were observed due to the compressibility of the fluid that are not captured in conventional incompressible models. These effects may be unimportant for practical applications in the field of sedimentation, but are necessary for the description of other types of flow processes of fluid-saturated mixtures, cf. Chapter 2.

Here, the batch sedimentation case served as a simple benchmark to verify whether compressibility effects are visible. During steady state sedimentation, the results for settling velocity are in very good agreement with the analytical results of Ishii & Zuber [42] for a range of different fluid bulk moduli, initial solid volume fractions, and grain sizes. Deviations are due to variations in fluid density along the vertical column,

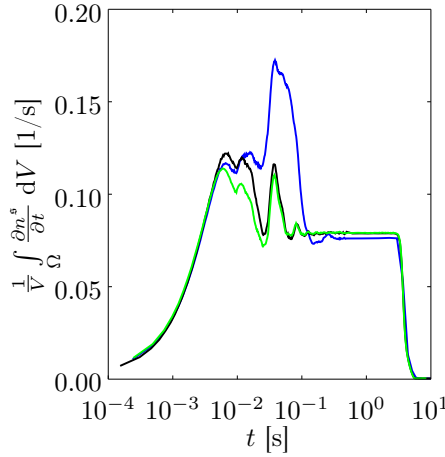


Figure 5.12: Temporal evolution of integral time rate of change of solid volume fraction for a range of fluid bulk moduli. Blue: $K_0^f = 10^5$ Pa, black: $K_0^f = 10^6$ Pa, green: $K_0^f = 10^7$ Pa.

which are higher when the prescribed fluid bulk modulus is low. The deviations can be reduced by prescribing higher fluid bulk moduli K_0^f , resulting in lower vertical density variations, or by using the reference fluid density ρ_{ref}^f instead of the true fluid density ρ^{fR} in the calculation of the drag force (3.65). Other than via the drag term, the results are not affected by unphysical, numerically more advantageous values of K_0^f , so that low values of K_0^f can be used to increase numerical efficiency when dynamic effects due to fluid compressibility are not of interest, e.g. during stationary sedimentation.

At the upper boundary, the velocity of both phases is zero. This behavior is not desired and is due to the open boundary condition, which prescribes zero far-field velocity for both phases. An improved boundary condition would prescribe a no-flux boundary condition at the top boundary for the *mixture* instead of separate boundary conditions for each single phase. However, the results away from the upper boundary appear not to be affected by this.

The contribution of the single terms of the momentum balances of solid and mixture to the overall force equilibrium were analyzed. It was found that during steady state sedimentation, equilibrium is attained by equating gravity with solid configuration and fluid pressure gradients in case of the mixture, and gravity with solid configuration and fluid pressure gradients and momentum exchange in case of the solid. Within the zone of homogeneous concentration (Zone II), the solid configuration pressure gradient does not contribute to the force equilibrium. Therefore, the hybrid model converges to the theories of Ishii & Zuber [42] and Kynch [51] at steady state. In these theories, it is a basic assumption that the only forces are gravity, fluid pressure gradient and drag.

In the simulations, the two boundaries separating the three zones from each other are not sharp, but distributed over a length of few centimeters. It was shown that a smaller granular temperature Θ^s leads to a sharper representation of the interfaces. However, in the current numerical implementation, stability is affected by too small values of Θ^s . In the future, this could be remedied by bounding p_{conf}^s to a finite value for $n^s \rightarrow n_{max}^s$. Smaller values of Θ^s would also avoid the local minimum in

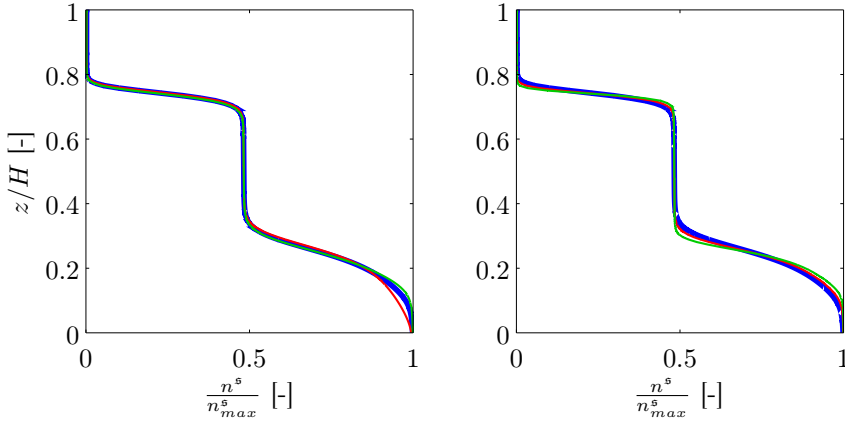


Figure 5.13: Effect of different values of $n^s_{max,\mu}$ (left) and Θ^s (right) on the shape of Zone boundaries. Left: $n^s_{max,\mu} = 0.64, 0.68, 0.72$ (red, blue, green); right: $\Theta^s = 0.012, 0.016, 0.02$ (green, red, blue)

$\text{grad } p^s_{conf}$ at the boundary between Zones I and II, which currently leads to a local decrease in settling velocity.

Summing up, the hybrid model performs well in capturing fluid compressibility effects in a batch sedimentation example, and converges to earlier sedimentation models at steady state. Further work concerns the extension and adjustment of the constitutive laws and the open boundary conditions to the type of flow described in Chapter 2.

Conclusions and Outlook

Experimental results were presented that reveal the outstanding role of the coupling between the evolution in porosity and the pore fluid pressure in granular-water mixture flow processes. The pore fluid pressure measurements cannot be explained without taking into account the compressibility of the pore fluid. The connection between fluid compressibility and porosity is established by the observation that the fluidization of an unconsolidated assembly of grains necessarily leads to a porosity increase, resulting in a volume increase of the fluid. If the pore fluid is assumed to be compressible and the conditions are not fully drained, this volume increase leads to a pressure drop. Here, the drainage is inhibited by the finite permeability of the porous skeleton, which prevents instantaneous water influx into the pore space. This interpretation is supported by the fact that the measured pressures compared to those from single-phase experiments are lower when the permeability of the porous medium is decreased. The exact amount of porosity increase could however not be determined, so that the degree of drainage could not be quantified. Future work could focus on improving the Particle Image Velocimetry (PIV) measurements to quantify exactly the porosity production. Moreover, PIV measurements in a larger image section could potentially detect the porosity wave that presumably propagates through the porous medium shortly after the simulation starts. A further experimental result is the observation that the flow process shown here is self-inhibiting: Fluidization of the grains causes a porosity increase, which leads to a fluid pressure drop, and consequently to a slight consolidation of the porous skeleton and retardation of the fluidization process.

Based on the experimental results, mass and momentum balance laws were chosen for the development of a mixture model of a weakly compressible barotropic pore fluid and an incompressible solid phase. Due to the complexity of the experimentally observed flow pattern, the balance equations were used to develop a model for the simpler case of batch sedimentation; but assuring for straightforward future extensibility to more complex types of flow. As the fluid is assumed compressible, it is possible to capture not only mass transport, but also acoustic wave propagation within this framework.

The hybrid model consists of a set of four strongly coupled partial differential equations. The discontinuous Galerkin method was found to be suitable for the solution of such a system of conservation laws. The numerical method allows for high-order approximation and relatively simple parallelization, at the same time being extremely robust for conservation laws. These findings were verified by a number of standard Computational Fluid Dynamics benchmarks, using a modified set of compressible Navier-Stokes equations that is similar to the hybrid model system of equations.

Acoustic waves, being a central part of the model, afforded the use of special open boundary conditions to avoid unrealistic reflections that would negatively affect the calculations. The boundary conditions require the prescription of a far-field state at

the boundary. Moreover, the boundary conditions require the system of equations to be hyperbolic. To adjust these boundary conditions to flows where the flow field is not known a priori and to a system of equations where hyperbolicity is difficult to assure is a major challenge.

An important feature of the model is its ability to capture mass transport and acoustic waves within the same framework. However, the explicit numerical representation introduces the need of very small time steps if acoustic wave speeds are to be realistically captured. Very efficient codes, possibly on Graphical Processing Units (GPUs) are necessary to obtain solutions within reasonable time frames. In case that the focus is on mass transport, however, the fluid compressibility can be increased, resulting in larger time steps. As a consequence, the actual wave speeds are not *precisely* captured, but the principal physical processes that can be attributed to the fluid compressibility are still visible.

Finally, numerical simulations of batch sedimentation were shown and the results at steady state were found to be in very good agreement with an analytical solution. Moreover, dynamic effects were observed at the beginning of the simulations that must be attributed to the compressible nature of the pore fluid. The acoustic waves emerging in the computational domain left the domain via the top boundary, where open boundary conditions were used. The observations indicate that the combination of the hybrid model and a numerical implementation in a discontinuous Galerkin framework is suitable for the description of the type of fluid-granular mixture flows presented in Chapter 2. The extension of the hybrid model to this more complex case, the adjustment of the open boundary conditions to the case of a free outflow with unknown far-field states and the improvement of the numerical implementation in terms of speed and robustness are left for further work.

Bibliography

- [1] URL <http://www.jpiv.vennemann-online.de>.
- [2] URL https://www.pcb.com/TechSupport/Tech_Pres.aspx.
- [3] T. B. Anderson and R. Jackson. Fluid mechanical description of fluidized beds. Equations of motion. *Industrial & Engineering Chemistry Fundamentals*, 6(4): 527–539, 1967. doi:10.1021/i160024a007.
- [4] R. Bakhtyar, A. Yeganeh-Bakhtiary, D. A. Barry, and A. Ghaheri. Two-phase hydrodynamic and sediment transport modeling of wave-generated sheet flow. *Advances in Water Resources*, 32(8):1267–1283, 2009.
- [5] F. Bassi and S. Rebay. A high-order accurate discontinuous finite element method for the numerical solution of the compressible Navier-Stokes equations. *J. Comput. Phys.*, 131(2):267–279, 1997. doi:10.1006/jcph.1996.5572.
- [6] G. Batchelor. *An Introduction to Fluid Dynamics*. Cambridge University Press, 1967.
- [7] M. Becker and M. Teschner. Weakly compressible SPH for free surface flows. In M. Gleicher and D. Thalmann, editors, *Symposium on Computer Animation*, pages 209–217. Eurographics Association, 2007.
- [8] M. Beyreuther, R. Barsch, L. Krischer, T. Megies, Y. Behr, and J. Wassermann. ObsPy: A Python Toolbox for Seismology. *Seismological Research Letters*, 81(3):530–533, 2010. doi:10.1785/gssrl.81.3.530.
- [9] M. A. Biot. General Theory of Three-Dimensional Consolidation. *Journal of Applied Physics*, 12:155–164, 1941. doi:10.1063/1.1712886.
- [10] S. Brdar, A. Dedner, and R. Klöforn. Compact and stable Discontinuous Galerkin methods for convection-diffusion problems. *SIAM Journal on Scientific Computing*, pages 1–18, 2012.
- [11] C. Brennen. *Fundamentals of Multiphase Flow*. Cambridge University Press, 2005. ISBN 9780521848046.
- [12] H. C. Brinkman. The viscosity of concentrated suspensions and solutions. *The Journal of Chemical Physics*, 20(4):571–571, 1952. doi:<http://dx.doi.org/10.1063/1.1700493>.

- [13] R. Bürger, W. Wendland, and F. Concha. Model equations for gravitational sedimentation-consolidation processes. *ZAMM - Journal of Applied Mathematics and Mechanics - Zeitschrift für Angewandte Mathematik und Mechanik*, 80(2):79–92, 2000. doi:10.1002/(SICI)1521-4001(200002)80:2<79::AID-ZAMM79>3.0.CO;2-Y.
- [14] C. Bustos. *Sedimentation and Thickening: Phenomenological Foundation and Mathematical Theory*. Mathematical Modelling: Theory and Applications. Springer, 1999. ISBN 9780792359609.
- [15] J. Chauchat, S. Guillou, D. Pham Van Bang, and K. Dan Nguyen. Modelling sedimentation-consolidation in the framework of a one-dimensional two-phase flow model. *Journal of Hydraulic Research*, 51(3):293–305, 2013. doi:10.1080/00221686.2013.768798.
- [16] B. Cockburn and C.-W. Shu. The local discontinuous Galerkin method for time-dependent convection-diffusion systems. *SIAM Journal on Numerical Analysis*, 35(6):2440–2463, 1998.
- [17] R. H. Cole. *Underwater explosions*. Princeton, Princeton Univ. Press,, 1948.
- [18] J. Ding and D. Gidaspow. A bubbling fluidization model using kinetic theory of granular flow. *AIChE Journal*, 36(4):523–538, 1990. doi:10.1002/aic.690360404.
- [19] P. Dong and K. Zhang. Intense near-bed sediment motions in waves and currents. *Coastal Engineering*, 45(2):75–87, 2002.
- [20] D. A. Drew. Turbulent sediment transport over a flat bottom using momentum balance. *Journal of Applied Mechanics - Transactions of ASME*, 42(1):38–44, 1975.
- [21] D. A. Drew and S. L. Passmann. *Theory of Multicomponent Fluids*, volume 135 of *Applied Mathematical Sciences*. Springer, 1999.
- [22] D. Drew. Mathematical modeling of two-phase flow. *Annual review of fluid mechanics*, 15:261–291, 1983.
- [23] D. Drew and S. Passman. *Theory of Multicomponent Fluids*. Applied Mathematical Sciences. Springer New York, 1998. ISBN 9780387983806.
- [24] W. Eckart, J. Gray, and K. Hutter. Particle Image Velocimetry (PIV) for granular avalanches on inclined planes. In K. Hutter and N. Kirchner, editors, *Dynamic Response of Granular and Porous Materials under Large and Catastrophic Deformations*, volume 11 of *Lecture Notes in Applied and Computational Mechanics*, pages 195–218. 2003. ISBN 978-3-642-05650-5. doi:10.1007/978-3-540-36565-5_6.
- [25] W. Ehlers, M. Schenke, and B. Markert. Liquefaction phenomena in fluid-saturated soil based on the theory of porous media and the framework of elasto-plasticity. *ZAMM - Journal of Applied Mathematics and Mechanics / Zeitschrift für Angewandte Mathematik und Mechanik*, 94(7-8):668–677, 2014. doi:10.1002/zamm.201200220.
- [26] A. Einstein. Eine neue Bestimmung der Moleküldimensionen. *Annalen der Physik*, 324(2):289–306, 1906. doi:10.1002/andp.19063240204.

- [27] E. Erturk, T. C. Corke, and C. Gökcöl. Numerical solutions of 2-d steady incompressible driven cavity flow at high Reynolds numbers. *International Journal for Numerical Methods in Fluids*, 48(7):747–774, 2005. doi:10.1002/flid.953.
- [28] M. Feistauer, J. Horáček, V. Kučera, and J. Prokopová. On Numerical Solution of Compressible Flow in Time-Dependent Domains. *Mathematica Bohemica*, 137(1):1–16, 2012.
- [29] N. Frankel and A. Acrivos. On the viscosity of a concentrated suspension of solid spheres. *Chemical Engineering Science*, 22(6):847 – 853, 1967. doi:http://dx.doi.org/10.1016/0009-2509(67)80149-0.
- [30] J. Fredsøe and R. Deigaard. *Mechanics of Coastal Sediment Transport*. World Scientific, 1992.
- [31] B. Galletti, C. H. Bruneau, L. Zannetti, and A. Iollo. Low-order modelling of laminar flow regimes past a confined square cylinder. *Journal of Fluid Mechanics*, 503:161–170, 3 2004. doi:10.1017/S0022112004007906.
- [32] U. Ghia, K. N. Ghia, and C. T. Shin. High-Re solutions for incompressible flow using the Navier-Stokes equations and a multigrid method. *Journal of Computational Physics*, 48:387–411, 1982. doi:10.1016/0021-9991(82)90058-4.
- [33] D. Gidaspow. *Multiphase Flow and Fluidization: Continuum and Kinetic Theory Descriptions*. Academic Press, 1994. ISBN 9780122824708.
- [34] J. Goddard, P. Giovine, and J. T. Jenkins, editors. *IUTAM Symposium on Mathematical Modeling and Physical Instances of Granular Flows (Cambridge, UK, July 7-9, 2009)*, volume 1227 of *AIP Conference Proceedings*, 2010. AIP Press.
- [35] J. Hesthaven and T. Warburton. *Nodal Discontinuous Galerkin Methods: Algorithms, Analysis, and Applications*. Texts in Applied Mathematics. Springer, 2008. ISBN 9780387720654.
- [36] C. Hirt and B. Nichols. Volume of fluid (VOF) method for the dynamics of free boundaries. *Journal of Computational Physics*, 39(1):201–225, 1981. doi:10.1016/0021-9991(81)90145-5.
- [37] F. Q. Hu, X. Li, and D. Lin. Absorbing boundary conditions for nonlinear Euler and Navier–Stokes equations based on the perfectly matched layer technique. *Journal of Computational Physics*, 227(9):4398–4424, 2008. doi:10.1016/j.jcp.2008.01.010.
- [38] K. Hutter and K. Jöhnk. *Continuum Methods of Physical Modeling: Continuum Mechanics, Dimensional Analysis, Turbulence*. Springer, 2004. ISBN 9783540206194.
- [39] K. Hutter. Geophysical granular and particle-laden flows: review of the field. *Philosophical Transactions of the Royal Society of London A: Mathematical, Physical and Engineering Sciences*, 363(1832):1497–1505, 2005. doi:10.1098/rsta.2005.1591.

- [40] K. Hutter and L. Schneider. Important aspects in the formulation of solid–fluid debris-flow models. Part I. Thermodynamic implications. *Continuum Mechanics and Thermodynamics*, 22(5):363–390, 2010. doi:10.1007/s00161-010-0153-x.
- [41] K. Hutter and L. Schneider. Important aspects in the formulation of solid–fluid debris-flow models. Part II. Constitutive modelling. *Continuum Mechanics and Thermodynamics*, 22(5):391–411, 2010. doi:10.1007/s00161-010-0154-9.
- [42] M. Ishii and N. Zuber. Drag coefficient and relative velocity in bubbly, droplet or particulate flows. *AIChE Journal*, 25(5):843–855, 1979. doi:10.1002/aic.690250513.
- [43] R. M. Iverson and R. P. Denlinger. Flow of variably fluidized granular masses across three-dimensional terrain: 1. Coulomb mixture theory. *Journal of Geophysical Research: Solid Earth*, 106(B1):537–552, 2001. ISSN 2156-2202. doi:10.1029/2000JB900329.
- [44] R. Jackson. *The Dynamics of Fluidized Particles*. Cambridge Monographs on Mechanics. Cambridge University Press, 2000. ISBN 9780521781220.
- [45] J. T. Jenkins and D. M. Hanes. Collisional sheet flows of sediment driven by a turbulent fluid. *Journal of Fluid Mechanics*, 370:29–52, 9 1998. ISSN 1469-7645. doi:10.1017/S0022112098001840.
- [46] R. Katzenbach and C. Bergmann. Investigation on mass flow of saturated soil by large scale experiments. In *Proceedings of the 18th International Conference on Soil Mechanics and Geotechnical Engineering*, number 3, pages 1–4, 2013.
- [47] A. Klöckner, T. Warburton, J. Bridge, and J. S. Hesthaven. Nodal discontinuous Galerkin methods on graphics processors. *Journal of Computational Physics*, 228:7863–7882, 2009.
- [48] A. Klöckner, T. Warburton, and J. S. Hesthaven. Viscous Shock Capturing in a Time-Explicit Discontinuous Galerkin Method. *Mathematical Modelling of Natural Phenomena*, X(X):1–27, 2011.
- [49] A. Klöckner, T. Warburton, and J. S. Hesthaven. Solving wave equations on unstructured geometries. *CoRR*, abs/1304.5546, 2013.
- [50] S. Kraft, Y. Wang, and M. Oberlack. Large Eddy Simulation of Sediment Deformation in a Turbulent Flow by Means of Level-Set Method. *Journal of Hydraulic Engineering*, pages 1394–1405, 2011. doi:10.1061/(ASCE)HY.1943-7900.0000439.
- [51] G. J. Kynch. A theory of sedimentation. *Trans. Faraday Soc.*, 48:166–176, 1952. doi:10.1039/TF9524800166.
- [52] B. Larock, R. Jeppson, and G. Watters. *Hydraulics of Pipeline Systems*. CRC Press, 2010. ISBN 9781420050318. URL <https://books.google.de/books?id=RAMX5xuXSrUC>.
- [53] M. Latsa, D. Assimacopoulos, A. Stamou, and N. Markatos. Two-phase modeling of batch sedimentation. *Applied Mathematical Modelling*, 23(12):881–897, 1999. doi:10.1016/S0307-904X(99)00016-5.

- [54] H. Laux and T. Yttrhus. Computer simulation and experiments on two-phase flow in an inclined sedimentation vessel. *Powder Technology*, 94(1):35 – 49, 1997. doi:[http://dx.doi.org/10.1016/S0032-5910\(97\)03285-3](http://dx.doi.org/10.1016/S0032-5910(97)03285-3).
- [55] A. Leonardi, F. Wittel, M. Mendoza, and H. Herrmann. Multiphase debris flow simulations with the discrete element method coupled with a lattice-Boltzmann fluid. In *Proceedings of III International Conference on Particle-based Methods, PARTICLES*, volume 2013, 2013.
- [56] Y.-H. Li. Equation of state of water and sea water. *Journal of Geophysical Research*, 72(10):2665–2678, 1967. doi:[10.1029/JZ072i010p02665](https://doi.org/10.1029/JZ072i010p02665).
- [57] F. Lominé, L. Scholtès, L. Sibille, and P. Poullain. Modeling of fluid-solid interaction in granular media with coupled lattice Boltzmann/discrete element methods: application to piping erosion. *International Journal for Numerical and Analytical Methods in Geomechanics*, 37(6):577–596, 2013. doi:[10.1002/nag.1109](https://doi.org/10.1002/nag.1109).
- [58] R. M. Lueptow, A. Akonur, and T. Shinbrot. PIV for granular flows. *Experiments in Fluids*, 28(2):183–186, 2000. doi:[10.1007/s003480050023](https://doi.org/10.1007/s003480050023).
- [59] C. K. K. Lun, S. B. Savage, D. J. Jeffrey, and N. Chepurniy. Kinetic theories for granular flow: inelastic particles in couette flow and slightly inelastic particles in a general flow field. *Journal of Fluid Mechanics*, 140:223–256, 1984. doi:[10.1017/S0022112084000586](https://doi.org/10.1017/S0022112084000586).
- [60] H. Luo, H. Segawa, and M. R. Visbal. An implicit discontinuous Galerkin method for the unsteady compressible Navier-Stokes equations. *Computers & Fluids*, 53: 133–144, 2012. doi:[10.1016/j.compfluid.2011.10.009](https://doi.org/10.1016/j.compfluid.2011.10.009).
- [61] V. Marieu, P. Bonneton, D. L. Foster, and F. Ardhuin. Modeling of vortex ripple morphodynamics. *Journal of Geophysical Research*, 113(C9):C09007, 2008. doi:[10.1029/2007JC004659](https://doi.org/10.1029/2007JC004659).
- [62] V. Matousek. *Flow mechanism of sand-water mixtures in pipelines*. PhD thesis, TU Delft, Delft University of Technology, 1997.
- [63] J. Monaghan. Smoothed Particle Hydrodynamics and its diverse applications. *Annual Review of Fluid Mechanics*, 44(1):323–346, 2012. doi:[10.1146/annurev-fluid-120710-101220](https://doi.org/10.1146/annurev-fluid-120710-101220).
- [64] S. Ogawa, A. Umemura, and N. Oshima. On the equations of fully fluidized granular materials. *Zeitschrift für angewandte Mathematik und Physik ZAMP*, 31(4):483–493, 1980. doi:[10.1007/BF01590859](https://doi.org/10.1007/BF01590859).
- [65] A. Penko, J. Calantoni, S. Rodriguez-Abudo, D. Foster, and D. Slinn. Three-dimensional mixture simulations of flow over dynamic rippled beds. *Journal of Geophysical Research: Oceans*, 118(3):1543–1555, 2013. doi:[10.1002/jgrc.20120](https://doi.org/10.1002/jgrc.20120).
- [66] J. Peraire and P.-O. Persson. The Compact Discontinuous Galerkin (CDG) Method for Elliptic Problems. *SIAM Journal on Scientific Computing*, 30(4): 1806–1824, 2008. doi:[10.1137/070685518](https://doi.org/10.1137/070685518).
- [67] E. B. Pitman and L. Le. A two-fluid model for avalanche and debris flows. *Philosophical Transactions. Series A, Mathematical, physical, and engineering sciences*, 363(1832):1573–601, 2005. doi:[10.1098/rsta.2005.1596](https://doi.org/10.1098/rsta.2005.1596).

- [68] S. P. Pudasaini. A general two-phase debris flow model. *Journal of Geophysical Research: Earth Surface*, 117(F03010), 2012. doi:10.1029/2011JF002186.
- [69] S. Pudasaini and K. Hutter. *Avalanche Dynamics: Dynamics of Rapid Flows of Dense Granular Avalanches*. Springer, 2007. ISBN 9783540326861.
- [70] J. F. Richardson and W. N. Zaki. Sedimentation and fluidisation: Part 1. *Trans. Inst. Chem. Eng.*, 32(35-53), 1954.
- [71] R. Roscoe. The viscosity of suspensions of rigid spheres. *British Journal of Applied Physics*, 3(8):267, 1952.
- [72] R. Ruiz-Baier and H. Torres. Numerical solution of a multidimensional sedimentation problem using finite volume-element methods. *Applied Numerical Mathematics*, 1:1–12, 2014. doi:10.1016/j.apnum.2013.12.006.
- [73] H. Rusche. *Computational Fluid Dynamics of Dispersed Two-Phase Flows at High Phase Fractions*. PhD thesis, Imperial College, London, 2002.
- [74] H. Schlichting, K. Gersten, and K. Gersten. *Boundary-Layer Theory*. Springer, 2000. ISBN 9783540662709.
- [75] L. Schneider and K. Hutter. *Solid-Fluid Mixtures of Frictional Materials in Geophysical and Geotechnical Context: Based on a Concise Thermodynamic Analysis*. Advances in Geophysical and Environmental Mechanics and Mathematics. Springer, 2009. ISBN 9783642029684.
- [76] R. Sivanapillai, H. Steeb, and A. Hartmaier. Transition of effective hydraulic properties from low to high reynolds number flow in porous media. *Geophysical Research Letters*, 41(14):4920–4928, 2014. doi:10.1002/2014GL060232.
- [77] C. Slominski, M. Niedostatkiewicz, and J. Tejchman. Application of Particle Image Velocimetry (PIV) for deformation measurement during granular silo flow. *Powder Technology*, 173(1):1–18, 2007. doi:http://dx.doi.org/10.1016/j.powtec.2006.11.018.
- [78] H. Steeb. *Non-Equilibrium Processes in Porous Media*. Fachbereich 8.4 Materialwissenschaften, Lehrstuhl für Technische Mechanik, Saarbrücken, 2008.
- [79] M. Syamlal, W. Rogers, and T. O’Brien. *MFIX documentation theory guide*, 1993.
- [80] T. Takahashi. *Debris Flow: Mechanics, Prediction and Countermeasures*. Balkema-proceedings and monographs in engineering, water, and earth sciences. Taylor & Francis, 2007. ISBN 9780203946282.
- [81] P. Tassi, S. Rhebergen, C. Vionnet, and O. Bokhove. A discontinuous Galerkin finite element model for river bed evolution under shallow flows. *Computer Methods in Applied Mechanics and Engineering*, 197(33-40):2930–2947, 2008. doi:10.1016/j.cma.2008.01.023.
- [82] K. Terzaghi. *Erdbaumechanik auf bodenphysikalischer Grundlage*. F. Deuticke, 1925.

- [83] C. Truesdell. Sulle basi della termomeccanica, I & II. *Rend. Accad. Lincei*, 22: 33–38, 158–166, 1957.
- [84] A. Verruijt. *Consolidation of Soils*. John Wiley & Sons, Ltd, 2006. ISBN 9780470848944. doi:10.1002/0470848944.hsa303.
- [85] Q. Wang, X. Zhang, Y. Zhang, and Q. Yi. AUGEM: Automatically Generate High Performance Dense Linear Algebra Kernels on x86 CPUs. In *Proceedings of the International Conference on High Performance Computing, Networking, Storage and Analysis*, pages 25:1–25:12, 2013. doi:10.1145/2503210.2503219.
- [86] R. C. Whaley and A. Petitet. Minimizing development and maintenance costs in supporting persistently optimized BLAS. *Software: Practice and Experience*, 35(2):101–121, 2005.
- [87] K. Yazdchi, S. Srivastava, and S. Luding. Fem-dem simulation of two-way fluid-solid interaction in fibrous porous media. In *Powders and Grains 2013: Proceedings of the 7th International Conference on Micromechanics of Granular Media*, volume 1542, pages 1015–1018. AIP Publishing, 2013.
- [88] K. Zhang, G. Wu, S. Brandani, H. Chen, and Y. Yang. CFD simulation of dynamic characteristics in liquid-solid fluidized beds. *Powder Technology*, 227: 104–110, 2012. doi:10.1016/j.powtec.2012.01.030.

Curriculum Vitae

Timo Timotheus Reisner

Date and Place of Birth: 19.02.1982, Dortmund

Education:

- 02/2011 – 09/2015 **Ph.D. Student and Research Assistant**
Chair of Mechanics – Continuum Mechanics, Ruhr-University Bochum, Germany
- 10/2011 – 10/2015 **Advanced training in Academic Didactics**
Ruhr-University Bochum, Germany
- Graduate of the professional qualification programme in Academic Didactics
- 03/2011 – 11/2015 **Member of Ruhr-University Research School**
- Graduate of the structured training programme
- 10/2005 – 12/2010 **Study of Geosciences – major Geophysics**
Institute of Geology, Mineralogy and Geophysics, Ruhr-University Bochum, Germany
- 2010: Master of Science, grade point average: excellent
- 2008: Bachelor of Science, grade point average: very good
- 10/2004 – 09/2005 **Study of Geography**
Institute of Geography, Ruhr-University Bochum, Germany
- 08/2001 – 01/2004 **Apprenticeship in Refrigeration Mechanics**
Professional association for Refrigeration and Air Conditioning Technology, Dortmund and Reisner GmbH, Holzwickede, Germany
- 2004: Apprenticeship diploma in Refrigeration Mechanics
- 06/2001 **Abitur (mandatory legitimation for university entry)**
Ernst-Barlach-Gymnasium, Unna, Germany

Professional experience:

- 2008, 2012
(part time) **Expert Editing**
- Proofreading and redevelopment of a book on Refrigeration Engineering: „Fachwissen Kältetechnik“ by Klaus Reisner, VDE Verlag, 4th edition (2008) and 5th edition (2013)
- 02/2006 – 12/2010
(part time) **Student Helper (Laboratory Assistant)**
Experimental Geophysics Group at Institute of Geology, Mineralogy and Geophysics, Ruhr-University Bochum
- 01/2004 – 10/2004
(full time) **Refrigeration Mechanic**
Reisner GmbH, Holzwickede, Germany
- 10/2004 – 07/2010
(part time) - Service technician, worldwide on-site service for industrial refrigeration plants
- 05/2008 – 06/2008 **Internship (five weeks)**
CSIRO Land and Water, Perth, WA, Australia

Witten, November 2015

**Mitteilungen aus dem Institut für Mechanik
RUHR-UNIVERSITÄT BOCHUM
Nr. 163**

ISBN 978-3-935892-41-4